NASA CR-54686

SUMMARY REPORT

STUDY OF MAGNETIC ANNULAR PLASMA ACCELERATOR

by

R. M. Patrick and A.M. Schneiderman

Contract NAS 3-5748

April 15,1964 - January 14,1966

prepared for

LEWIS RESEARCH CENTER
NATIONAL AERONAUTICS and SPACE ADMINISTRATION
Cleveland, Ohio

AVCO EVERETT RESEARCH LABORATORY
A DIVISION OF AVCO CORPORATION
2385 REVERE BEACH PARKWAY · EVERETT, MASSACHUSETTS 02149

Requests for copies of this report should be referred to

National Aeronautics and Space Administration
Office of Scientific and Technical Information
Attention: AFSS-A
Washington, D. C. 20546

NASA CR-54686

SUMMARY REPORT

STUDY OF MAGNETIC ANNULAR PLASMA ACCELERATOR

by

R. M. Patrick and A. M. Schneiderman

AVCO EVERETT RESEARCH LABORATORY
a division of
AVCO CORPORATION
Everett, Massachusetts

Contract NAS 3-5748

April 15, 1964 - January 14, 1966

prepared for

LEWIS RESEARCH CENTER
NATIONAL AERONAUTICS AND SPACE ADMINISTRATION
Cleveland, Ohio

TABLE OF CONTENTS

		Page
I.	INTRODUCTION	1
II.	DESCRIPTION OF DEVICE	5
III.	DESCRIPTION OF DIAGNOSTICS	9
	Total Mass Flow Measurements	9
	Arc Voltage, Arc Current and Arc Power	9
	Total Power in the Gas	9
	Magnetic Field Coil Current	10
	Thrust Measurements	10
	Local Mass Flow Density Measurements	14
	Axial Current Distribution Measurements	18
IV.	EXPERIMENTAL AND THEORETICAL RESULTS	21
	Current-Voltage Characteristics	21
	V-B Characteristics	22
	Mode Changes in the MAARC	25
	Anode Heat Transfer Results	27
	Thrust Measurements	28
	Oscillograms Showing ρu^2 Versus Radius	28
	Effect of Magnetic Field on Thrust	29
	Thrust Stand Measurements	31
	Specific Impulse and Thrust Efficiency	32
	ρu Measurements	33
	Entrainment of Ambient Tank Gas	34
	Operation of MAARC with no Net Propellant Through-put	35
	ρu Measurements of Entrainment in Hydrogen	36
	Shroud Measurements	36
	Ammonia Data	37
	Conclusions on Entrainment	38
	Discussion of High Exhaust Velocity Versus Low Operating Voltage Results of Other Experiments	39
V.	RECOMMENDATIONS AND CONCLUSIONS	43
VI.	REFERENCES	47
	ADDENDUM	(i)
	Optimization of Thermal Efficiency	(ii)
	Axial Current Distribution in the Exhaust	(vii)

SECTION I

INTRODUCTION

This report summarizes the experimental and analytical studies of the past seventeen months that have been directed toward achieving high propulsive efficiencies in the 2000-3500 sec specific impulse range with a magnetic annular arc (MAARC). The MAARC is very similar to the device described in Ref. 1, and the motivation for making the accelerator in its present form has not changed. Therefore, some of the arguments made in that reference for the choice of the MAARC geometry will be reproduced here.

Direct current plasma accelerators are very attractive for plasma propulsion because of their compact size and the simplicity of associated electrical circuitry and propellant feed requirements. The ordinary thermal arc jet is the least intricate device in this category, but is limited to temperatures corresponding to specific impulses below 1500 sec by the onset of excessive thermal ionization. To avoid the limitations of the pure thermal arc jet, magnetohydrodynamic dc plasma accelerators which make use of crossed electric and magnetic fields to produce acceleration have been investigated. The plasma in this type of device has sufficiently low conductivity so that the magnetic field can diffuse through the plasma. The plasma need only be slightly ionized and the thrust energy is largely obtained through the $\vec{j} \times \vec{B}$ forces which act throughout the volume of the accelerator. The limitations of a $\vec{j} \times \vec{B}$ accelerator with a rectangular channel due to boundary layer and side wall effects[2, 3] led us to consider an axisymmetric geometry. The discharge takes place in the annulus between two coaxial electrodes (Fig. 1) with a magnetic field throughout the flow region. This geometry was chosen for the following reasons:

1. When the magnetic field has a sufficiently high intensity so that the electrons in the arc plasma undergo a complete gyro orbit before making a collision (i.e., $\omega_e \tau_e > 1$), the arc impedance is increased. This increased plasma

impedance reduces the effect of electrode voltage drops and leads to a more efficient arc operation.

2. The discharge is stable when $\omega_e \tau_e > 1$ and the arc is uniformly distributed throughout the channel.
3. Momentum can be added to the plasma by $\vec{j} \times \vec{B}$ forces in both azimuthal and axial directions. The azimuthally directed energy can be recovered in an expansion nozzle in the form of directed axial velocity.
4. The magnetic field is aligned essentially parallel or at small angles to the channel walls, and since the $\omega\tau$ for the electrons is large compared to unity, the azimuthal (Hall) currents are the largest component of the current in the nozzle. The j x B forces are directed away from the channel walls. Therefore, both acceleration and containment are achieved in this device with plasma conditions corresponding to a relatively low degree of ionization and low electrical conductivity.

There has been a large increase in the interest in this type of device recently by several investigators.[4-7] This increased interest has been due to the achievement of very high specific impulses with these magnetic arcs and the attainment of high enthalpies in the arc heated plasma without excessive wall losses.[7] There is a basic similarity in geometry between the magnetic annular arc and the several other magnetoplasmadynamic (MPD) arc devices that have been described recently. They all have an axisymmetric geometry consisting of a central cathode and an axisymmetric anode surrounded by a solenoidal magnetic field. There is general agreement that the applied magnetic field is necessary to stabilize the arc and make the discharge more uniform, and also increase the arc voltage and reduce wall losses. In addition, for the experiments described in Refs. 1 and 8, and those by Hess[4] and Cann,[6] the B field has been used to change the current configuration and produce additional thrust. In the experiments described in this paper, the B field was used to stabilize the arc and make it uniform, and also to play a basic role in the acceleration of the arc heated plasma due to the interaction of the arc currents and the applied B field.

The new results which have been obtained since our last publication can be divided into four categories. First, the voltage characteristics of the device with various propellants and bias field intensities have been investigated, and it has been found that the voltage is linearly dependent on the bias field intensity and that is a function of the propellant used and the B field geometry. A simple theory has been developed which predicts the MAARC voltage and can be expressed by the relation

$$V = V_o + U_c B \ell \quad ,$$

where V is the overall MAARC voltage, V_o is an integration constant related to the electrode voltage drop which is determined by the electrode configuration, B is the magnetic field strength near the cathode, ℓ is the length of the upstream end of the discharge normal to the B field, and U_c is the speed an incoming molecule must have so its kinetic energy equals the energy required to dissociate and/or ionize it.

Second, detailed measurements of the thrust profile obtained with a thrust plate system have been obtained at low mass flows and various magnetic field shapes and intensities. The results show that both the magnitude of the total thrust and the thrust density profile (ρu^2) are very sensitive to both the magnetic field intensity and shape. Furthermore, for some particular bias magnetic field geometries, an optimum magnetic field intensity has been observed which produces a maximum overall thrust efficiency.

Third, local mass flow distributions have been measured in the plasma jet. These measurements have been made with a sharp edged conical mass flow probe which can be traversed over the whole jet. The measurements indicate that the ambient tank gas mixes with the plasma issuing from the MAARC nozzle, making the interpretation of the ρu^2 and ρu profiles difficult. It became apparent from these measurements that there were two ways in which the ambient tank gas could mix with the primary plasma jet. First, viscous mixing along the boundary between the jet and ambient gas, setting up a cell of moving gas in the tank; second, diffusion of the tank gas into the regions of the MAARC flow where this gas could be accelerated by the MAARC currents. These results led us to investigate the fourth category, namely the arc current distributions.

The fourth category of measurements consists of measuring the axial and radial current distribution in the plasma flow in order to determine the importance of the ambient tank gas on the MAARC performance.

This report describes the experiments and the experimental technique carried out to show the above-mentioned effects and also contains a discussion of the results.

SECTION II

DESCRIPTION OF DEVICE

The magnetic annular arc (MAARC) is an axisymmetric, magneto-hydrodynamic Hall accelerator. It consists of a diverging anode, a coaxial cathode, and an external magnet.

The anode is fabricated from thin walled copper and placed in a conformed cavity where water cools its external surfaces. The anode itself acts as a hypersonic nozzle. The divergence half angle (50^{o}) contributes in two ways to the high thermal efficiency (typically 55-90%) of this device. It provides a smooth boundary of very small surface area for the jet with no prominent protrusions into the flow, and hence lacks stagnation regions to which large amounts of gas enthalpy can be lost or upon which high speed flow phenomena (such as shocks) can attach. It also allows the use of highly divergent magnetic fields without permitting these fields to link the anode and cathode, and hence provide a low impedance path between them; or to force the flow itself to stream into the anode. The anode has an internal diameter of 5/8 inch.

The cathode consists of a one inch length of 5/16 inch diameter thoriated tungsten rod with a 45^{o} conical tip. The conical tip stabilizes the arc by forcing it to run off the apex where the electric field is highest. The tungsten tip is fastened to coaxial copper tubes which provide an electrical connection, support, and water cooling to the cathode base. A 7/16 inch outside diameter quartz tube is placed around the copper tubes and most of the tungsten tip to prevent currents from flowing to the internal surfaces of the anode. This quartz tube represents the only internal insulation in the device. Figure 2 is a photograph of the anode and the composite cathode systems.

Magnetic field coils of various geometric shapes have been used in obtaining the data presented in this report. The following table summarizes the geometric characteristics of these coils.

Coils	OD in.	Width in.	Turns	G/100A at cathode
Large Heat Sink	18	4	1280	1250*
Medium Heat Sink	10	3	474	1300
Medium Water Cooled	10	3	88	400
Small Water Cooled	6	4	40	108
Trimmer Coil	12	4	21	67

The coils are 2 inches ID except for the trimming coil whose ID is 10 inches.

The trimming coil fits outside the medium water cooled coil. It can be separately excited and permits continuous field shape variations over a range which covers all the other coils.

Several field plots are shown in Figs. 3 and 4. Note the small difference in field shape between the medium heat sink and water cooled coils.

The MAARC is powered by a large storage battery bank capable of delivering up to 5 megawatts. A water cooled ballast resistor is placed in series with the arc, and provides a variable load line upon which the arc is free to operate.

The magnetic field coil is powered by a 50 kW Miller welder which is well regulated to provide a constant current even with resistance changes in the coil due to heating. The experimental facility is so arranged that power supplies for the field coil and the arc can be interchanged or used concurrently.

The vacuum system for the MAARC consists of a 30 inch diameter by 4 foot long cylindrical aluminum tank which is evacuated by a 5200 cfm Roots blower backed by a 500 cfm Stokes forepump. The outer surface of the anode cooling jacket is connected to one end flange of this tank, the field coil being outside the vacuum facility. The MAARC is made to float electrically from the tank with suitable insulation.

It is felt that all materials problems in this installation have been satisfactorily solved with the use of water cooled copper, radiation and water

* The large heat sink coil is 2 inches further away from the cathode than the other coils.

cooled tungsten, and quartz. Quartz has been found to be especially useful as an insulator in these high enthalpy flows because of its high melting point, large heat conduction coefficient, and its ability to withstand thermal shock. These materials now permit clean arc performance and no ablation of the anode or cathode during several hours of operation.

SECTION III

DESCRIPTION OF DIAGNOSTICS

We have chosen to use local diagnostics rather than to make overall measurements. This technique provides a great deal of additional information which permits a greater insight into the details of operation of the device. It leads to means of calculating density and velocity profiles.

Total Mass Flow Measurements

The mass flow through the magnetic annular arc is monitored with a Fisher-Porter tri flat flowmeter with accuracy reported by the manufacturer as better than $\pm$ 2%. It has been calibrated with the data supplied by the manufacturer and checks have been made by determining the rate of pressure increase in a known volume to which the propellant is made to flow.

Arc Voltage, Arc Current and Arc Power

The arc voltage is determined with a voltmeter which is placed directly across the arc. A 2000 amps equals 50 mv series shunt is used to determine the arc current. In addition, the voltage drop across a known portion of the arc ballast resistor is monitored to provide a check on the arc current. This latter system provides signals of the order of a hundred volts rather than the millivolt signals obtained from the shunt.

Both arc current and voltage are simultaneously monitored on strip recorders thus giving accurate measures of any time variation in arc performance. The arc power is computed from the product of measured arc current and voltage and hence, can be accurately determined even if time variations are present.

Total Power in the Gas

The total power in the gas is determined by subtracting from the total delivered electrical power that portion which is transferred to the walls. Since all surfaces in the vicinity of the arc are water cooled, the heat rejection can be determined by monitoring the coolant flow rates and their temperature rise through the device. The coolant temperature rise is measured with calibrated thermistor transducers of our own design. The output of

these transducers is monitored by strip recorders. Heat rejection to the cathode and anode are monitored separately. In addition, an indication of the symmetry of the jet is obtained by the use of multiple transducers which sample the coolant from different azimuthal portions of the anode.

Magnetic Field Coil Current

The current to the field coil is monitored by a 500 amps equal 50 mv series shunt. Its output is displayed on a strip recorder which indicates any time variations in the magnetic field. We note here that all of the above recorders are time correlated so that the effect of a change in any parameter can be correlated to simultaneous changes in any other measured parameter.

Thrust Measurements

In general, one may write for any steady state, self-contained propulsive device that

$$T \equiv \int_A (P + \rho u^2) dA = \int_{exit} \left[(P - P_{amb}) + \rho u^2 \right] dA_{exit} \qquad (1)$$

or, in differential form, and for $P_{amb} \sim 0$

$$\frac{dT}{dA} = P_{exit} + \rho u^2 \quad . \qquad (2)$$

Then, since for a perfect gas $\gamma P M^2 = \rho u^2$, we can write:

$$\frac{dT}{dA} = P_{exit} \left[1 + \gamma M^2 \right] \qquad (3)$$

or

$$\frac{dT}{dA} = \rho u^2 \left[1 + \frac{1}{\gamma M^2} \right] \quad . \qquad (4)$$

A continuum pitot tube measures in impact pressure

$$P_{impact} = f\left[\gamma, M^2\right] P_{exit} \quad , \qquad (5)$$

while a small flat plate normal to the flow feels a force per unit area

$$F = C_D \tfrac{1}{2} \rho u^2 \quad . \tag{6}$$

Substituting these last relations into Eqs. (3) and (4), one obtains the relation

$$\left.\frac{dT}{dA}\right]_{\substack{\text{pitot}\\ \text{tube}}} = \frac{P_{\text{impact}}}{f(\gamma,\ M^2)} \left[1 + \gamma M^2\right] \tag{7}$$

$$\left.\frac{dT}{dA}\right]_{\substack{\text{thrust}\\ \text{plate}}} = \frac{2F}{C_D} \left[1 + \frac{1}{\gamma M^2}\right] \quad . \tag{8}$$

It is found, by evaluating f of Eq. (5) that for reasonable values of γ and all values of M^2, $(1 + \gamma M^2)/f$ ranges at most from 1 to 1.3 and hence, represents less than a 30% correction factor.

The behavior of pitot tubes in flow regimes where the appropriate mean free path is greater than or equal to the probe diameter is not well known, especially when gas dynamic reactions, for example, recombination and very large temperature gradients are present. It appears at this point that discrepancies of several orders of magnitude from continuum relations are possible under these conditions.

For these reasons, it has become necessary to use thrust plates, which make necessary Mach number corrections (at $M < 2$ to 3), for the measurement of local thrust density. We then write, for an axisymmetric jet, the relation

$$T = \left[1 + \frac{1}{\gamma M^2}\right] \int_0^{\infty} F_{\substack{\text{thrust}\\ \text{plate}}} \, 2\pi r \, dr \quad . \tag{9}$$

With a measurement of the stagnation enthalpy and the average gas velocity, the average equilibrium Mach number can be computed, and hence, the above correction factor is obtained.

The average velocity is computed in the following manner:

$$\bar{u} = \frac{\int_0^\infty \rho u^2 \, 2\pi r dr}{\int_0^\infty \rho u \, 2\pi r dr} = \frac{\int_0^\infty \rho u^2 \, 2\pi r dr}{\dot{m}} \tag{10}$$

The gas enthalpy is computed as follows:

$$P_{gas} = \dot{m} h_o = \dot{m} h + \dot{m} \frac{\bar{u}^2}{2}$$
$$\therefore \; h = P_{gas}/\dot{m} - \bar{u}^2/2 \tag{11}$$

Equation (11) yields h, and assuming that the gas pressure is of the order of the nozzle back pressure, the sound speed can be obtained from a Mollier diagram. It is found that the sound speed is a very weak function of gas pressure over the range of interest. As a check on this approximation, one can calculate the average pressure by

$$p = \overline{\rho u^2}/\gamma M^2 = \frac{\int_0^{R_o} \rho u^2 \, 2\pi r dr}{\pi R_o^2 \, \gamma M^2} \tag{12}$$

where R_o is taken to be the point at which the integral reaches 95% of its final value. The Mollier diagram can then be consulted to complete the iteration loop and provide a self-consistency check.

As an example of this computation, let us consider the following example where the uncorrected specific impulse was 2350 sec.

$\dot{m}$ = .05 gms/sec hydrogen
I = 900 amps
V = 75 volts
B $\simeq$ 1000 gauss (at tip of cathode)
Q_{total} = 18.4 kw (heat rejected to anode and cathode)
P $\simeq$ 10^{-3} atm

Then, Eqs. (10) and (11) yield

$$\bar{u} = 2.3 \times 10^4 \text{ m/sec}$$

$$h = 7.1 \times 10^8 \text{ m}^2/\text{sec}^2$$

Then from a Mollier diagram[9] for hydrogen

$$a = .97 \times 10^4 \text{ m/sec}$$

$$T = 8000^\circ\text{K}$$

Hence

$$M = 2.4$$

and

$$\left[1 + \frac{1}{\gamma M^2}\right] = \begin{matrix} 1.16 \rightarrow \gamma = 1.4 \\ 1.13 \rightarrow \gamma = 1.67 \end{matrix}$$

Therefore, there is a 13% to 16% correction depending on ones choice of γ. Hence,

$$I_{sp} = 2600 \text{ sec.}$$

The fact that I_{sp} is not given here by $\bar{u}/g$ is due to the fact that sufficient expansion has not yet occurred for the thrust density to be given accurately by ρu^2.

Similar computations show that in the desired range of operation of the MAARC in all propellants the Mach number will be large in our facility, hence, the correction factor will be quite close to unity. For this reason, a Mach number correction factor of unity is used throughout this report. In all cases, then, the thrust measurements are underestimates of the actual thrust with respect to the Mach number correction factor. Note also, that a drag coefficient of 2 is assumed for all data presented in this report.

Figure 5 shows a schematic drawing of the ρu^2 probe. It consists of a 3/4 inch diameter, 1/8 inch thick tungsten disk firmly secured to a long 1/16 inch diameter tungsten rod. This rod contacts and deflects a model UC 3 Statham Transducing Cell, or a 0.005 inch thick brass beam with strain gauges attached. The back of the thrust plate and the rod are shielded from the flow by a 3/4 inch outside diameter water cooled jacket. A photograph of this system using the brass beam is shown in Fig. 6. Frictional contact between the rod and the jacket is eliminated by hanging the disk-rod assembly concentrically inside the jacket by a single 3 mil tungsten wire placed at its center of gravity. This tungsten support wire is electrically

and thermally insulated from and connected to the rod by a small ceramic cylinder placed around the rod. The thrust plate and support rod are radiation cooled. The system is calibrated in place by applying known forces to the plate and observing the strain gauge output. The calibration is linear. In addition, data obtained with a $1\frac{1}{2}$ inch diameter tungsten plate and a 3/4 inch diameter quartz plate agreed with ρu^2 integrals obtained with the 3/4 inch tungsten plate. This system is mounted on a mechanism which transports it radially through the arc exhaust. The traversing mechanism has an electrical output which is used to drive the horizontal trace of an oscilloscope. The thrust plate output is displayed as the vertical deflection. The resulting oscillogram yields ρu^2 as a function of radius. Several typical traces are presented in Figs. 7 and 8. A computer program is supplied with data from these oscillograms, calibration factors and conversion constants, and performs the integration in Eq. (9).

Local Mass Flow Density Measurements

Several requirements must be met for the satisfactory operation of a ρu probe. In the operating range of the MAARC, the mean free path, λ, will be greater than 10^{-2} cm in cold flow, and even larger in hot flow. The characteristic diameter of the ρu probe opening is of the order of 10^{-1} cm. Hence, at the inlet of the probe and in the internal regions of the chamber and piping, there will be free molecule or near free molecule flow. The two basic conditions which must be met under these conditions are that the pressure ratio across the probe be sufficiently large so that there will be negligible back flow from the probe chamber into the tank. Also, since a particle striking the side walls of the opening will be diffusely reflected, and hence will have a probability of flowing back out of the opening, the ratio of the length of the opening to its diameter must be kept small; that is, the inlet must be made to look like a free molecule orifice. Therefore, in the free molecule limit, we may write these requirements as

$$\text{(A)} \qquad \frac{P_{\text{static in exhaust}}}{P_{\text{chamber of } \rho u \text{ probe}}} \gg 1 \quad \text{say} > 100$$

$$\text{(B)} \qquad \text{L/D of probe opening} \quad < \quad 1 \quad \text{say} \quad 1/4 \quad .$$

The latter case was computed by Clausing[10] in the free molecule limit for the case of no average flow velocity and with a pressure ratio of infinity. These results are summarized by the Clausing factor defined as

$$K = \frac{\dot{m}}{\frac{\rho\bar{c}}{4} A} \quad , \tag{13}$$

where $\dot{m}$ is the actual mass flow into the probe, ρ and $\bar{c}$ are the upstream density and average thermal velocity, and A is the area of the probe opening. As examples of this effect, for L/D = 0, .1, .5, 1 and 5; K = 1.0, .91, .67, .51 and .20.

Narasimha[11] has computed the increase in mass flow into an orifice due to finite values of λ/D, and again with an infinite pressure ratio, and has found that

$$\frac{\dot{m}}{\dot{m}_{\frac{\lambda}{D} \to \infty}} = 1 + \frac{1}{8} \frac{D}{\lambda} \quad . \tag{14}$$

This computation was verified experimentally by Liepmann[12] for λ/D down to about 1/2.

Hence, for $\lambda/D > 1/2$, we may write as the mass flow into a ρu probe from a static environment (i.e., no average flow velocity) when requirement (A) previously is satisfied,

$$\dot{m} = \frac{\rho\bar{c}}{4} A K \left(1 + \frac{1}{8} \frac{D}{\lambda}\right) \quad . \tag{15}$$

If a bulk flow is superimposed upon this background then

$$\dot{m} = \frac{\rho\bar{c}}{4} A K \left(1 + \frac{1}{8} \frac{D}{\lambda}\right) + \rho u \tag{16}$$

or

$$\frac{\dot{m}}{\rho u} \simeq 1 + \sqrt{\frac{1}{2\pi\gamma}} \left(1 + \frac{1}{8} \frac{D}{\lambda}\right) \frac{1}{M} \quad . \tag{17}$$

Since K and D/λ will be small and the Mach number, M, will be large in

hot or cold flow, $\dot{m}$ will be quite close to ρu. There should perhaps be some type of Clausing factor associated with the ρu term above, however, this will best be evaluated experimentally. If it is satisfactorily close to unity in cold flow, it will certainly be unity in hot flow since the particles leaving the wall will have a much lower $\bar{c}$ than the incoming particles.

Figure 9 shows a schematic drawing of the ρu probe. It consists of a 90% tantalium-10% tungsten tip with conical inner and outer surfaces. This alloy was chosen because of its high melting temperature and good machineability. The conical surfaces have 19° and 30° half angles respectively, and meet to form a very sharp edged opening of about 1/32 inch diameter with an L/D much less than unity. This tip is held in a water cooled jacket whose surfaces match those of the tip. The probe is connected to a large water cooled cylinder which is continuously evacuated by a 2 inch booster diffusion pump. Pressure transducers are placed within the cylinder and at the inlet of the pump to act as measures of the mass flow through the system. The vacuum pumps are connected to the system with flexible tubing so that the ρu probe is free to move on the traverse mechanism described in the last section. In this way, continuous ρu measurements as a function of radius are obtained in a single run.

The ρu probe system is calibrated in two ways. First, a simple constant pressure oil displacement flowmeter is connected to the probe inlet and the pressure readings on the two transducers are noted. In this way, the pressure readings can be directly related to the mass flow through the system. The probe is then placed in the MAARC vacuum tank and room temperature hydrogen is bled into the vacuum tank. The mass flows measured in this way, for ambient pressures from .01 to 1 mm Hg are compared with Eq. (15). Since the measured pressure ratio for the ρu probe ranges from 20 to 30, criteria A is reasonably well satisfied. The comparison of the measured and computed mass flows then gives a K of .95 and hence an effective L/D for the ρu probe of much less than unity. We, therefore, conclude that the ρu probe described above satisfactorily satisfies the requirements established for its proper operation. Figure 10 is a photograph of the ρu probe in place in the MAARC facility.

Figures 11 and 12 are typical ρu profiles obtained in hydrogen in cold and hot flow together with ρu^2 profiles obtained under corresponding conditions. The data shown here was obtained in hydrogen at power levels ranging from 50 to 60 kw, and mass flows of .05 and .03 gms/sec. The medium water cooled coil with the trimmer coil adding was used. The upper trace on the ρu oscillograms, labeled "I", is the output of a Pirani type NRC Autovac vacuum gauge placed in the chamber just behind the ρu probe. The lower trace, labeled "II", represents the output of a Phillips type NRC ionization gauge located near the inlet of the booster pump used to pump the ρu probe. These gauges are separately calibrated and hence give independent measurements of the mass flow through the ρu probe. This method is used to indicate any possible effects due to electromagnetic pickup or thermal drift. Since the two gauges are of entirely different types and are located a large distance apart, the above unwanted effects would be manifest clearly by a large discrepancy in the results obtained with the two gauges.

Noted on the ρu oscillograms are three radii defined as follows:

1. R_o is the radius obtained from the ρu^2 profile, at which the measured thrust reaches 95% of its final value.
2. R_I is the radius obtained from the upper (Autovac) ρu profile, at which the computed mass flow equals the total mass flow through the MAARC.
3. R_{II} is the radius obtained from the lower (ionization gauge) ρu profile, at which the computed mass flow equals the total mass flow through the MAARC.

The use of a ρu probe in ammonia is made difficult because it recombines to form H_2 and N_2. A scheme has been devised to circumvent this problem with the use of the two different pressure gauges. Since these gauges have different sensitivities for ammonia, hydrogen, and nitrogen, it is possible with proper calibration that measurements of the pressure difference and pressure ratio from the two gauges will not only yield the local mass flow but also the relative species concentrations and hence a measure of the degree of dissociation.

Axial Current Distribution Measurements

The axial current distribution can be easily deduced from measurements of the azimuthal component of the magnetic field, B_θ, induced by these currents. By measuring B_θ at a radius r one determines the total current passing through the loop of radius r which is concentric with the axis. This current is given by

$$I_Z(\text{amps}) = \frac{1}{5} \frac{B_\theta(\text{gauss})}{r(\text{cm})} \quad . \tag{18}$$

This current starts at zero at the centerline and increases with radius to a maximum value which corresponds to the total axial current at that axial position. It then decreases to zero as these currents return to the anode.

The determination of B_θ is made by integration of the measured value of dB_θ/dt obtained by a small search coil, whose axis is aligned to the azimuthal direction, as the MAARC is turned off. This measurement is repeated at various radial positions to obtain the distribution of I_Z. In Fig. 13 a schematic drawing of this search coil is shown indicating the details of its construction and the associated integrating circuit. The center ground construction of this coil is used to eliminate electrostatic signals. In addition, the coil and all electrical leads are surrounded by an electrically grounded shielding to further prevent electrostatic pickup. The output of this circuit is directly proportional to B_θ, the computed calibration constant having also been checked experimentally. In Fig. 14 another schematic drawing shows the placement of this coil in the MAARC facility.

In Fig. 15 an ensemble of B_θ measurements is presented. This data was obtained with .05 grams/sec hydrogen. The time constant for the integrating circuit was 40 ms whereas the measurement of dB_θ/dt directly, as also shown in this figure, indicates that it lasts for only 2 ms. This assures the proper functioning of the integrating circuit. The B_θ measurements are displayed at a sweep speed which is long compared to the time constant of the integrating circuit so that the zero level can be accurately determined. The distance between this zero level and the plateau of the trace is directly proportional to B_θ. Note that B_θ reverses sign as we pass through the centerline, then increases to a maximum value and then decreases to zero

far from the centerline just as it should. The upper trace on these oscillograms is the arc current. It was used in triggering the oscilloscope.

SECTION IV

EXPERIMENTAL AND THEORETICAL RESULTS

The overall operating conditions of the MAARC for data presented in this report, which are not specifically described below, are summarized in the following table:

Propellant	$\dot{m}$(gms/sec)	IV(kW)	B(gauss)	$\eta_{\text{thermal}}^{\text{average}}$
Hydrogen	.01-.05	35-66	0-4000	55-90%
Argon	.1	22	1250	50-85%
Nitrogen	.05	26-38	500-1325	40-90%
Ammonia	.02-.10	10-78	500-5500	25-75%

$\eta_{\text{thermal}} \equiv$ Total Power in GAS/IV

Current-Voltage Characteristics

The MAARC voltage at fixed hydrogen mass flow rate versus current using the large heat sink coil to produce the bias field is shown in Fig. 16. For bias fields less than 750 gauss at the cathode tip, the MAARC voltage increases with current; for bias fields greater than 750 gauss, the MAARC voltage decreases with current. This variation in current voltage characteristics with bias field intensity is an additional manifestation of the important effect that the bias field has on the current configuration.

A possible explanation for this dependence of the voltage on B field can be given as follows. For zero applied magnetic field, the lowest curve in Fig. 16, an increase in arc current increases the voltage indicating that the plasma conductivity in the absence of a magnetic field does not change appreciably with an increased power input. When a bias field is applied which is sufficiently strong to make the arc run uniformly off the cathode tip (that is, above 500 gauss at the cathode tip), the slope of the voltage versus current curve is greatly reduced. At this magnetic field, the Hall effect becomes important and the currents are forced to run in the expanding portion of the nozzle. A further increase in the applied magnetic field increases the Hall current for a given arc current which results in an increased concentration or pinching of the plasma toward the axis. This results in an increase in the average enthalpy in the gas with a corresponding increase

in the degree of ionization. The expression for the conductivity in the plasma is a function of $\omega\tau$ or the magnetic field and ion density can be given as follows:

$$\sigma = \frac{\sigma_o}{1 + (\omega\tau)^2} = \frac{\sigma_o}{1 + \left[\frac{Be}{m_e} \frac{1}{N_i Q_{Ie} \bar{c}_e}\right]^2} \tag{19}$$

When the magnetic field is very high, an increase in power level at a fixed mass flow increases the ion density which lowers the mean time between collisions for the electrons thereby reducing $\omega\tau$ and raising the effective electrical conductivity. This effect was experimentally and theoretically discussed in Ref. 13. Hence, the rapid decrease in arc impedance with increasing arc current (power) results in the lowering of the arc voltage with increasing current at very high magnetic fields.

V-B Characteristics

During the course of our investigation, we have observed that the overall operating voltage of the MAARC is a linear function of the applied bias field strength. The slope of these V-B characteristics is found to depend primarily upon the propellant and bias field geometry, possessing only a very slight dependence on mass flow and power level over the range of operating conditions studied. This data is presented in Figs. 17, 18 and 19, where the overall MAARC voltage is plotted as a function of the magnetic field strength at the cathode. Plotted also in these figures are curves obtained from a theory which describes the voltage in an ionizing plasma with a strong magnetic field where the dissociation and ionization processes dominate.

Several authors[14, 15] have investigated such discharges in magnetized plasmas and have discovered that the voltage drop in the plasma is connected with a critical ionization speed.[14] This "burning voltage" - "critical speed" relationship was first pointed out by Alfven[14] and a suggested partial explanation for this was given by Petschek.[14] This rough theory as it applies to the MAARC geometry is presented below.

Let us consider that region of the MAARC where the incoming room temperature gas first starts carrying current (Fig. 1) and let us further restrict ourselves to that portion of the flow which is uninfluenced by the cathode and anode surfaces, i.e., the portion near the middle of the channel. In this region, we take the current density, j, and the local electric field, E, as both being radial, and the magnetic field, B, as axial. Then, the electrical input power per unit volume to the gas, P_{in}, is given by

$$P_{in} = jE \tag{20}$$

If we assume that the gas enters this region with negligible enthalpy and exists from this region highly dissociated and ionized, then we can write the energy equation as

$$\dot{n}\left[\mathcal{E} + C_p T + \frac{m\bar{U}_I^2}{2}\right] = P_{in} = jE \tag{21}$$

where $\dot{n}$ is the incoming number density flow rate, $\mathcal{E}$ is the energy per incoming particle invested in dissociation and ionization, T is the exit temperature and U_I is the velocity of the exiting ions.

If we now consider the azimuthal component of the momentum equation, then we find that

$$jB = \dot{n}[mU_I] \tag{22}$$

Note that the $\vec{j} \times \vec{B}$ forces in this region merely swirl the flow resulting in an azimuthal U_I.

Since we are postulating a region where dissociation and ionization processes are dominant, it is reasonable to presume that the plasma temperature is much less than the energy necessary to dissociate and ionize (which is of the order of 10 eV or more). Hence, we assume that

$$\mathcal{E} \gg C_p T$$

With this assumption, we can combine Eqs. (21) and (22) and obtain

$$E/B = \frac{\mathcal{E} + \frac{mU_I^2}{2}}{m\bar{U}_I} \tag{23}$$

Further, if the magnetic field is sufficiently strong so that $\omega_e \tau_e \gg 1$ the ions will very nearly drift with the local E/B velocity,[16] that is, $U_I = E/B$, hence

$$E/B = U_I = \sqrt{\frac{2\mathcal{E}_{ionization}}{m_I}} \tag{24}$$

This argument is correct for the ionized portion of the gas passing through the ionization region. The assumption is made in Eq. (24) that $\omega_e \tau_e$ is large enough so that the ions nearly move at the local E/B velocity. This corresponds to ion slip[16] where there is insufficient drag on the ions by the neutral gas to inhibit their drift with the E/B velocity.

Equation (24) defines a critical speed for a molecule which is the velocity a molecule must have so that its kinetic energy equals the energy necessary to ionize and/or dissociate it. This velocity for the propellants used is summarized in the table below. If this process describes the ionization process in the MAARC, it will also describe the voltage for the whole device because $\omega_e \tau_e \gg 1$, there will be very little voltage gradient along the B field lines. To be more specific, except for the regions in the flow immediately downstream from the cathode and near the anode, the voltage along each B field line will be nearly constant because the electron mobility is several times greater parallel to the B field compared to the mobility perpendicular to the B field. Hence, for the central portion of the discharge, the initial ionization can fix the electric field for the whole flow. To check this hypothesis, we may integrate Eq. (24) and write

$$V = V_o + (U_c B)\ell \tag{25}$$

where V_o is an integration constant and represents in part a voltage drop associated with the electrodes, that is, near the cathode and anode, U_c is the critical speed, B is the magnetic field intensity in the ionization region, and ℓ is a characteristic radial dimension of the arc near the upstream region of the discharge. Equation (25) was used for the theoretical lines in Figs. 17, 18 and 19. The following table summarizes the values for U_c, ℓ, and V_o for Fig. 17.

$$\tfrac{1}{2} m U_c^{\,2} = \mathcal{E}_{\text{dissociation}} + \mathcal{E}_{\text{ionization}}$$

Critical Speeds and Electrode Voltages
(Large Heat Sink Coil)

Propellant	U_c	V_o	ℓ
Hydrogen	5.5×10^4 m/sec	45 volts	1 cm
Nitrogen	1.6×10^4 m/sec	30 volts	1 cm
Argon	$.87 \times 10^4$ m/sec	15 volts	1 cm
Ammonia	2.6×10^4 m/sec	36 volts	1 cm

$$V = V_o + U_c B \ell$$

The values for U_c are determined by the chemical structure of the propellent molecules, ℓ is the same for all conditions, depending only upon the flow geometry, and V_o was determined empirically.

In Fig. 17, the MAARC voltage versus B field intensity for a large heat sink coil (Fig. 1) is shown. The data is for several different propellants. The critical speed in ammonia was calculated before the MAARC was operated in ammonia and there was a strong indication that the MAARC voltage would

be relatively high using this propellant, since U_c for ammonia is relatively high (2.6×10^4 m/sec). This number is based on the 69 eV required for the reaction $NH_3 \rightarrow N^+ + 3H^+ + 4e$.

In addition, data is shown in Fig. 17 using hydrogen as a propellant for several different mass flows. This data indicates that the MAARC voltage agrees with the theory express in Eq. (25) for a large range of mass flows in hydrogen with the same field coil.

If lines are drawn through the data for each propellant, connecting points obtained during a single run, it is found that all these lines have roughly the same slope. (See Fig. 20 for example.) This observation leads to the conclusion that scatter in the data appears to be due to changes in the quantity V_o from run to run. A particular example of this effect is presented in the following section.

The voltage versus B field intensity characteristics using the medium sized coils are shown in Figs. 18 and 19. In Fig. 18, the data is for hydrogen and the theoretical line for the large heat sink coil is also shown. It can be seen by inspecting Fig. 18 that the slope of the MAARC voltage versus B field curve is less for the medium sized water-cooled coil than it is for the large heat sink coil. The data for ammonia is shown in Fig. 19, where the results obtained using the large heat sink coil are also shown, and the same trend as that obtained in hydrogen is obtained where the slope of the V vs B curve is smaller for the medium sized coil.

Therefore, the voltage characteristics of the MAARC depend both on the magnitude of the bias magnetic field and geometry of the B field. The bias fields produced by smaller coils have a larger radial component, and produce a discharge in the MAARC which is less sensitive to changes in the B field. This corresponds to a smaller value of ℓ in Eq. (25); data on Figs. 18 and 19 show slopes for the medium coils that correspond to $\ell = 0.4$ cm rather than 1 cm for the large coil. This indicates that the ionizing portion of the discharge is forced further upstream with a more divergent B field, because the small value of ℓ indicates a shorter initial length of the discharge.

Thus, it appears that a more nearly axial bias field forces the ionizing portion of the discharge (the most upstream portion) out into the expanded portion of the anode nozzle.

Mode Changes in the MAARC

Under two apparently unrelated conditions, mode changes have been observed in the MAARC.

If the magnetic field is held constant, and the arc current reduced, a minimum current is observed for which the MAARC is stable. Also, if the current is held constant and the magnetic field reduced, a minimum field is observed for which the MAARC is stable. In the unstable mode, the arc does not appear to be uniform and a large amount of erosion occurs at the

anode. There are indications that these effects are closely related and the data suggests that a quantity like the sum of the arc current and coil current must be above a certain value for stable operation. This is further suggested by the data at very high arc currents where no magnetic field is needed for stable operation. It is not unlikely that this critical combination of arc current and magnetic field strength is such that the sum of the induced and applied magnetic field strength is such as to just make $\omega_e \tau_e$ for the electrons equal to unity.

A second type of mode change manifests itself in changes in arc voltage. In Fig. 20 a plot of arc voltage vs magnetic field strength obtained in ammonia with the medium water-cooled coil and the trimmer adding is presented. The data on this figure which is plotted with unflagged symbols represents data obtained at a fixed cathode location which for identification purposes is called the "normal" position of the cathode. This normal position was 1-7/32" upstream of the exit plane of the nozzle. As can be seen from this data, there appears to be two distinct voltage modes present in the MAARC which manifest themselves as changes in the quantity V_o. Changes between these modes in times ranging from less than 1 to 10 or 15 seconds occurred during a run, while all external parameters were held constant. However, most often the arc would initially light and remain in one or the other of these modes. In addition, at 10 mgs/sec and high magnetic field strengths, the MAARC would change into a third voltage mode and run unstably at a meter reading of over 200 volts for a period of seconds, and then either drop to a lower voltage mode or extinguish itself. It is most likely that this very high voltage mode represents a condition where the MAARC is rapidly extinguishing and relighting itself, although this has not not yet been documented.

To determine what controls these voltage modes, the effect of cathode location was studied. The data obtained at positions other than the normal cathode location is shown on Fig. 20 with flagged symbols. It was observed that when the cathode was moved downstream from its normal position, the MAARC always operated in the low voltage mode; also, inspection of the cathode indicated that currents were being emitted near the sides of the cathode rather than from the very tip. As the cathode was moved upstream from its normal position, the MAARC operated unstably, switching randomly between modes and occasionally producing cathode erosion. Eventually an upstream position was reached where the arc ran continuously in the high voltage mode with visual evidence that the currents were emanating from the very tip of the cathode. In between these extreme cathode locations, several runs were made in which the arc ran quite steadily at intermediate voltages. The effect of cathode location on the arc voltage is shown in Fig. 21. It is felt at this time that the mode changes in arc voltage are due primarily to the location of the currents on the cathode which appears to effect the quantity V_o of Eq. (25) and that the MAARC can be stabilized by moving the cathode sufficiently far up or downstream, or by improved shaping of the cathode and the quartz insulator.

Anode Heat Transfer Results

Based on the V-B characteristics described above, one would expect the anode heat transfer to be related to the product of the arc current and the quantity V_o. Since, in any given mode the quantity V_o is constant, the anode heat transfer should be related only to the arc current. If several modes are present, as above, the one possessing the lowest V_o should yield the lowest anode heat transfer at a given arc current.

In Fig. 22 data is presented showing the dependence of the anode heat transfer on the arc current. The power supply for the MAARC is so constructed that in this operating range, large changes in arc voltage produce much smaller changes in arc current; for example, a change in arc voltage from 50 to 100 volts produces only a 20% decrease in arc current. During any given run, the arc voltage was changed by changing the magnetic field, while the arc current changed very slightly. It was observed that under these conditions of constant current and V_o during a run, the anode heat transfer was also quite constant, hence, each point on Fig. 22 represents one complete run. As has also been observed by other investigators, the anode heat transfer seems to be a function of the arc current only for a constant value of V_o. Comparison of the data in Fig. 22 shows good agreement with similar data reported by R. John et al.[17] The line plotted in Fig. 22 was obtained by linear extrapolation of this data to lower arc currents, since their experiments were at arc currents in excess of 600 amps. In this figure, the open symbols correspond to the low voltage mode whereas the solid symbols were obtained in the high voltage mode. The trend of the data indicates quite clearly that there is a higher anode heat transfer at a given arc current when the MAARC is operating in the high voltage (high V_o) mode.

Figure 23 contains a summary of thermal efficiencies vs electrical power input obtained in ammonia in the MAARC. The thermal efficiency is defined as the ratio of gap power to total electrical input power. The lines drawn on this figure connect typical sets of data points obtained during a single run in which only the magnetic field strength varied and no mode change occurred - movement from left to right corresponds to increasing magnetic field - the solid symbols correspond to data obtained in the high voltage mode, and the open symbols in the low voltage mode. This data again demonstrates that the low voltage mode is more efficient.

Figure 24 contains data obtained in hydrogen. This data suggests at first that it is in contradiction with the trend observed in ammonia, however, these results were obtained in such a way that each point was obtained in a different run. Examination of the V-B characteristics for this data indicates that there were large changes in the quantity V_o from run to run. Therefore, this data would not be expected to follow the trend evident in ammonia at constant V_o. It is also worthwhile to point out that the thermal efficiency in hydrogen is in general higher than in ammonia. This appears to be due to the fact that the V-B characteristic is steeper for hydrogen than for ammonia.

The thermal efficiencies of Fig. 24 were plotted for the data appearing in Fig. 26. It can be seen by inspecting Fig. 24 that the thermal efficiency was slightly above 80% for nearly all the runs, while inspecting Fig. 26, one can see that the thrust varied over a large range for a nearly constant power input. Therefore, for this configuration, the thrust efficiency is not dependent on the fraction of the total power delivered to the gas, but depends on the current and B field configuration in the flow and the ratio of the energy delivered to accelerate the gas compared to the energy invested in heating and ionizing the gas. The same comparison can be made for the other coils and other propellants. Similar data was obtained with the medium sized heat sink coil for a large range of arc current and B field intensities.

If one looks at all of the data obtained in hydrogen with a given coil configuration, for instance, the large heat sink coil, the power delivered to the anode measured with the heat balance technique shows that the anode heat transfer can be described as a voltage drop between 10 and 30 volts with a distribution between these two voltages as a function of arc current and/or mass flow in hydrogen.

Based on the above ammonia data, the following observations can be made:

1. The value of V_o can be controlled through changes in cathode location.

2. Smaller values of V_o lead to lower anode heat transfers and higher thermal efficiencies.

3. At any given V_o, increases in magnetic field strength produce higher thermal efficiencies.

4. There is a strong indication that the thermal efficiency at any given power level can be increased by applying the highest possible magnetic field and reducing the arc current proportionately.

5. There is an indication that increased mass flow reduces anode heat transfer.

Thrust Measurements

Oscillograms Showing ρu^2 Versus Radius

In Fig. 7 some typical oscillograms of the thrust plate output versus radius are presented with the associated scale factors. These profiles are used to obtain both the shape of the ρu^2 profile and the overall thrust. The overall thrust is obtained from these oscillograms by integrating the area under these curves on the oscillogram as described in the section on diagnostic techniques.

The overall shape of these thrust profiles for different propellants and bias field intensities with a given bias field coil are quite similar. For sufficiently intense bias fields, Hall effects dominate the current pattern and the currents emanate from the tip of the cathode and flow in the expanded portion of the 50° nozzle. This gives rise to a characteristic thrust profile for all propellants, mass flows and for a very wide range of bias field shape and intensities.

In Fig. 7, oscillograms of the ρu^2 profiles for cold flow at .05 gms/sec hydrogen is shown for comparison to the hot flow results. Also, a hot flow oscillogram obtained with no bias field at all is shown for comparison. The cold flow ρu^2 oscillogram yields an average exit velocity which is in reasonable agreement with the calculated value based on the observed pressure and area ratios for the nozzle. It can be seen that for the normal operating condition, compared to that with no bias field, the overall shape of the ρu^2 profile is drastically altered by the addition of the bias field. It is interesting to note that the thrust profile in ammonia has a decrease at the center similar to that obtained in argon at high mass flows.[1] In Fig. 8, there are two oscillograms showing the thrust profiles obtained with argon and nitrogen which also have the same characteristic shape as that obtained with hydrogen and ammonia, shown in Fig. 7. The effect of the magnetic field on the magnitude of these signals and the overall integral which leads to the thrust measurement is discussed in the next section.

It has been observed that the general shape of our ρu^2 oscillograms is such that the quantity $\rho u^2 r$ appears to be nearly constant over a large region of the flow. This fact is demonstrated in Fig. 25 where the fraction of the total thrust existing between the centerline and a radius r is shown as a function of r. This information should be quite useful in any analytic study of the flow in the exhaust of the MAARC.

Effect of Magnetic Field on Thrust

For our experiments, the total current delivered to the gas was nearly always less than 1000 amperes. The magnetic field due to a concentrated axial current can be written.

$$B_i = I/5r \tag{26}$$

where B_i is the induced azimuthal field due to arc currents in gauss, I is the current in amperes, and r is the radius in centimeters. For an arc current equal to 10^3 amperes, this field is less than 200 gauss for radii in excess of 1 centimeter. Most of the integrated thrust from the ρu^2 profile occurs at relatively large radii. Hence, for our operating conditions, the bias field (which always exceeded 200 gauss for efficient operation) always exceeded the induced field in the major portion of the plasma flow.

We have studied the effect of varying the field strength at constant propellant mass flow and relatively constant input power for the various field coils described above. These results are presented in Fig. 26 through

30 in the form of IB vs T plots, where I is the arc current and B is the magnetic field expressed in terms of current through the coil. The results obtained with our large and medium sized heat sink coils provide a clear indication of the optimum in MAARC performance in hydrogen and ammonia (Figs. 26, 27 and 28), however, the water-cooled coil does not completely demonstrate this effect (Figs. 29 and 30). Operation with this coil in hydrogen seems to indicate that the optimum exists below the range of IB products investigated (Fig. 29) whereas the ammonia data indicates that this optimum exists above the range of IB studied (Fig. 30). The medium sized heat sink and water-cooled coils differ very slightly in field geometry but produce relatively large differences in performance.

The MAARC has been operated in hydrogen and ammonia using the trimming coil described above. The trimming coil was placed around and connected in series with the medium-sized water-cooled coil in such a way that the magnetic field of the trimming coil either added to or subtracted from that of the medium-sized coil. Note that the trimmer coil changes the magnetic field at the cathode tip by approximately $\pm$ 10% at a given coil current. It was observed that an increase in thrust was obtained when the trimmer coil current was bucking the current in the inner coil compared to the thrust obtained with the inner coil alone. When the current in the trimmer coil was in the same direction as the inner coil current, the thrust was reduced. At the same B field intensity, mass flow and power level, the thrust was increased approximately 10% by using the trimmer in the bucking mode, and decreased by 10% with the trimmer coil adding. In addition, we have observed a marked variation in thrust with the IB product at constant $\dot{m}$ and essentially constant power level. Since the range in IB products covered was quite small, an optimum value of IB was not always apparent.

In Figs. 31, 32 and 33, several ρu^2 profiles are reproduced. Figure 31 shows points on the lower portion of Fig. 26 and Fig. 32 on the upper portion. Note that as the IB product increases, the profiles grow until the optimum is reached. Increasing IB further produces a pinching of the jet and a resulting decrease in thrust. The data in Fig. 33 shows that the thrust profiles obtained with the smaller coils which produce a larger radial B field are less pinched. The profiles shown are for operating conditions very near the optimum values for maximum thrust and efficiency.

An explanation for the character of this data is given as follows. The thrust plate profiles for large bias field intensities show a concentration of ρu^2 near the axis with very little ρu^2 in the flow at relatively large radii. This indicates that for too large a bias field, the azimuthal Hall currents pinch the plasma on the axis to such an extent that most of the j x B forces are directed inwards with a smaller magnitude of the following dot product

$$(\vec{j} \times \vec{B}) \cdot U_x$$

where j is the current, B is magnetic field, and U_x is the axial component of the plasma velocity. For very low bias field intensities, the arc current

pattern was seen to tend to form spokes and local anode spots, resulting in relatively large wall heat transfers and low thrusts.

As the bias field is increased beyond that value necessary for stable operation, the value of $\omega_e \tau_e$ for constant power input increases. Therefore, for a given anode-cathode current, the total current in the nozzle increases, because the Hall currents are completely short circuited, and are proportional to B. Hence, the total current in the flow is proportional to IB, and the integral of $\vec{j} \times \vec{B}$ throughout the volume in the nozzle where the azimuthal Hall currents exist is therefore proportional to IB^2 for these conditons. It can be seen by inspecting the IB vs T plots that for the lower values of IB the thrust is more nearly proportional to IB^2 (dashed curve) than IB. The thrust increases until the optimum magnetic field intensity and then a further increase in B field causes a concentration of the propellant toward the axis with a decrease in thrust.

Thus, there seems to be an optimum bias field intensity for a given operating condition. This bias field must be sufficiently strong to give a large Hall effect and force the arc current to emanate from the cathode tip and run through the expanded portion of the nozzle, but not be too large to cause excessive plasma concentration and high pressure near the axis.

Thrust Stand Measurements

The MAARC has been operated on a thrust stand at the AVCO/RAD facility. The results obtained on this thrust stand in hydrogen and ammonia with the medium-sized water-cooled coil and with the trimmer geometry in the adding mode (for hydrogen only) are shown in Figs. 34, 35 and 36. Also shown on these figures is data obtained with our thrust density probe under similar operating conditions at our own Laboratory. Identical values of the IB product correspond to identical values of both I and B. It can be seen from these figures that a large discrepancy exists in both the magnitude and the functional dependence of the measured thrust on the IB product. There is, however, agreement in the data obtained in ammonia over a portion of the range of IB products. Note that the thrust plate data in ammonia represents a $\pm$ 15% variation in power level. The range in overall efficiencies covered by this data are quite large. The data in Fig. 34 yields overall efficiencies ranging from 10-12% for the thrust stand data whereas the thrust plate data yields a range of from 20-60%. For Fig. 35 these ranges are 10-14% and 10-50%, while for the ammonia data of Fig. 36 they are 15-22% and 3-15%, respectively.

We feel at this time that the discrepancy in the two sets of data is most likely due to differences in the mode of operation of the device at the RAD and Everett facilities. MAARC type devices have been run in the RAD facility with no net propellant through-put, whereas the MAARC could not be operated in our own system under these conditions (see later section). Also, we observed that the MAARC operated at voltages which were up to 10% lower than those obtained in our own installation at identical operating conditions. Based on these observations, it is not entirely surprising that different thrusts were measured at the two facilities.

Specific Impulse and Thrust Efficiency

Figures 37 and 38 are plots of overall thrust efficiency as a function of measured specific impulse. The specific impulse was determined from the ρu^2 measurements using the relation.

$$I_{sp} = T/\dot{m}g \tag{27}$$

where T is the thrust in grams-force and $\dot{m}g$ is weight mass flow of propellant in grams-force/sec. Equation (9) was used to determine T from the ρu^2 profiles. However, no Mach number correction was applied to the integral of this equation. It was found that this correction was insignificant for the data in excess of 2000 sec in hydrogen. The specific impulse results below 2000 seconds would be substantially increased if this correction were applied.

The overall thrust efficiency was computed from the relation

$$\eta_{overall} \equiv \frac{P_{thrust}}{\text{Total Electrical Power Input}} = \frac{\frac{1}{2}\frac{T^2}{\dot{m}}}{IV} = \frac{\frac{1}{2} I_{sp}^2 g(\dot{m}g)}{IV} \tag{28}$$

The solid lines in Figs. 37 and 38 are for fixed input powers and mass flows. These lines were drawn to connect the various points at the same input power and mass flows to point out the variation in η and I_{sp} as the B field is changed.

The data on Fig. 37 show the variation in η vs I_{sp} for three different propellants. All of the data in nitrogen and argon were obtained using the large heat sink coil. The points for hydrogen were with several different coil shapes. The details of the effect of the B field shape and intensity are discussed in the section on the effect of the magnetic field on thrust. The thrust and thrust efficiency obtained with hydrogen using the large heat sink coil depended strongly on the magnetic field intensity at a fixed power level. This was shown in Fig. 26 and is also shown in Fig. 37. The thrust and thrust efficiency was not as steep a function of IB using the medium sized coils (Figs. 28 and 29), but the maximum thrust at a given power level and mass flow was nearly the same for all three B field shapes.

The data obtained using ammonia as a propellant is given in Fig. 38 along with two curves obtained using hydrogen and one for nitrogen, for comparison.

In subsequent sections of this report the effects of entrainment of ambient gas particles on the results presented in Figs. 37 and 38 are discussed in some detail.

ρu Measurements

ρu distributions have been obtained in the MAARC under the following operating conditions.

Propellant:	Hydrogen
Mass flow:	.01 - .05 grams/sec
Power level:	45-65 kW
Magnetic field:	without trimmer: 400-1000 amps
Medium water-cooled coil	
	trimmer adding: 300-1000 amps

Several sample oscillograms obtained in hot and cold flows are shown in Figs. 11 and 12. Based on this data, the following observations and conclusions can be made.

1) In cold flow, there is very good agreement between the ρu measurements obtained with the different gauges and, of greater importance, the jet diameter obtained from ρu and ρu^2 measurements are very closely equal.

2) R_I and R_{II} agree to better than 20% for all operating conditions indicating that there is neglibible drift and/or zero shift in the ρu probe system.

3) R_{II} (or R_I) is found to increase with increasing $\dot{m}$ in such a way that the area of the jet, as determined by R_{II}, is roughly proportional to $\dot{m}$. In addition, R_{II} was insensitive to magnetic field without the trimmer coil but decreased with increasing B when the trimmer coil was used adding.

4) R_o remained roughly constant under all operating conditions.

5) In previous reports we have observed that the profile shapes changed markedly with IB product at constant $\dot{m}$ and essentially constant power level when the large heat sink coil was used. This effect was shown to be far less severe with the other field coils, hence the results noted in Items 3) and 4) above. However, as can be seen from Fig. 12, there are variations in the shape of the ρu profiles with the trimmer coil adding that are quite similar, if not as dramatic, as those observed with the large heat sink coil.

6) Due to the finite back pressure in our vacuum tank, the mass flow into the probe when it is outside the jet is finite and is given approximately by $\frac{\rho \bar{c}}{4}_{ambient} A_{probe}$ where ρ is the ambient density, $\bar{c}$ is the average thermal velocity of the ambient gas, and A_{probe} is the inlet area of the ρu probe. Since the ambient tank pressure has been found to remain essentially constant when the arc is turned on, it can be seen that the mass flow into the probe when it is outside the jet is proportional to $1/\ T_{ambient}$. Thus, when the arc is turned on, the ambient temperature increases and the mass flow into the probe decreases. This effect can clearly be seen in the level changes in the oscillograms of Fig. 12.

Based on the above data, it is felt at this time that the present ρu probe is a dependable and accurate diagnostic for the measurement of local mass flux.

Entrainment of Ambient Tank Gas

To aid in the interpretation of entrainment measurements in MAARC type devices it is convenient to discuss two basic types of entrainment.

The first type of entrainment, which we call $\vec{j} \times \vec{B}$ entrainment, is caused by the presence of ambient gas particles in the acceleration region of the MAARC, that is, the region where arc currents and magnetic fields exist together. Power is delivered directly to the entrained gas in the form of $\vec{j} \cdot \vec{E}$ power from the arc. Ambient gas particles can exist in the acceleration region either because the arc currents are capable of flowing out into the ambient tank gas or because the ambient gas particles are able to diffuse through the exhaust jet into the acceleration region. The thrust obtained from this kind of entrainment is real thrust; however, the total mass flow associated with this thrust must be used in computing I_{sp} and η. This type of entrainment augments the thrust which corresponds to the actual through-put of propellant. It can be eliminated by restricting the arc currents to flow only in the actual propellant and by preventing diffusion of ambient gas particles through the propelland and into the acceleration region. This is best accomplished by removing the ambient gas altogether with the use of a large vacuum facility. However, it may be possible to greatly reduce this type of entrainment by preventing the arc currents from extending out into the ambient tank gas through the use of electrically insulating walls placed at the natural boundary between the propellant and the ambient gas. If, in either of these ways, the propellant can be made to fill the region previously occupied by ambient gas, then the net thrust should remain unchanged. If, in addition, the currents and propellant can be made to occupy a larger volume in space, the thrust may possibly increase. This is a consequence of the fact that the magnetic contribution to the thrust depends only

on $\int \vec{j} \times \vec{B} dV$, that is, the volume integral of $\vec{j} \times \vec{B}$. If this type of entrainment is the dominant one in the MAARC, then we expect that the observations we have made in the past will not be changed qualitatively by replacing ambient gas with actual propellant. Our description of voltage-current and voltage-magnetic field characteristics should remain basically unchanged. An optimum magnetic field strength and shape should still exist although quantitative differences from our past results will most probably occur.

The second type of "entrainment" which may occur in MAARC-type devices is simple viscous entrainment produced by viscous mixing of the propellant with the ambient tank gas. If this were to occur in an environment in which there were no material boundaries, then, as is well known, the thrust across any plane normal to the axis would remain invariant with axial portion. However, if walls are placed a finite distance from the exhaust, as is the case in the MAARC vacuum tank, a cell is formed in the region surrounding the exhaust and momentum is convected "upstream" near the walls and added to the jet when the cell closes near the exit plane of the MAARC. In addition to this back flow near the walls, things are further complicated by viscous shear forces exerted on the cell by the tank walls. To obtain a reasonably accurate measure of the thrust from ρu^2 measurements in a flow dominated by viscous entrainment, it would be necessary to obtain an estimate of the wall shear forces and to make a measurement of ρu^2 from the centerline to the tank wall. The measurement of the negative ρu^2 associated with the back flow near the wall would be extremely difficult as the large radii imply extremely small values of ρu^2. Measurements of thrust obtained from ρu^2 measurements which did not include the back flow and viscous wall forces would be dominated by the cell structure and hence any conclusions based on these measurements would be inconclusive. The thrust obtained from these incomplete measurements may not be closely related to the actual thrust produced by the device. It should be noted at this point that thrust stand measurements should not be affected by viscous entrainment if the thrust stand is sufficiently well shielded from the cellular flow in the vacuum tank. Several observations have been made which may aid in determining the extent and type of entrainment present in the MAARC.

Operation of the MAARC with No Net Propellant Through-put

It has been shown by R. John at Avco/RAD[18] that propellant is ingested into his device from the ambient gas of the vacuum tank and then ejected in a narrow region near the centerline.

We have been unable to operate the MAARC in the above manner. We have found that when the propellant flow through the engine is turned off, the engine immediately extinguishes itself (in less than a second) even when the ambient tank pressure is maintained or increased either by introducing propellant through a port in the vacuum tank or by closing the valve to the vacuum pumps. Our normal ambient tank pressure at .05 gms/sec hydrogen is 350μ.

The most likely explanation for this difference from the experience of other investigators is the method used in mounting the MAARC in the

vacuum system. The exit of the MAARC is mounted flush with the end wall of the vacuum tank, whereas other devices are placed completely within the vacuum chamber. This may have a significant effect on the modes of circulating ambient gas which are possible. The differences in anode geometry may also influence this effect.

ρu Measurements of Entrainment in Hydrogen

A measure of the amount of ambient gas entrained in the exhaust can be found from the ρu data presented above.

The amount of entrained gas is determined by computing the difference between the mass flow computed from the ρu distribution corresponding to R_o and the actual mass flow through-put remained essentially constant over the range of mass flows and magnetic fields studied. This effect is shown in Fig. 39. From this figure, it can be seen that the entrained flow represents .15 ± 20% gms/sec which is 3 to 15 times the actual through-put. In addition, at .05 and .03 gms/sec through-put, the amount of entrained gas was observed to increase slightly with increasing B, whereas at .02 and .01 gms/sec the converse was true.

Note, however, that because of the nature of the ρu^2 profiles, the thrust corresponding to R_{II} represents 1/2 to 1/4 the thrust obtained by integrating the complete profile and hence is not linearly reduced by the entrained flow.

Shroud Measurements

To investigate entrainment in the MAARC, we have placed a translucent fused quartz cylinder at its exit plane. This cylinder is 6 inches long by $6\frac{1}{4}$ ID, and has a $\frac{1}{4}$ inch thick wall. No attempt has been made to optimize the size or shape of this shroud. As a first step toward reducing entrainment, it was primarily intended to determine its structural capabilities and to observe its effect on the overall current-voltage characteristics of the MAARC.

Figure 40 shows a photograph of this shroud during operation of the MAARC at a 60 kw power level in hydrogen. Figure 14 is a schematic drawing which shows its placement in the tank relative to the MAARC and the $\dot{B}$ probe. This shroud has also been used in ammonia at a 25 kw power level and under no conditions has there been any observable change in either the current-voltage characteristics of the MAARC with and without the shroud or any change in the physical characteristics of the shroud itself except for a slight discoloration of its inside surface. This latter observation is compatible with computed values of radiative heat transfer from the shroud which show that it could radiate at least 50 kw without softening.

The MAARC has been operated in .05 grams/sec hydrogen at 60 kw with and without the shroud. Sample oscillograms obtained under these conditions are shown in Fig. 41. This data was obtained near the exit plane of the shroud.

Noted on these oscillograms are the three radial positions defined previously. In addition the line marked "shroud" indicates the radial position corresponding to the inside surface of the shroud. The apparent discrepancy in the ρu profiles with the shroud, obtained with the Autovac and the ion gauge, is due to the difference in relative sensitivity of these two instruments; the Autovac being more sensitive at the higher ρu's, while the ion gauge is more sensitive at the low values of ρu. This is confirmed by the excellent agreement between R_I and R_{II}. The steady rise in ρu outside the shroud is due to the decreasing ambient gas temperature and relatively constant gas pressure as one moves away from the shroud. This effect produces an increasing $n\bar{c}/4$ as discussed previously. Based on this data, the following observations can be made.

1. Presence of the shroud reduces the thrust by almost 40%.

2. Presence of the shroud reduces the amount of entrained ambient gas from 0.15 grams/sec to 0.08 grams/sec or by an amount of about 45%.

3. Very good agreement exists between the computed values of R_I and R_{II} and the radial boundary of the shroud indicating that there is negligible diffusion of ambient gas particles into the shroud nor is there appreciable ablation of shroud material.

To further determine the type of entrainment which dominates the flow in the MAARC, it is necessary to establish the current distribution in its meridian plane. In this way we hope to understand the degree to which $\bar{j} \times \bar{B}$ entrainment is possible and also to evaluate the possible disturbing effects of the shroud itself.

The axial current distribution computed from the data of Fig. 15 is shown in Fig.42, for hydrogen with the shroud in place. This distribution was obtained at the same axial position as the ρu and ρu^2 profiles shown in the last section. As can be seen from this figure, the total axial current at this position is 12 amps or 5% of the total arc current. Under no conditions were axial currents measured near the exit of the shroud in excess of 5% of the total arc current.

From this data we can conclude that the major portion of the arc currents flow well inside the shroud. Hence, the shroud prevents the arc currents from flowing into the ambient tank gas.

Ammonia Data

The MAARC has been operated in ammonia at a power level of approximately 25 kw and mass flows of .03, .02 and .01 grams/sec. A few oscillograms are presented in Fig. 43 to demonstrate the basic nature of the ρu^2 profiles in ammonia with the quartz shroud. The first observation to be made

from this data is that there is no measurable thrust obtained once the thrust plate is placed at a radius outside the shroud. If there is no diffusion of ambient gas particles into the shroud as was seen in hydrogen, then these results suggest that there is no measurable momentum in the circulating tank gas. This indicates quite strongly that there is negligible viscous entrainment of ambient ammonia by the MAARC exhaust under these operating conditions in ammonia. In addition, the essential agreement between thrust stand and ρu^2 probe results in ammonia, as discussed above, further suggest the lack of viscous entrainment. This is not surprising since the ambient number density is substantially smaller than it is in hydrogen because of ammonia's higher molecular weight. In addition to this, it is clear from Fig. 43 that there are marked changes in the shape of the ρu^2 profiles with variations in magnetic field as has been previously observed by us. Before this effect can be clearly understood, it is necessary to determine the shear forces on the shroud, the total mass flow leaving the shroud from ρu measurements, and also to maintain a smaller variation in input power level.

Some measurements of axial current have also been made in ammonia and at the present time they indicate that with or without the shroud, the axial current is substantially less than 5% of the total arc current to within a distance of 2 inches from the exit plane of the MAARC nozzle.

Conclusions on Entrainment

We may summarize the observations made above as follows:

1. B_θ measurements indicate that under all operating conditions, in both hydrogen and ammonia, the arc currents are well contained within the volume of the shroud.

2. ρu measurements in hydrogen at the exit of the shroud show that there is no measurable diffusion of ambient gas particles into the shroud.

3. The shroud reduces the measured thrust by 40% and the amount of entrained ambient gas by 45%.

4. ρu^2 measurements in ammonia indicate negligible viscous entrainment under the given operating conditions.

The first two observations above indicate conclusively that there is no possibility of j x B entrainment when the shroud is in place; hence, the entrainment in hydrogen with the shroud must be entirely viscous mixing. One would expect that the presence of the shroud should in fact reduce the viscous mixing of the exhaust with the ambient tank gas as is observed in Item 3. Also, lowering the ambient number density should again reduce viscous entrainment if, at the same time, the jet diameter does not increase substantially. This is compatible with observation 4 above. To evaluate the role of $\bar{j} \times \bar{B}$ entrainment in the absence of the shroud, it is necessary to establish the meridian plane current distribution with and without the shroud. If these currents flow over a very small volume then one may

conclude that viscous entrainment also dominates in the absence of the shroud. Under these conditions, the smallest possible shroud can be constructed which does not disturb the current pattern and ρu and ρu^2 measurements made at the exit plane of this shroud. If these measurements are made near enough to the shroud, it will be a straightforward task to divide the ρu^2 profile into that portion which results from the exhausting jet and the contribution to the profile of the cell which is driven by the flow downstream from the measuring position. Measurements of viscous drag on the shroud itself must also be made under these conditions.

Discussion of High Exhaust Velocity vs Low Operating Voltage Results of Other Experiments

Some investigators in this field are questioning the possibility of obtaining an average directed energy per particle in the exhaust which corresponds to a voltage drop that a single charged ion must attain which is greater than the applied voltage. There are two possible ways that the ions can achieve this velocity in a plasma accelerator with no net space charge.

First, in many cases the total current delivered to the accelerator exceeds by several factors the ion current in the exhaust; that is, the number of electrons passing between the cathode and anode per unit time is much greater than the number of ions leaving the accelerator per unit time. In this case, it is possible for these electrons to transfer part or nearly all of their energy to the ions through Coulomb collisions, and since there are many more electrons passing through the accelerator and falling through the applied potential region than ions per unit time, it is possible for the ions to achieve energies much higher than the individual electron energies. The limiting speed for the plasma exhaust is then set when the $\bar{U} \times \bar{B}$ potential integrated over the width of the accelerator in the exhaust equals the applied voltage, i.e., $\bar{E}$ applied $\gtrsim \bar{U} \times \bar{B}$. This is the design criteria for most linear $\bar{j} \times \bar{B}$ accelerators that operate with continuum flow, i.e., short collisional mean free paths, and most probably limits all high density plasma accelerator exhaust velocities. This flow picture is not new,[19] and has been most recently described in connection with some experiments using cesium as a propellant in a magnetic annular arc by R. John et al.[20]

The second mechanism that is important is also due to collisional transfer of momentum between the electrons and ions, but with electron velocities not in the direction perpendicular to the applied field. While the mechanism described above is due to $\bar{j} \times \bar{B}$ forces, there can also be a drag force on the ions due to high velocity streams of electrons parallel to the applied field. In particular, it is possible to have a high electron current density concentrated near the axis due to currents emanating from the cathode in a device such as the MAARC or MPD arcs. In order to assess the importance of this drag effect, one must investigate the ion momentum equation.

$$\rho_I \bar{U}_I \nabla \bar{U}_I = -\text{grad } p_I + \sum_{I,j=1}^{3} \nu_{Ij}(\bar{U}_j - \bar{U}_I) + N_I \epsilon (\bar{E} + \bar{U}_I \times \bar{B}) \qquad (29)$$

where

$\nu_{Ij} = N_I N_j Q_{Ij} M_I \bar{C}_I$

N_I = ion number density

$\bar{E}$ = electric field

$\bar{B}$ = magnetic field

ϵ = ion charge

ρ_I = ion density

Q_{Ij} = collision cross section between ions and j species

$\bar{C}_I$ = mean thermal velocity of ions

For the experiments considered in this discussion, the summation is made over the two species, namely neutrals and electrons. The same momentum equations for the electrons show the $\bar{j} \times \bar{B}$ forces in the last term. This gives rise to ion momentum in the second term on the right hand side of Eq. (29) which is the momentum transfer due to collisions from the other species of the plasma. If one considers the region downstream from the cathode near the axis in an MPD arc, the magnetic field is axial and the current is essentially parallel to the B field in this region. The acceleration of the ions due to electron drag can be estimated by examining Eq. (29) and writing

$$\rho_I U_I \nabla U_I \approx \nu_{Ie}(U_e - U_I) \quad , \tag{30}$$

where the other momentum terms have been neglected in order to assess the importance of the drag of the electrons on the ions. The change in ion velocity ΔU_I due to this effect in a typical acceleration can be estimated by integrating this force over a length similar to the nozzle length, L. Then Eq. (30) becomes

$$\int_0^L \rho_I U_I \frac{\partial U_I}{\partial x} dx = \rho_I \Delta U_I^2 = \nu_{Ie}(U_e - U_I)L \quad . \tag{31}$$

Also, the local current density J can be written

$$J = -N_e \epsilon (U_e - U_I) \quad . \tag{32}$$

Equations (31) and (32) can be used to obtain

$$\Delta U_I^2 = \frac{Q_{Ie} \bar{C}_I J L}{\epsilon} \tag{33}$$

where $\rho_I = N_I m_I$ has been used to eliminate the ion density. A total current of several hundred amperes is not uncommon for many of the experiments recently described in the literature. A typical nozzle length is at least 5 cm and an average electron energy equal to 1 eV is not inconsistent with many laboratory conditions. With these choices of parameters, and with an average ion thermal speed corresponding to 1000 sec, i.e., 10^4 m/sec, we obtain $\Delta U_I^2 \simeq 10^9$ or $\Delta U_I \simeq 3 \times 10^4$ m/sec or a velocity increase equal to an impulse of 3000 sec, when the current density is 100 amperes/cm^2. This is an acceleration felt by the ions by a large axial current density which flows directly downstream from the cathode. It can be seen that this is not a negligible effect in considering the overall possibilities for achieving plasma acceleration.

SECTION V

RECOMMENDATIONS AND CONCLUSIONS

A magnetic annular arc has been constructed which is capable of producing a steady axisymmetric discharge in such propellants as nitrogen, hydrogen, ammonia, helium and argon at power levels from 10 to 200 kw with no apparent erosion of anode or cathode material. Diagnostic techniques have been developed for such local measurements as ρu^2, ρu and axial current density. We have carefully studied the overall operating characteristics of the MAARC and have been led to the following conclusions:

1. Application of an external magnetic field modifies the current voltage characteristics in a manner which is compatible with the existence of Hall effects in the device.
2. A theory has been developed and substantiating experimental data obtained which indicates that the arc voltage is determined for any given geometry and magnetic field shape by the relation
$$V = V_o + U_c B \ell .$$
The quantity V_o appears to be related to the anode voltage drop so that it becomes apparent that for high thermal efficiency one wants the quantity $U_c B \ell$ to be large compared to V_o.
3. Thrust measurements with a ρu^2 plate indicate that both an optimum field strength and field shape exist for maximizing the thrust at a given power level.
4. Combined ρu and ρu^2 measurements indicate that marked viscous entrainment of ambient tank gas exists when the MAARC is operated in hydrogen with our test tank facility. Preliminary results in ammonia indicate that there is no such problem in this propellant in the range of operation of interest.

Shroud measurements in hydrogen indicate that the interference of entrained gas with the ρu^2 probe can be eliminated.

At the present time there appears to be two basic acceleration modes possible in MAARC type devices. The first is the development of very high plasma enthalpies with substantial Hall currents flowing in the nozzle to give body forces directed radially inwards to reduce anode losses. The device operates similarly to a conventional arc jet then with a production of high enthalpies and recovery as directed energy in the magnetic nozzle. This mode of operation necessarily ionizes the propellant substantially in order to obtain high gas enthalpies and corresponding high exhaust velocities. The acceleration does not depend upon the obtaining of high operating voltages except to minimize the electrode voltage drop losses. Propellants such as sodium and lithium suggest that if multiple ionization does not occur, the ionization losses will be negligible because of the low ionization energies for these types of propellants.

The second mode involves the attainment of high voltages, i.e., a large product $U_c B \ell$, which implies relatively high ionization and dissociation energy such as ammonia or hydrogen where the velocity a propellant particle must have so that its kinetic energy equals the dissociation and ionization energy is relatively high. The use of this type of propellant leads to high operating voltages which besides minimizing electrode voltage drop losses causes the arc current to flow in the extended portion of the nozzle where the bias field has a larger radial component.

The interaction of the azimuthal Hall currents with the radial component of the bias field can then produce a substantial force in the thrust direction. This acceleration can take place until the cross products of the plasma velocity with the radial component of the bias field equals the applied Hall potential, i.e.,

$$\bar{U}_x \times \bar{B} \leq E_r \omega\tau$$

where the azimuthal Hall field is $\omega\tau$ times as large as the radial electric field. The electric field in the azimuthal (Hall) direction is closed on itself, hence it cannot be measured, but Hall currents do flow in the azimuthal direction until the back voltage (due to plasma crossing radial field lines) is

equal to the generated Hall potential.

Hence in order to produce $\bar{j} \times \bar{B}$ acceleration to high velocity in the expanded portion of the nozzle, the radial electric field must be made as large as possible for a given magnetic field intensity. This can only be accomplished by using a propellant such as hydrogen or ammonia which produces a large operating voltage due to their relatively high ionization and dissociation energies, compared to their molecular weight.

High conversion or thermal efficiencies in ammonia have been achieved and it appears at present that the propellant is compatible with long electrode life. A detailed mapping of the current distribution is underway at the time of the writing of this report which will help the understanding of the acceleration mechanism.

Our preliminary results indicate that gas entrainment in the MAARC using our vacuum facility may not be important in ammonia and that useful knowledge can be gained with this propellant in our facility.

It appears at this time therefore that relatively high performance can be obtained with an easily handled and stored propellant (i.e., ammonia), and we suggest that NASA investigate the performance of MPD arc devices using this propellant with the high vacuum facility at their disposal.

SECTION VI

REFERENCES

1. R. M. Patrick and W. E. Powers, paper presented at the Third Symposium on Advanced Propulsion Concepts, Cincinnati, Ohio, October 2-4, 1962. Advanced Propulsion Concepts, Proceedings of the Symposium, N. Y.: Gordon and Breach, 1963, Vol. I, pp. 115-136.

2. G. S. Janes and J. A. Fay, paper presented at the Second Symposium on Advanced Propulsion Concepts, Boston, Mass., October 7-8, 1959. Advanced Propulsion Concepts, Proceedings of the Symposium, Washington, D. C.: U. S. Government Printing Office, 1960.

3. J. A. Fay, Avco-Everett Research Laboratory Research Report 81, December 1959.

4. W. Grossman, R. Hess and H. A. Hussan, paper presented at the Fourth Electric Propulsion Conference, AIAA, Philadelphia, Penna., August 31-September 2, 1964. AIAA Paper No. 64-700.

5. Avco Corporation, Research and Advanced Development Division, Arc Jet Technology Research and Development, First Quarterly Progress Report RAD-SR-64-239, October 1964.

6. G. L. Cann, paper presented at the Fourth Electric Propulsion Conference, AIAA, Philadelphia, Penna, August 31-September 2, 1964. AIAA Paper No. 64-670.

7. A. C. Ducati, G. M. Giannini, and E. Muehlberger, paper presented at the Fourth Electric Propulsion Conference, AIAA, Philadelphia, Penna., August 31-September 2, 1964. AIAA Paper No. 64-668.

8. Avco Corporation, Research and Advanced Development Division, Arc Jet Technology Re search and Development, Second Quarterly Progress Report RAD-SR-65-5, December 1964.

9. Bosnjakovic, et al., "Mollier-Enthalpy-Entropy Charts of High Temperature Plasmas," Symposium on Thermodynamics and Transport Properties of Gases, ASME, 1960. p. 465.

10. P. Clausing, Ann. Physik 12, 961 (1932).

11. R. Narasimha, J. Fluid Mech. 10, 371 (1961).

12. H. W. Liepmann, J. Fluid Mech. 10, 65 (1961).

13. W. E. Powers and R. M. Patrick, Phys. Fluids 5, 1196 (1962).

14. H. Alfven, Rev. Mod. Phys. 32, 710 (1960).

15. O. Anderson, et als., J. Appl. Phys. 30, 188 (1959).

16. R. M. Patrick and T. R. Brogan, J. Fluid Mech. 5, 289 (1959).

17. R. John, Avco Corporation, Research and Advanced Development Division, Private Communication.

18. E. L. Resler and W. R. Sears, J. Aero. Sci., April 1958.

19. S. Bennett et al., AIAA Second Annual Meeting, San Francisco, Calif., July 26-29, 1965. AIAA Paper No. 65-296.

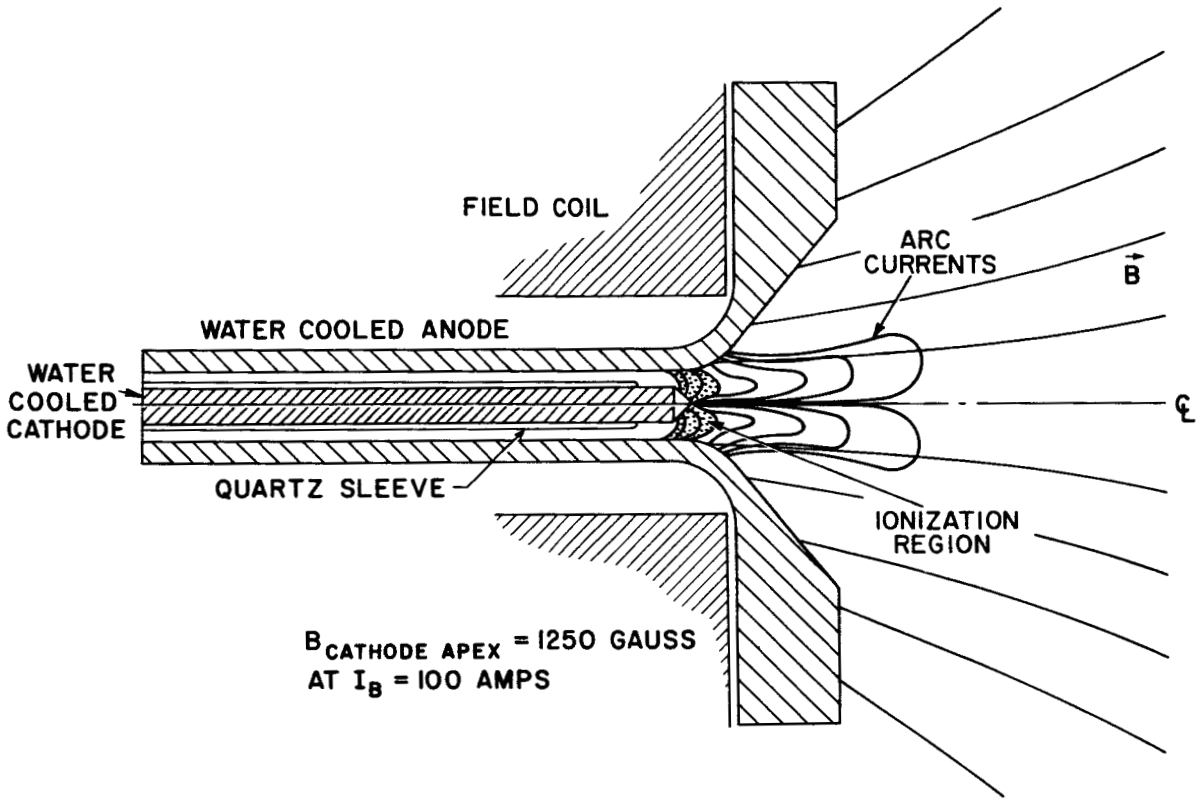

Fig. 1 A schematic cross section of the MAARC shown with the large heat sink coil. This drawing is nearly to scale. The arc currents are drawn in schematically. The ionization region is referred to in the text.

A2886X

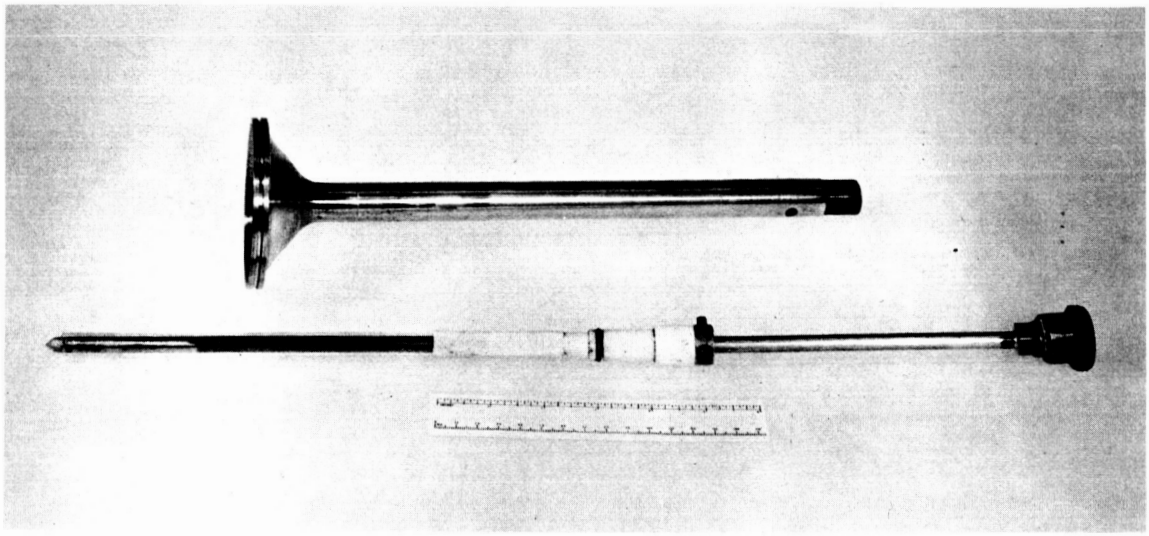

Fig. 2 Photograph of the anode and cathode assemblies used in the experiments described in this report.

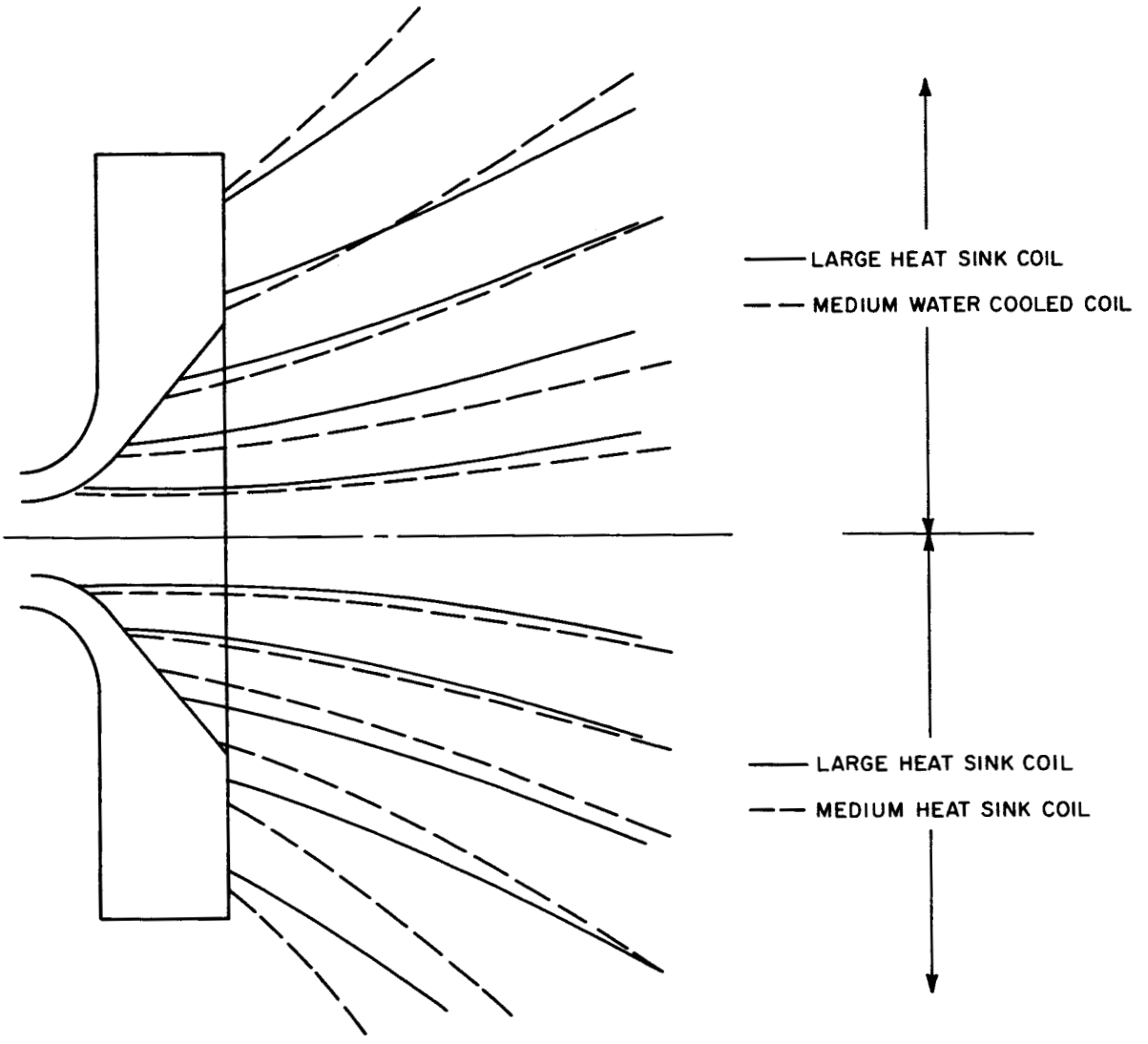

Fig. 3 Field plots of large heat sink, medium heat sink and medium water cooled coils. The upper half compares the large heat sink and medium water cooled coils; the lower half compares the large heat sink and medium heat sink coils.

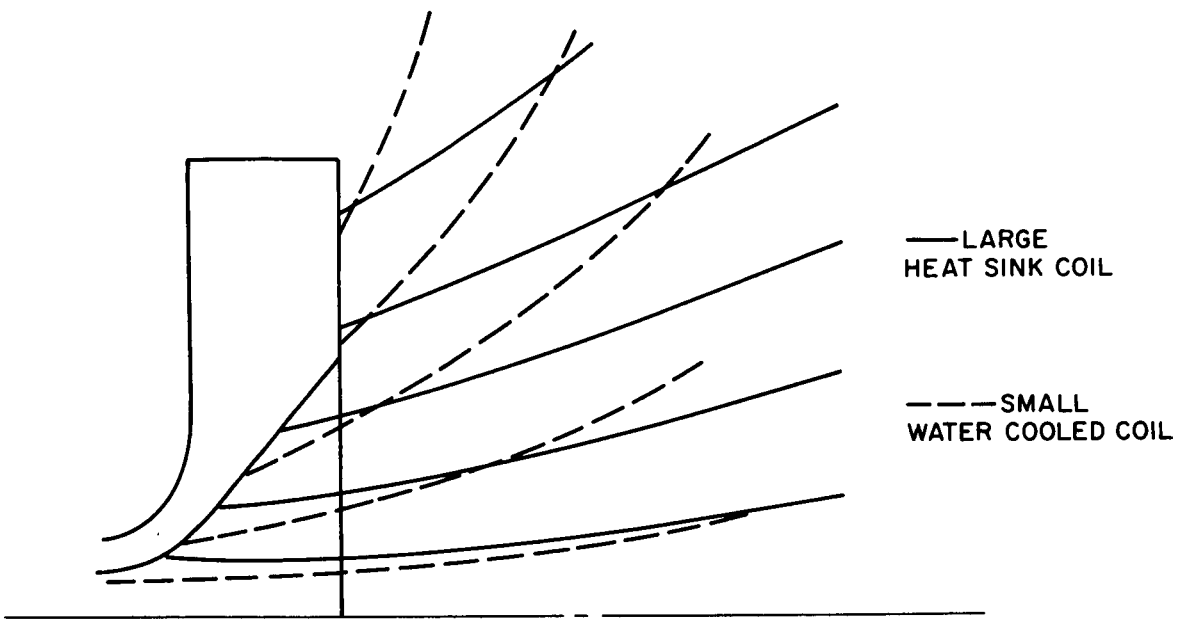

Fig. 4 Field plots comparing large heat sink and small water cooled coils.

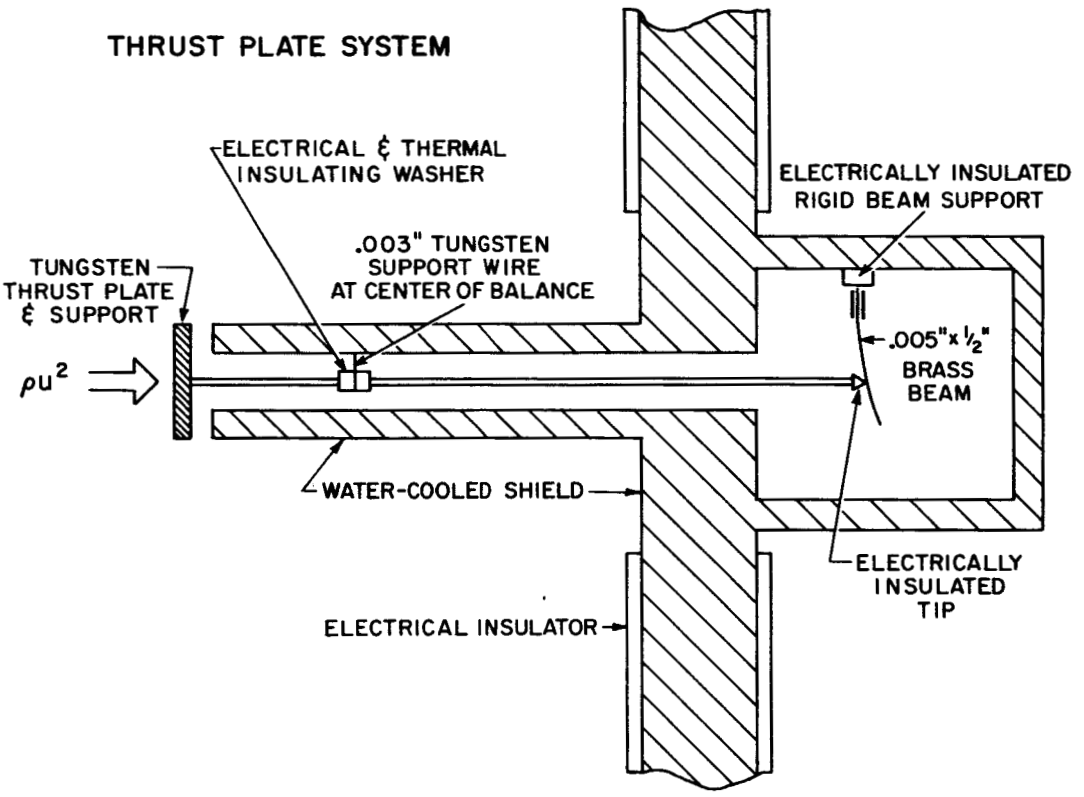

Fig. 5 Schematic drawing of the probe used to measure the thrust profiles in the MAARC experiments.

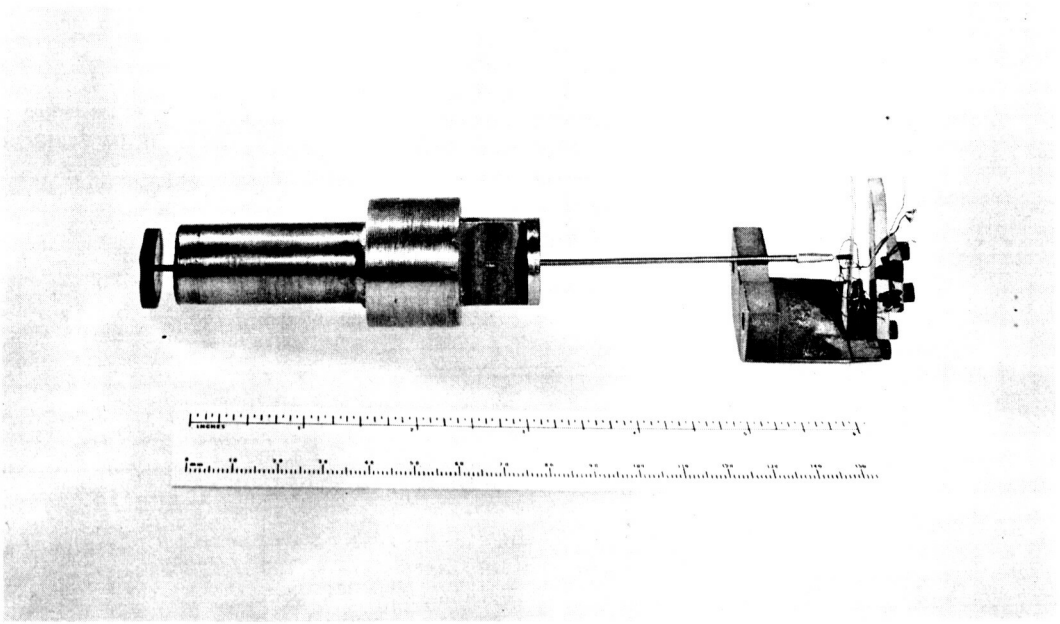

Fig. 6 Photograph of the essential components of the thrust plate system shown schematically in Fig. 5.

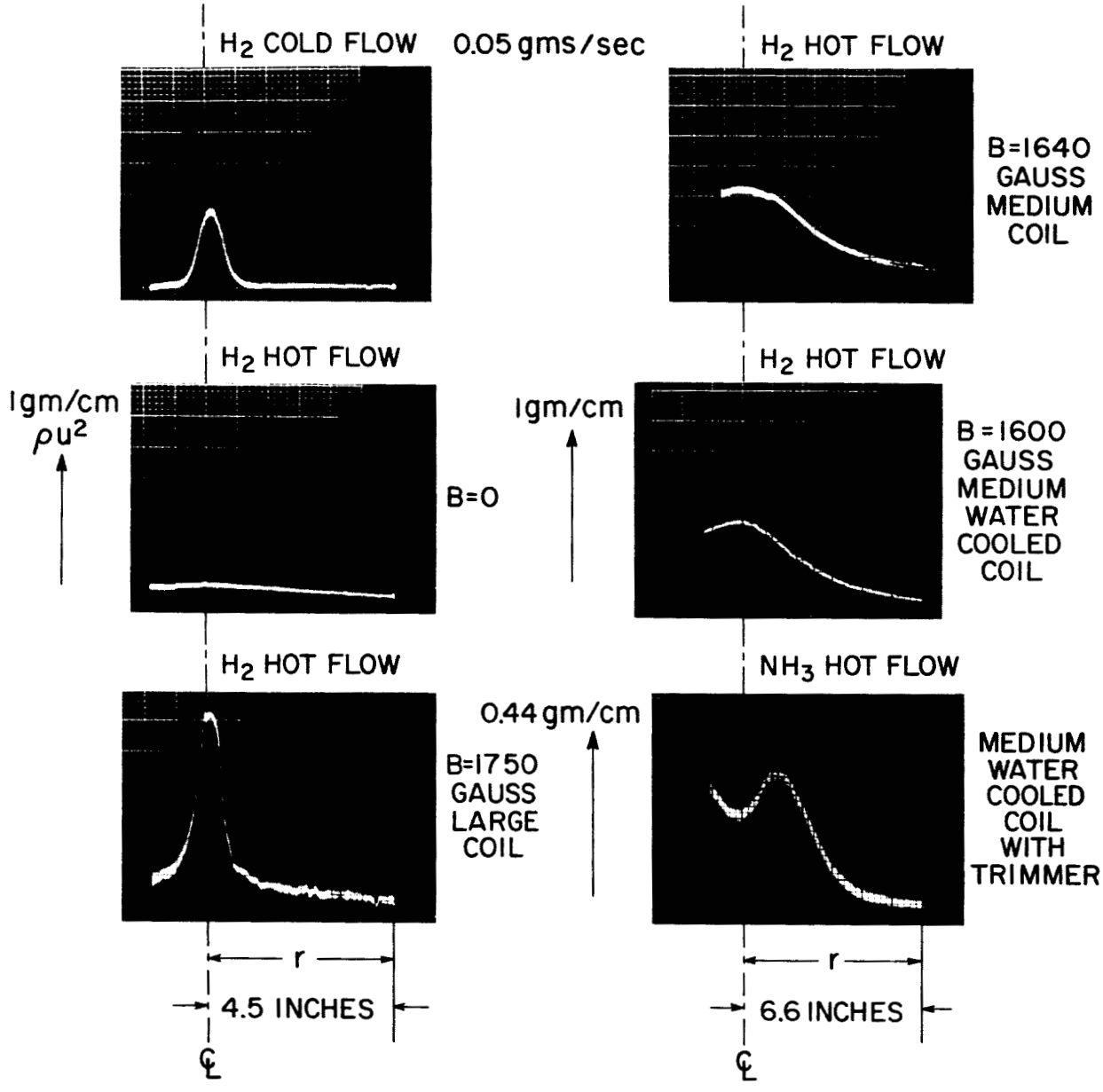

Fig. 7 Some typical ρu^2 profiles obtained with the thrust plate system. The hydrogen data shows both cold flow and hot flow with various bias magnetic fields. The ammonia data was obtained with the trimmer coil placed in series with the medium water cooled coil so that their respective fields opposed each other.

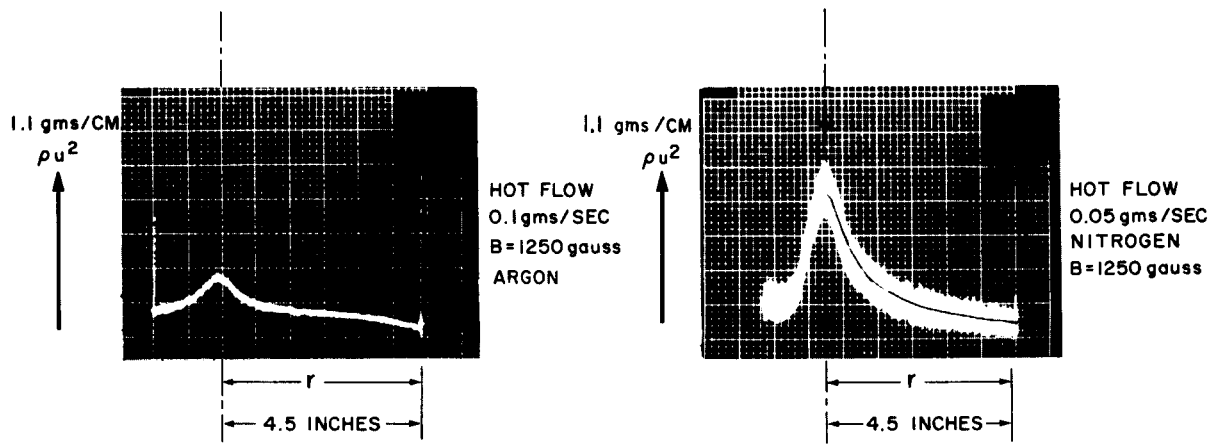

Fig. 8 Two oscillograms showing the thrust profiles obtained in argon and nitrogen.

A2895

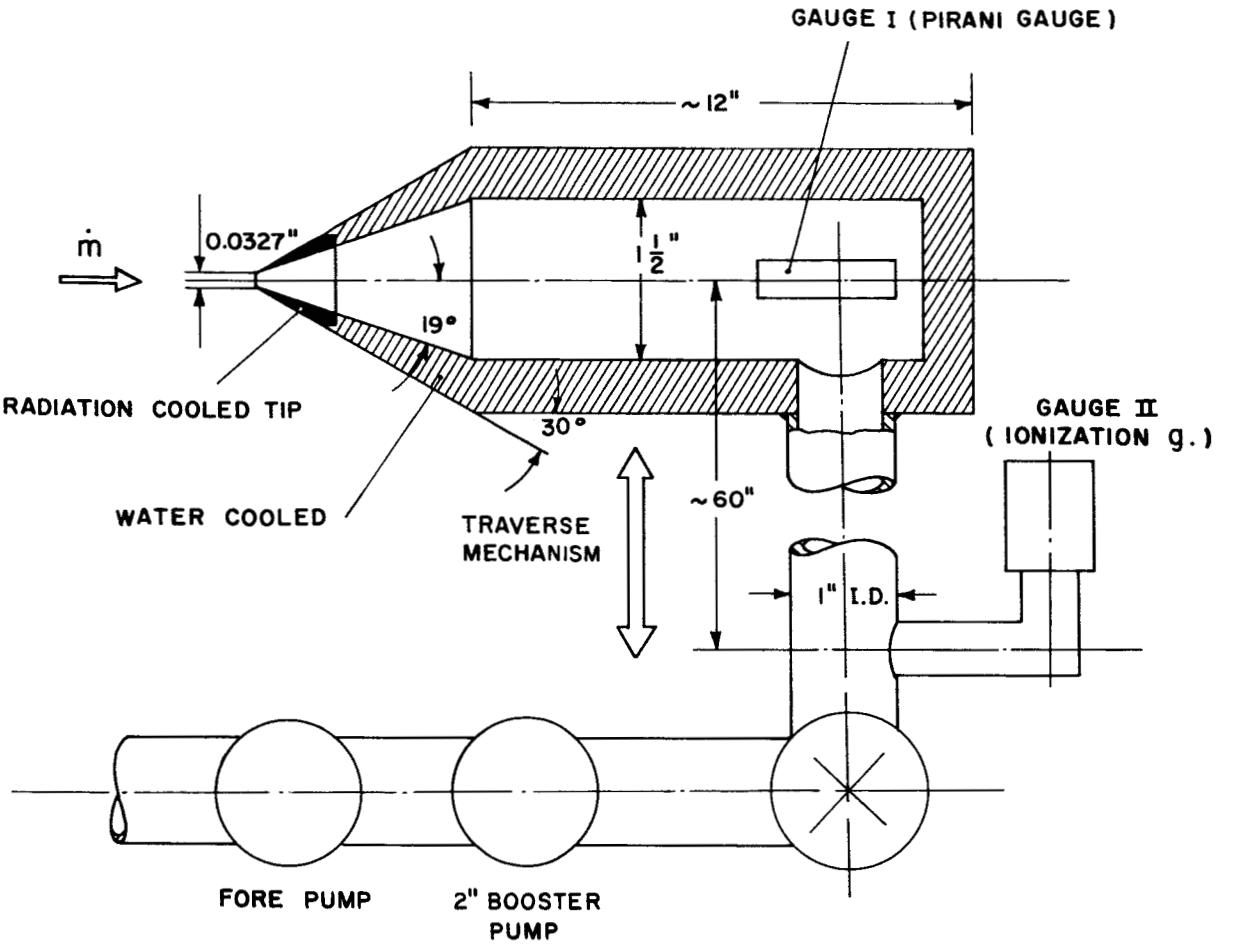

Fig. 9 Schematic diagram of the ρu probe used in the MAARC.

A4504

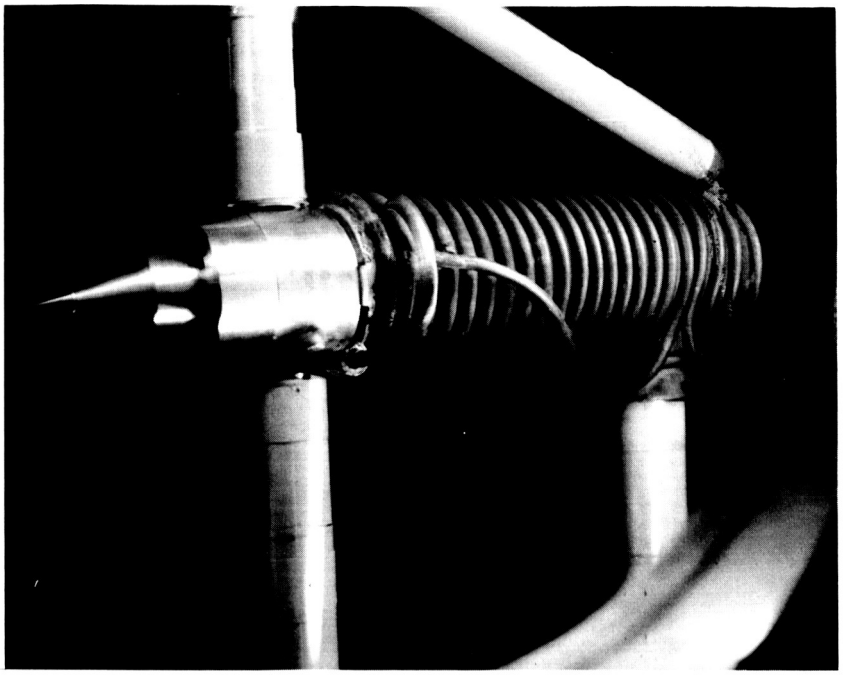

Fig. 10 Photograph of the ρu probe in place in the MAARC vacuum tank.

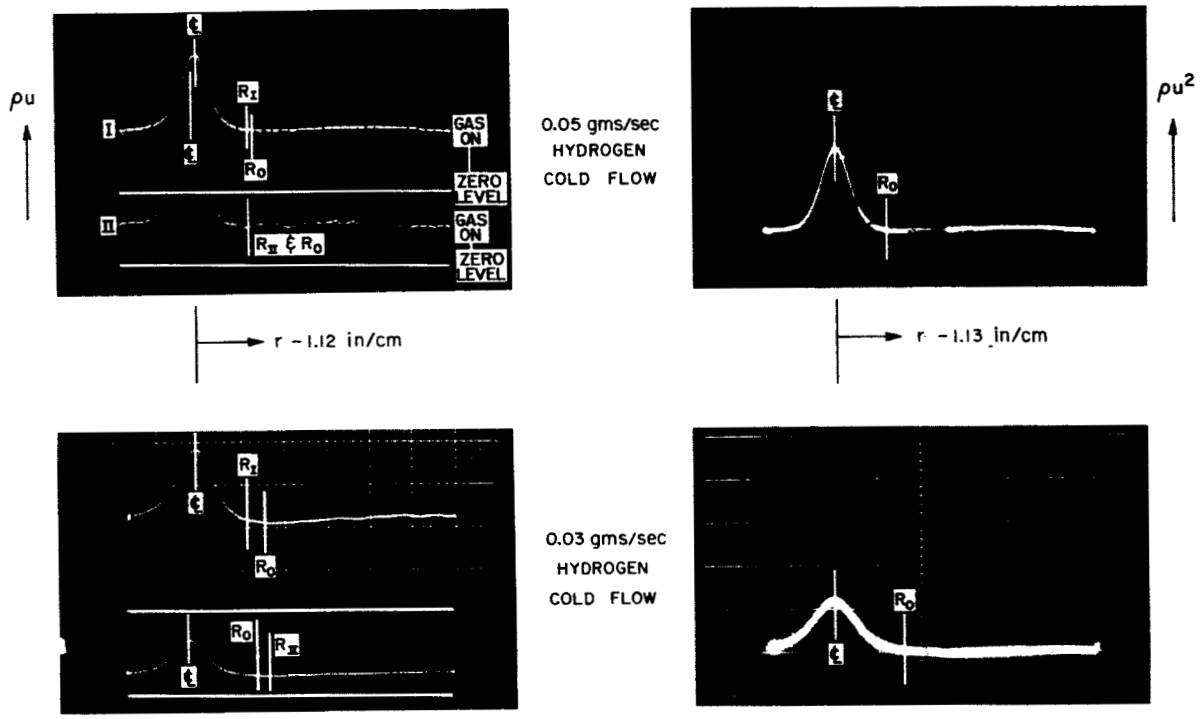

Fig. 11 Cold Flow ρu and ρu^2 Distributions in the MAARC

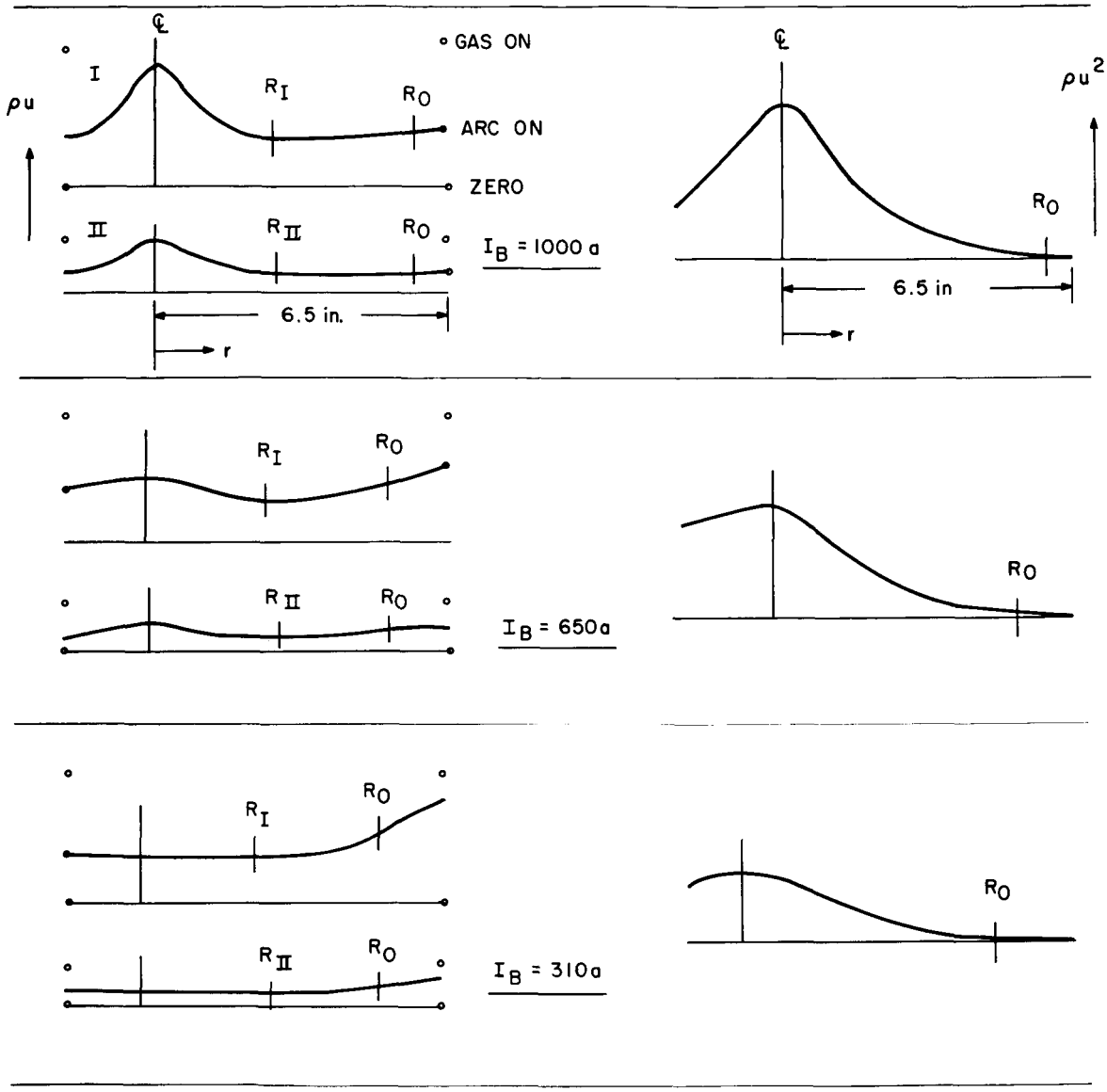

Fig. 12 Typical ρu and ρu^2 oscillograms obtained in the MAARC with .05 grams/sec Hydrogen at 50 to 60 kW and various magnetic field strengths with the trimmer coil adding.

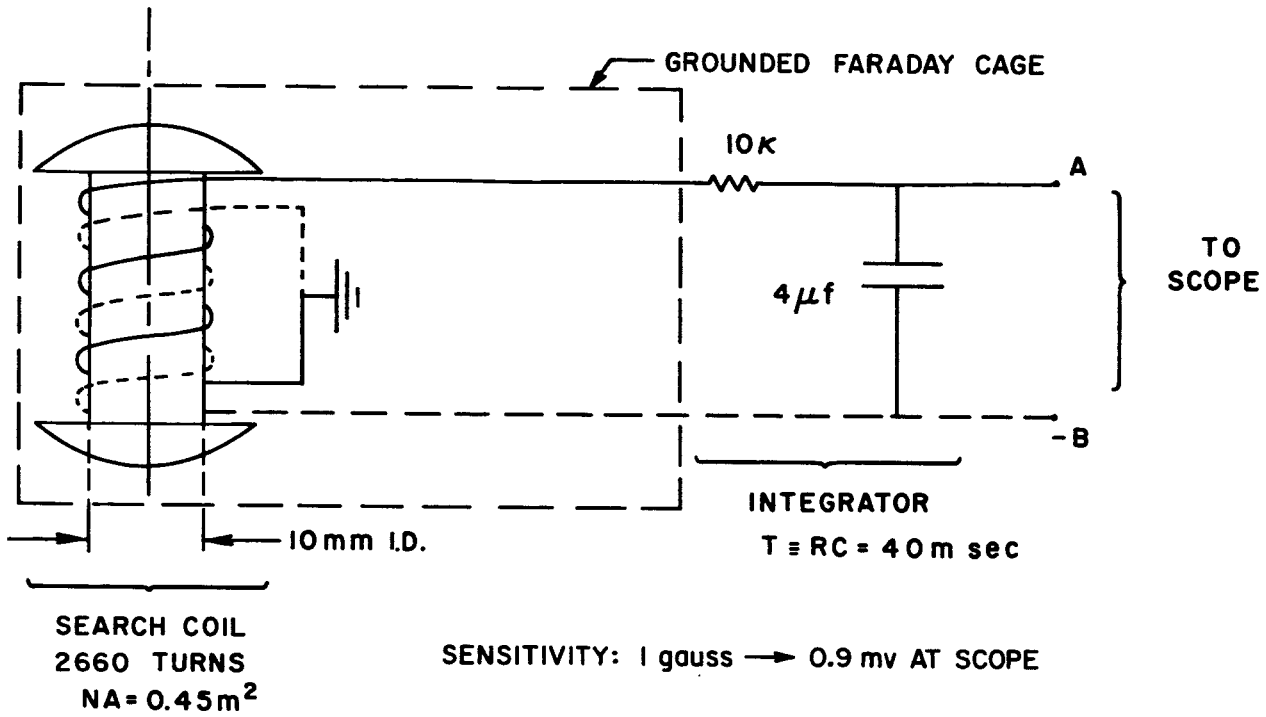

Fig. 13 Schematic diagram of the coil used in the measurement of axial current distribution.

A4262

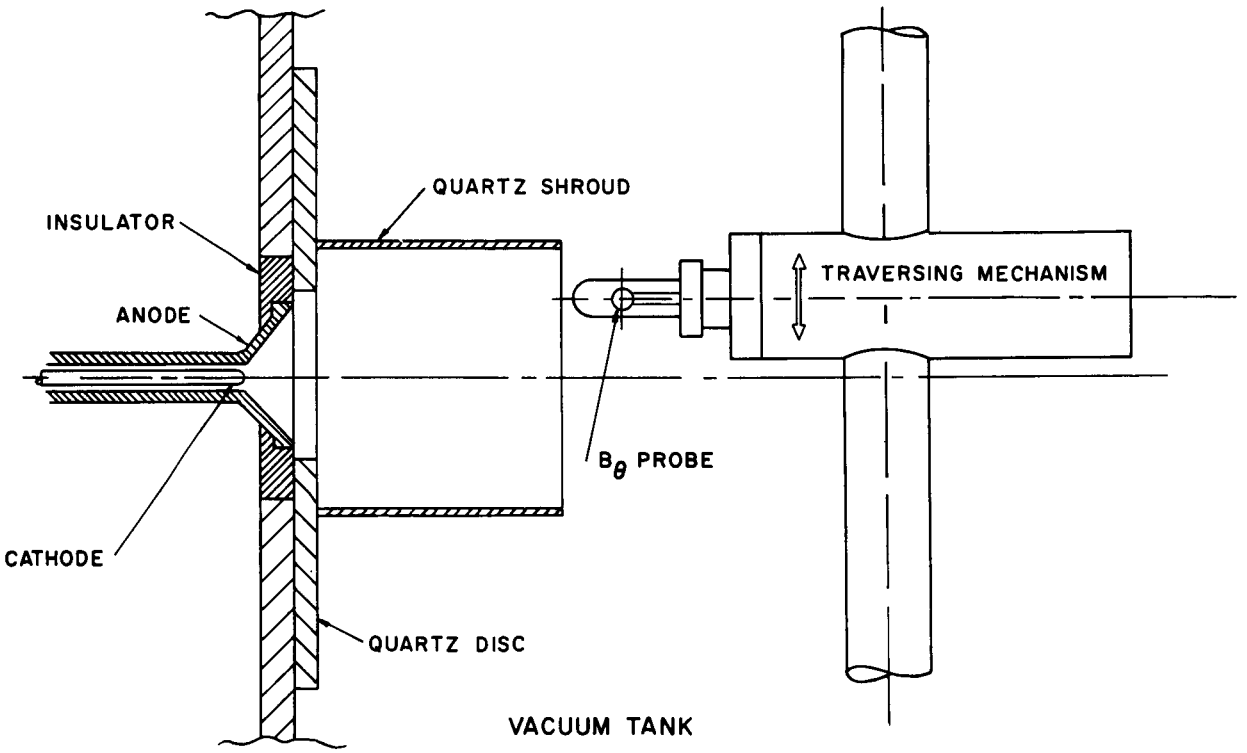

Fig. 14 Schematic drawing of the placement of the B_θ probe and the shroud in the MAARC facility.

A4263

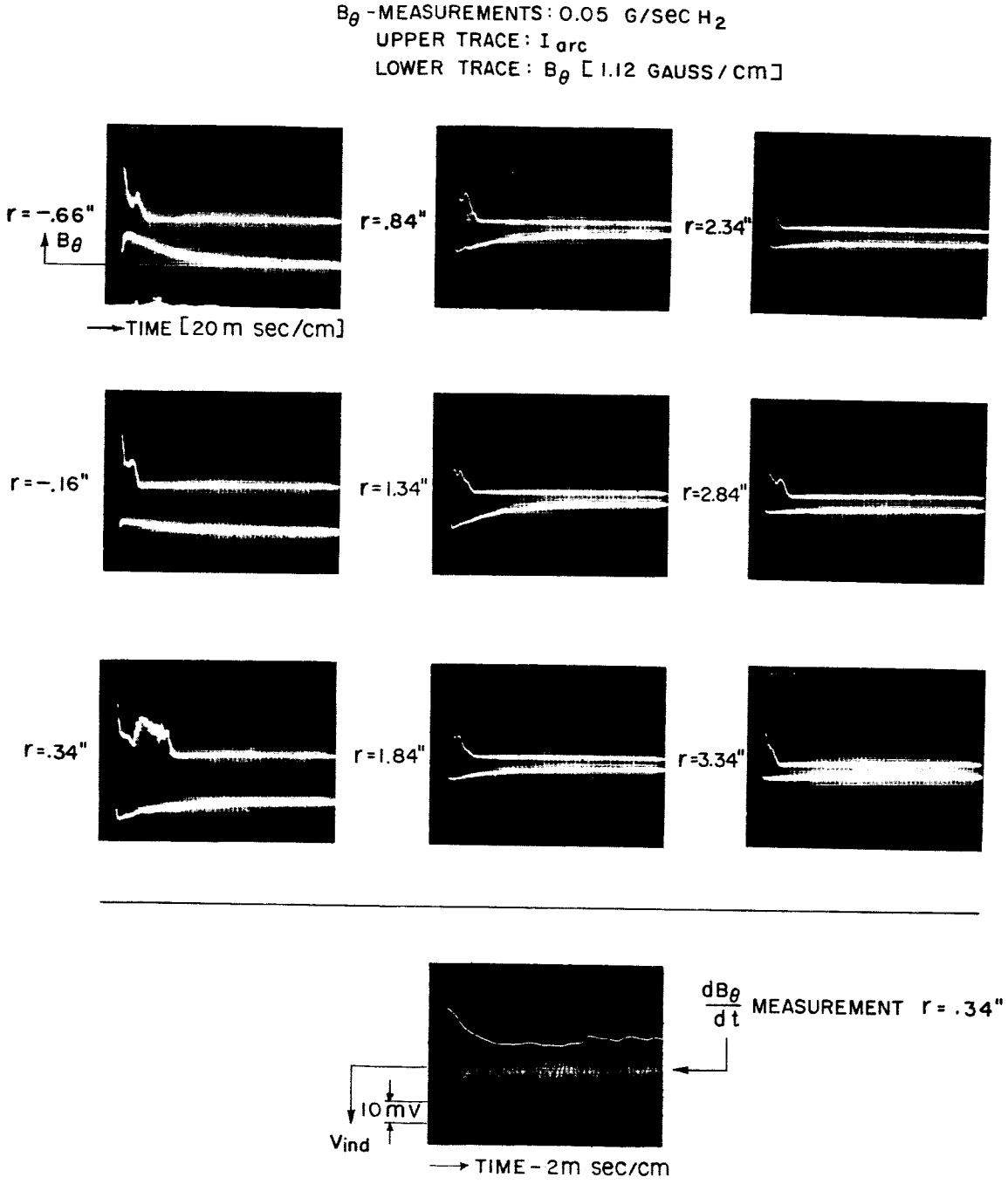

Fig. 15 B_θ measurements near the exit of the shroud. Also shown here is a direct measurement of dB_θ/dt.

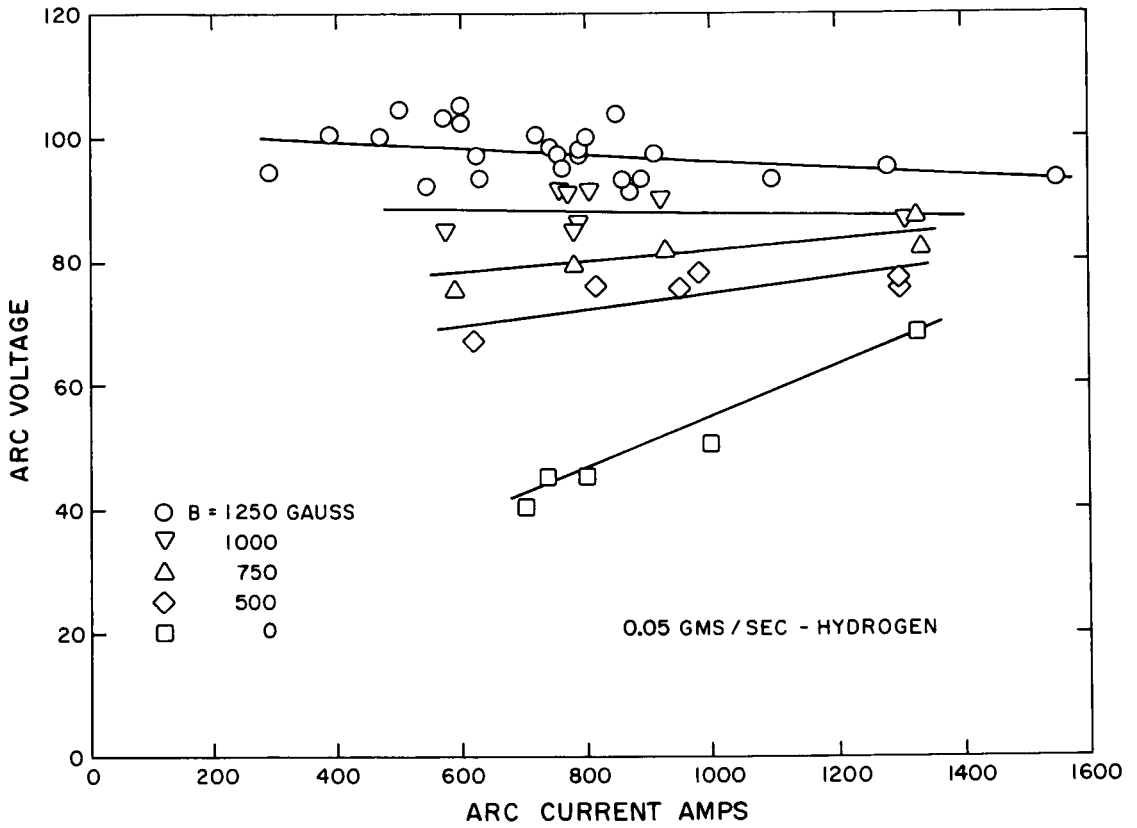

Fig. 16 MAARC voltage versus current characteristics. Note the change in the slope of current versus voltage curves with the change in bias field intensity. This data was obtained with the large heat sink coil.

A2893

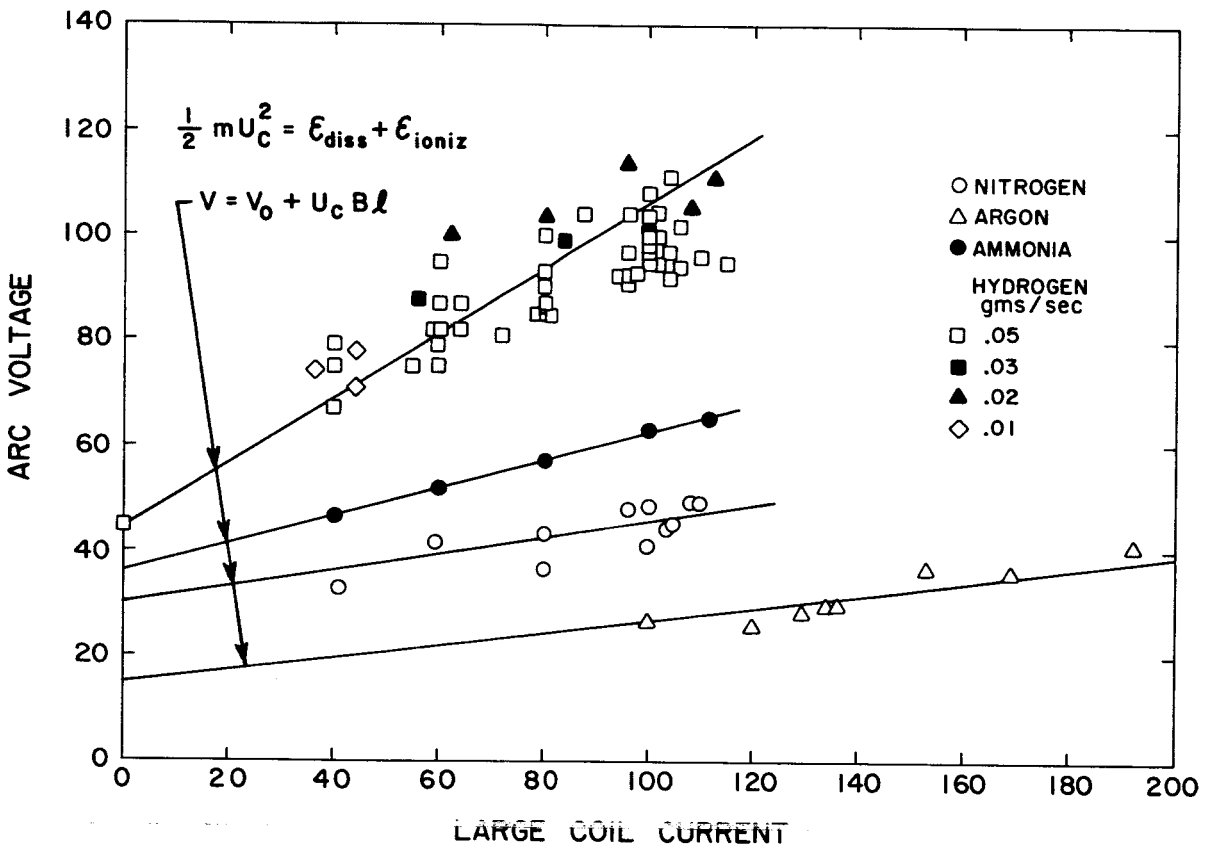

Fig. 17 The V-B characteristics of the MAARC operating with several propellants and various mass flows using the large heat sink coil.

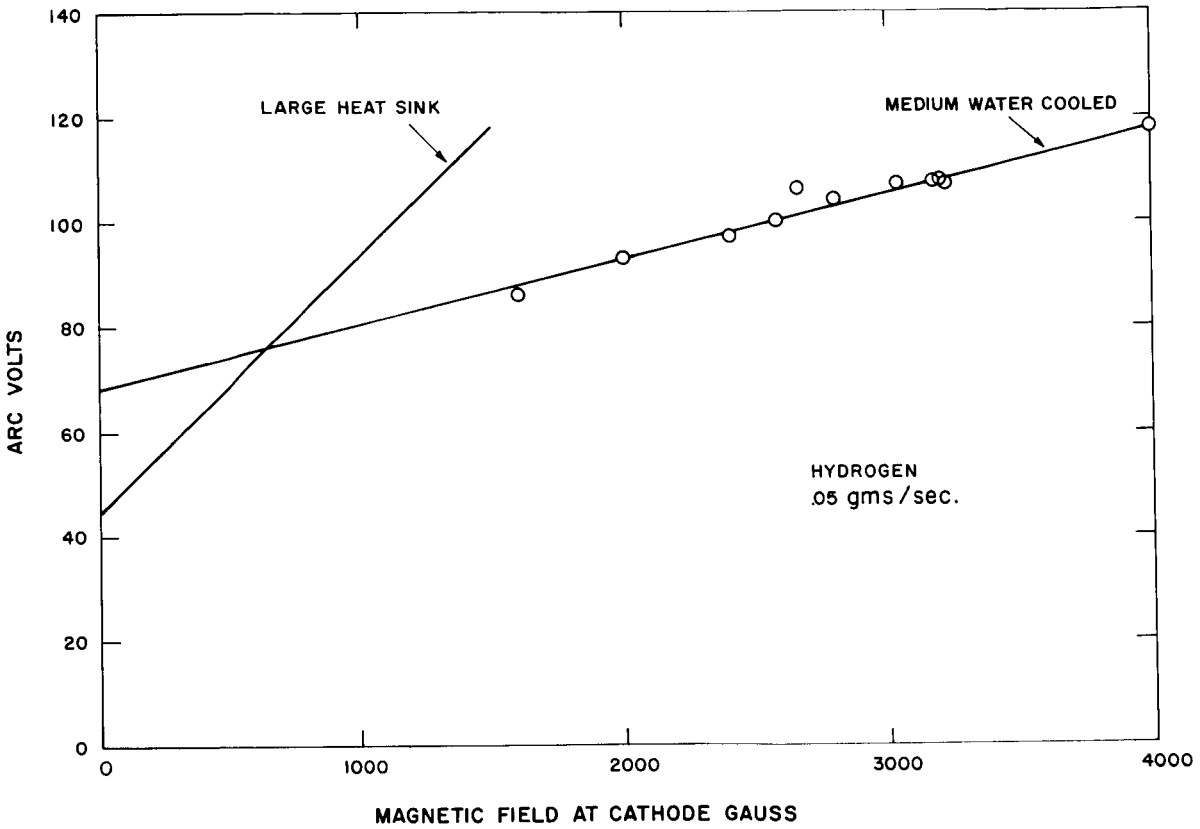

Fig. 18 V-B characteristics of the MAARC in hydrogen using the large heat sink and the medium water cooled coils. The large heat sink coil line was taken from Fig. 17.

A3269

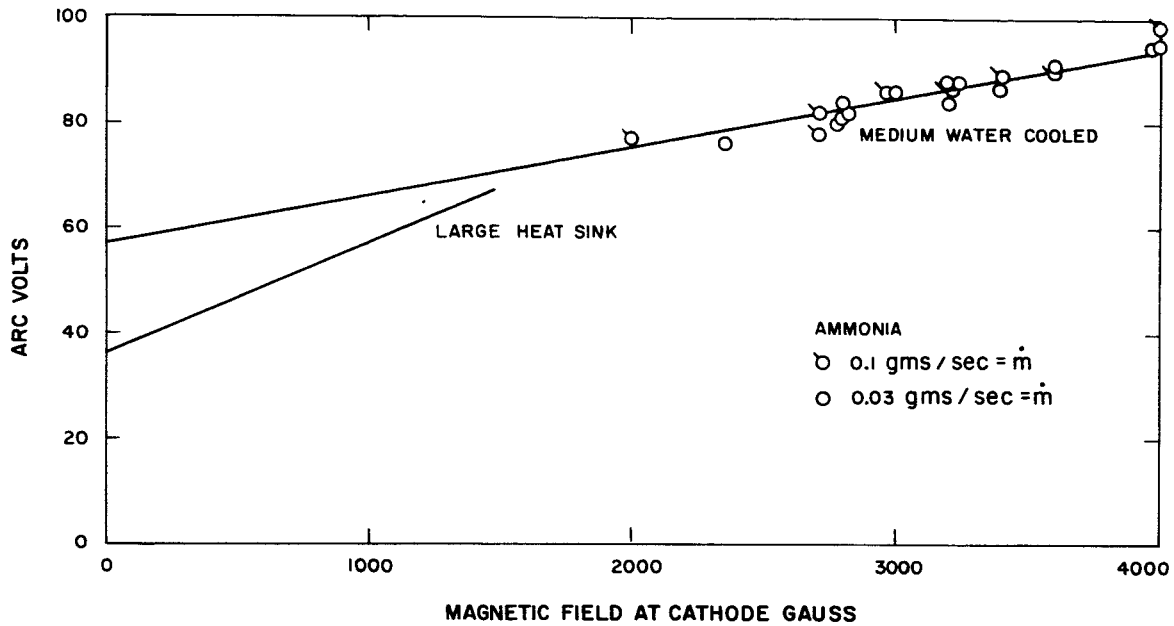

Fig. 19 V-B characteristics of the MAARC in ammonia using the large heat sink and the medium water cooled coils. The large heat sink coil line was taken from Fig. 17.

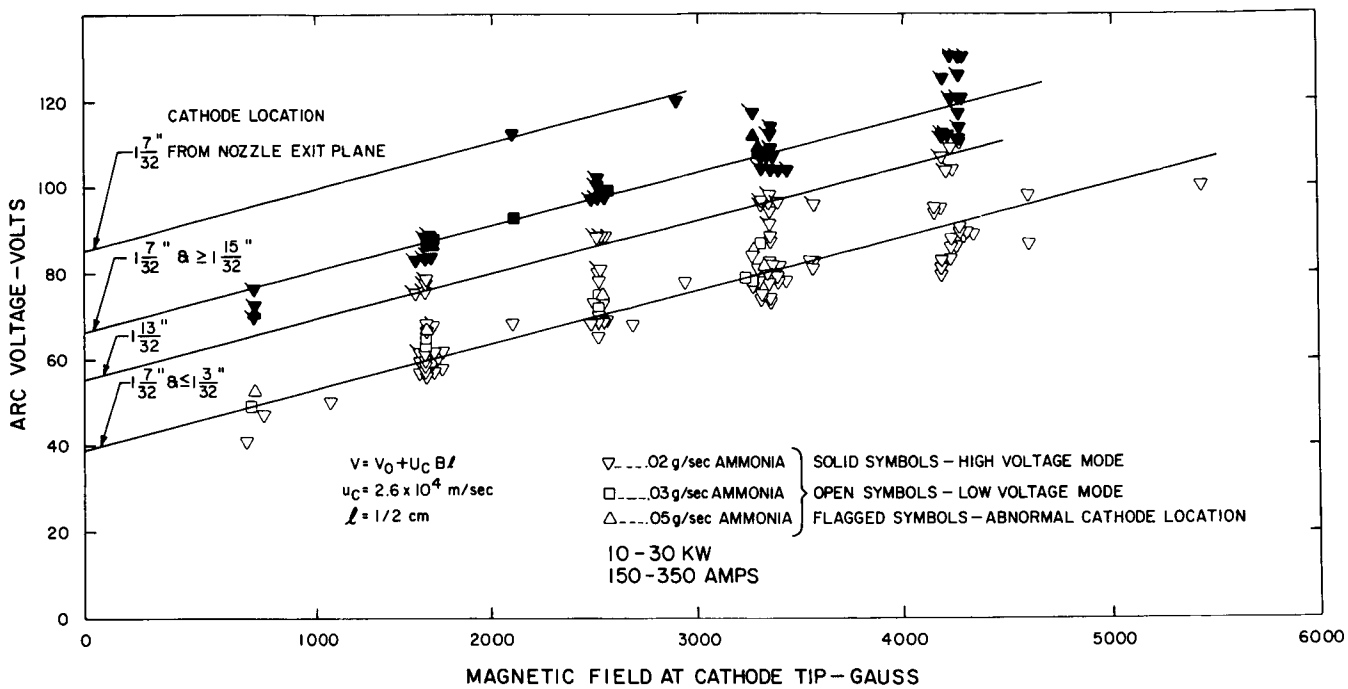

Fig. 20 Plot of arc voltage vs magnetic field strength in the MAARC showing the high and low voltage modes.

A4378

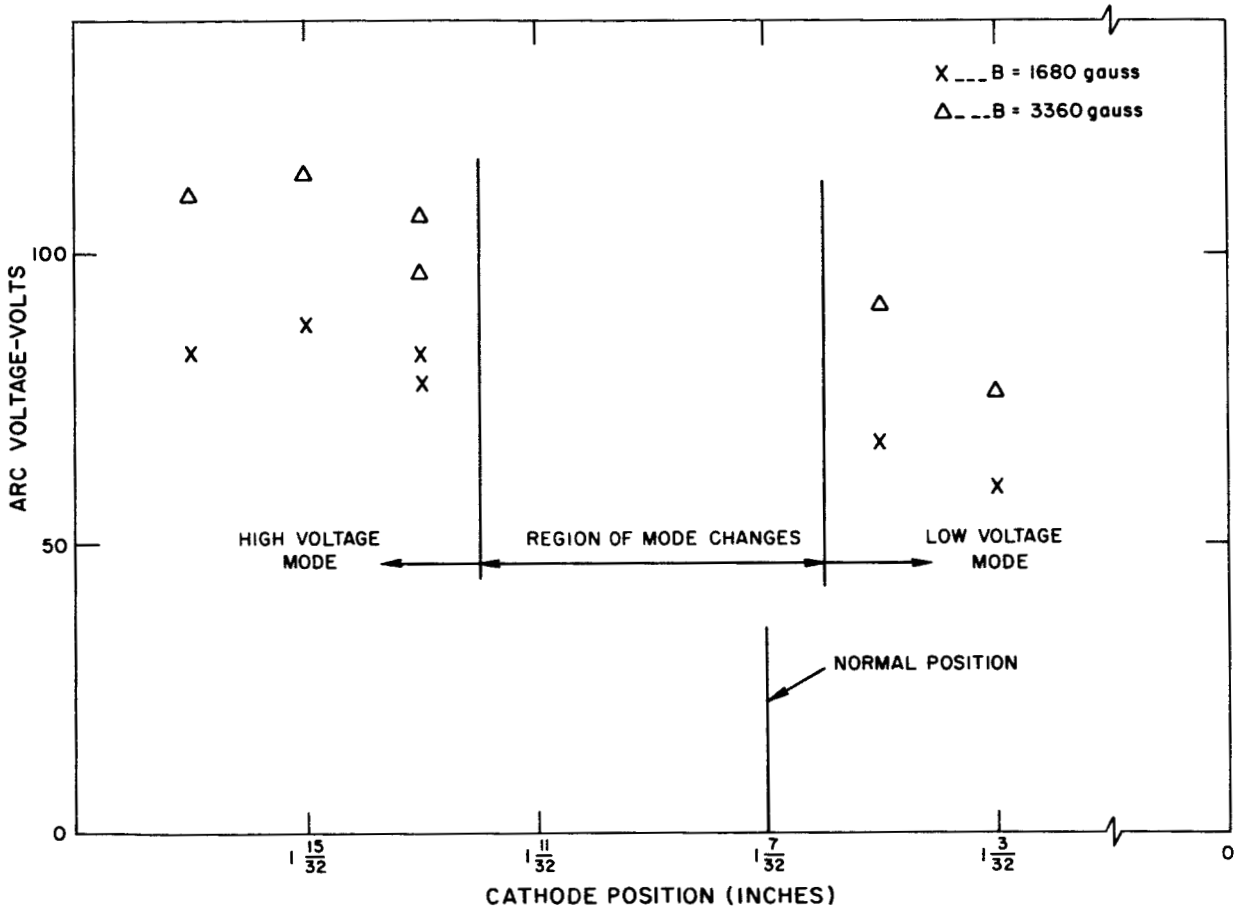

Fig. 21 Dependence of arc voltage on cathode location. The zero position corresponds to the nozzle exit plane.

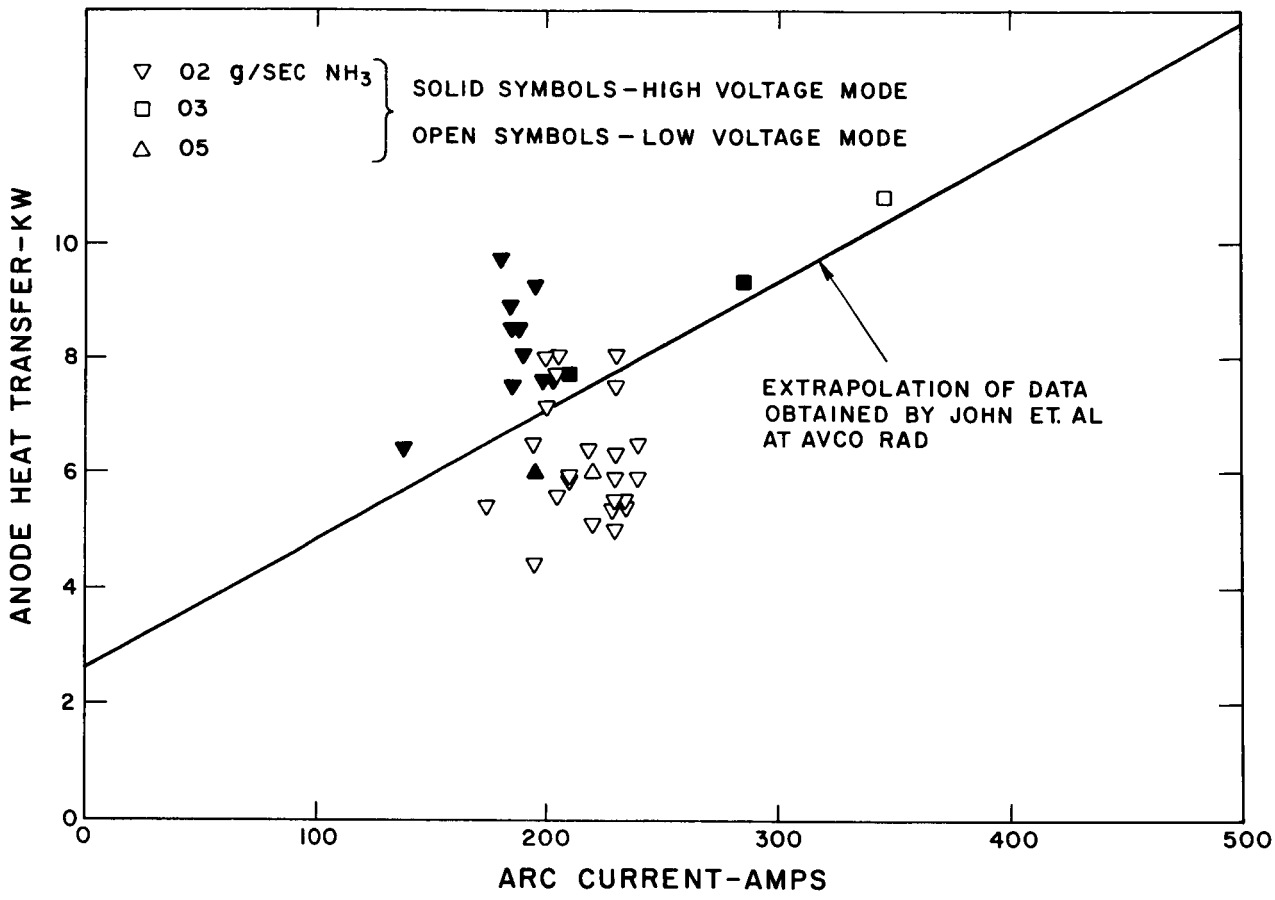

Fig. 22 Effect of voltage modes on the dependence of anode heat transfer on arc current.

A4380

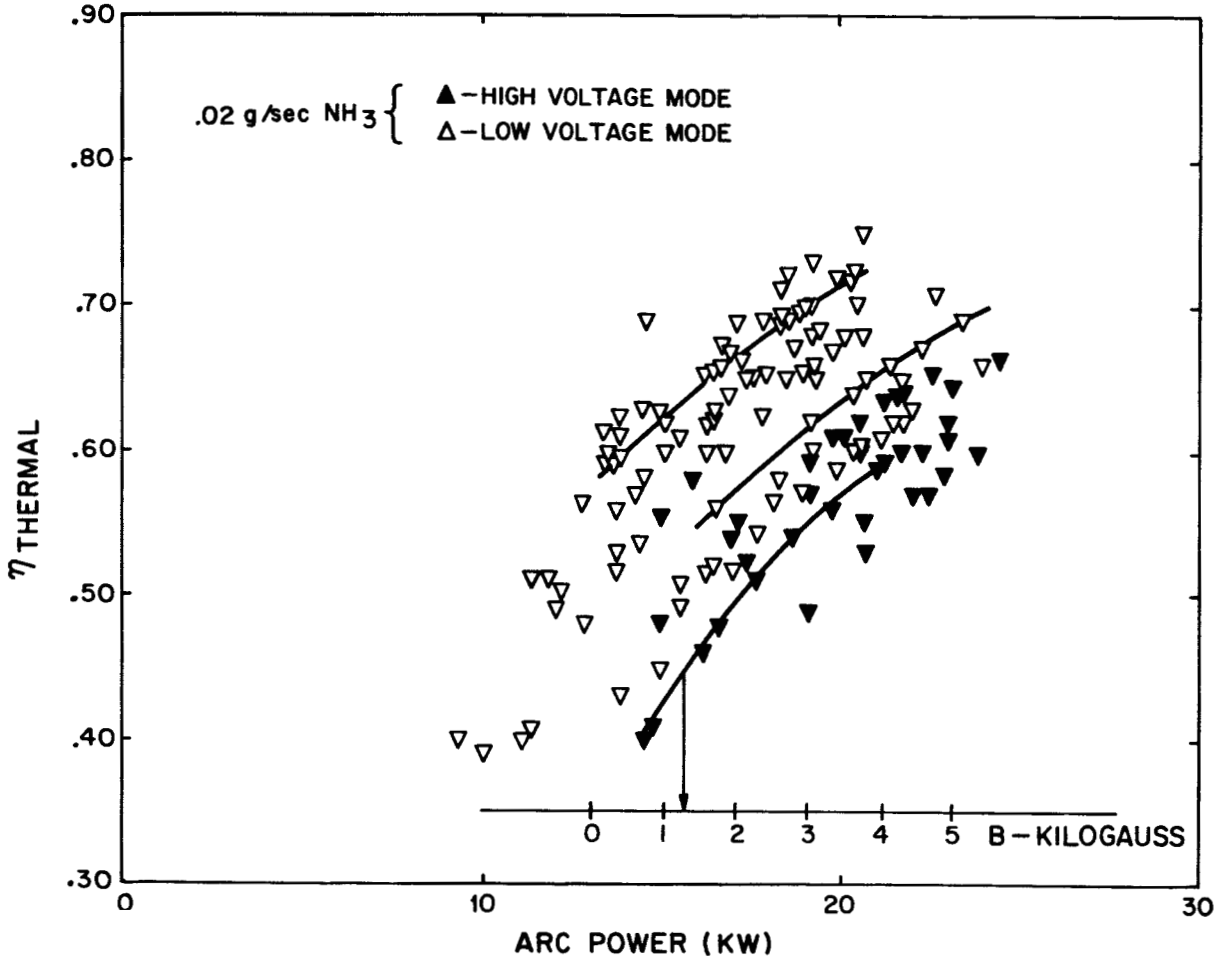

Fig. 23 Summary of thermal efficiencies vs input power showing the dependence on voltage modes.

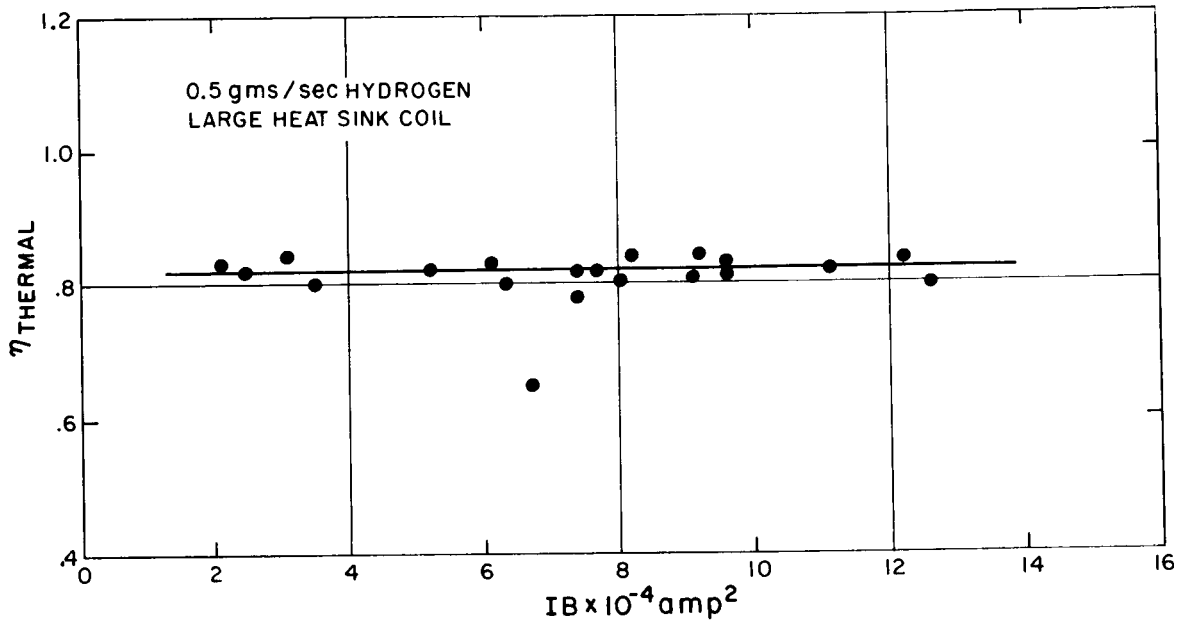

Fig. 24 The thermal efficiency $\eta_{thermal} = P_G/IV$ as a function of the IB product. This data corresponds to the points of Fig. 26.

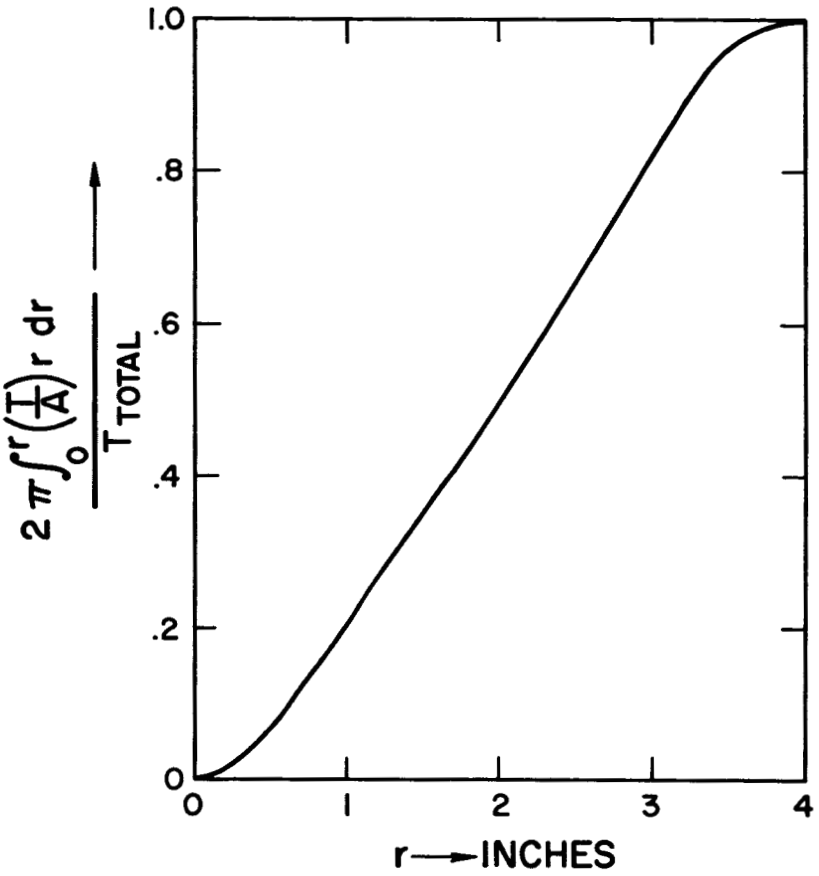

Fig. 25 Partial Thrust vs Radius

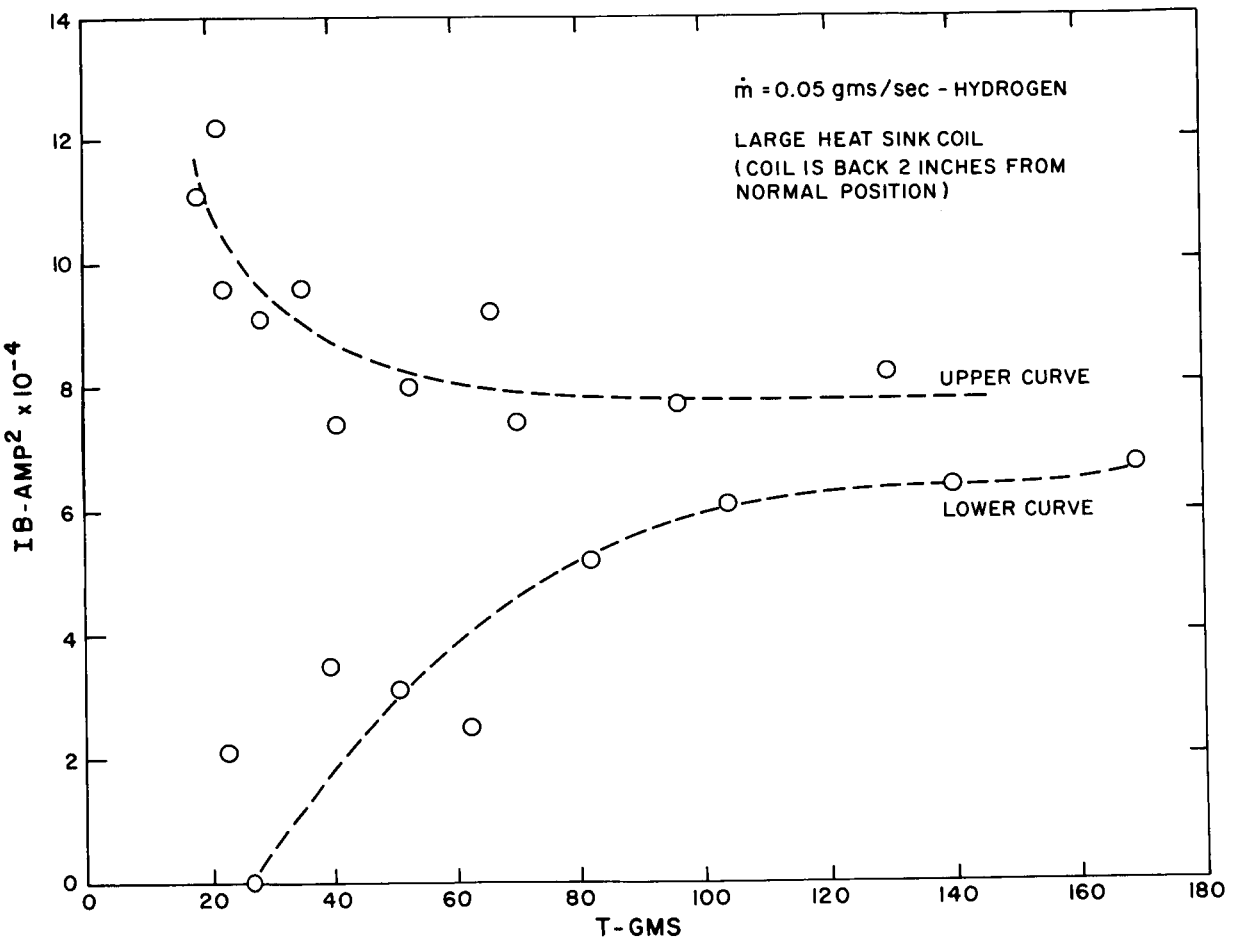

Fig. 26 IB vs thrust characteristics of the MAARC in hydrogen operating with a large heat sink coil at constant mass flow and essentially constant power levels.

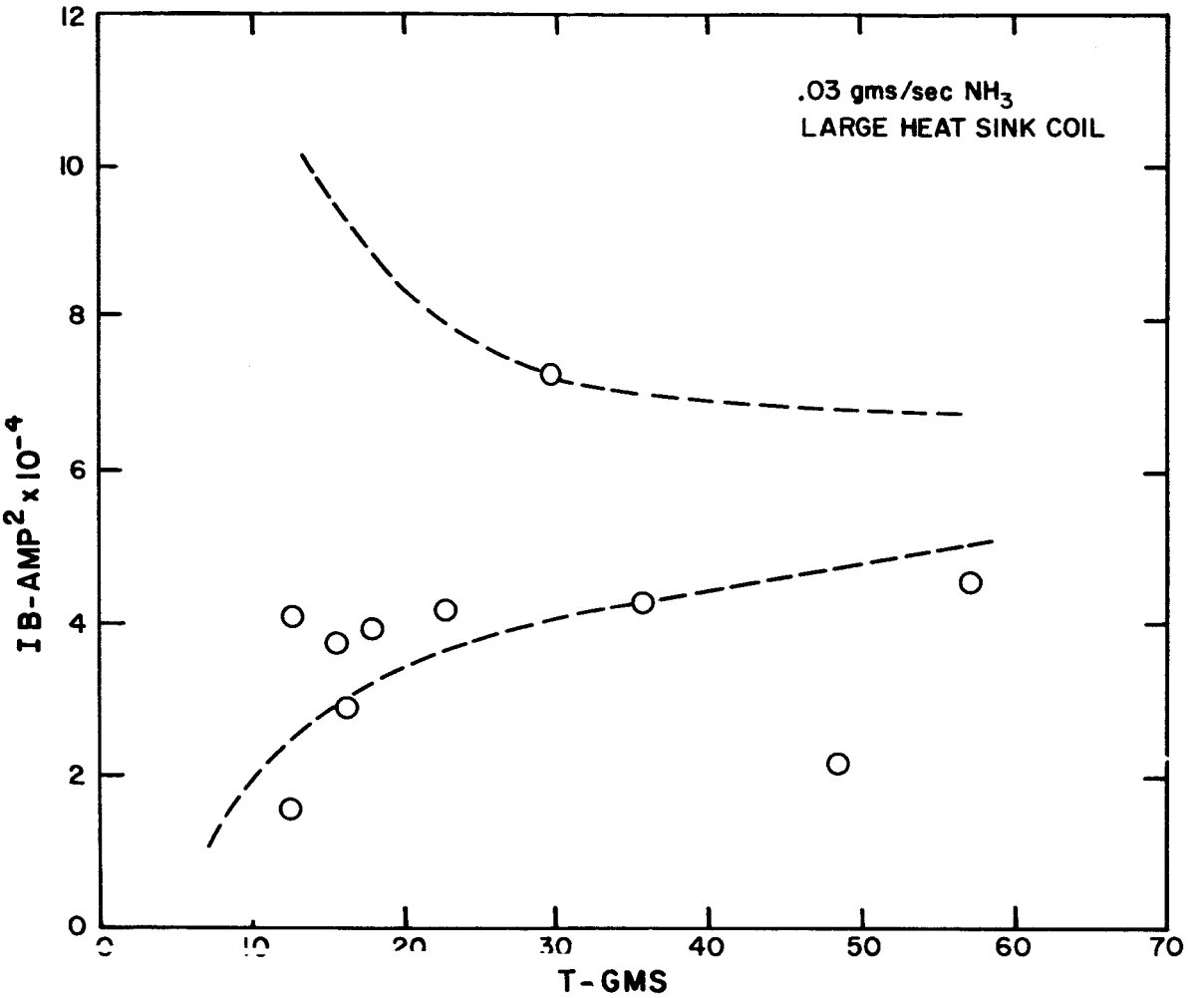

Fig. 27 IB vs thrust characteristics of the MAARC in ammonia operating with a large heat sink coil at constant mass flow and essentially constant power levels.

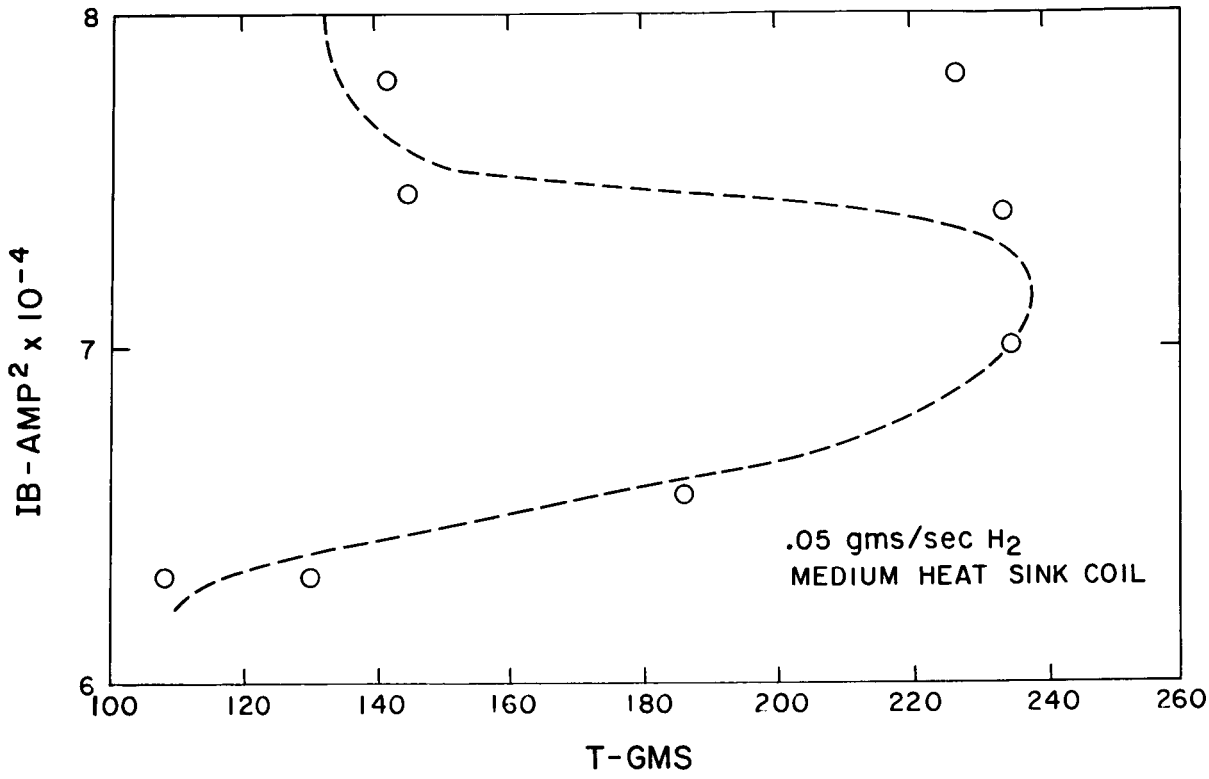

Fig. 28 IB vs thrust characteristics of the MAARC in hydrogen operating with a medium heat sink coil at constant mass flow and essentially constant power levels.

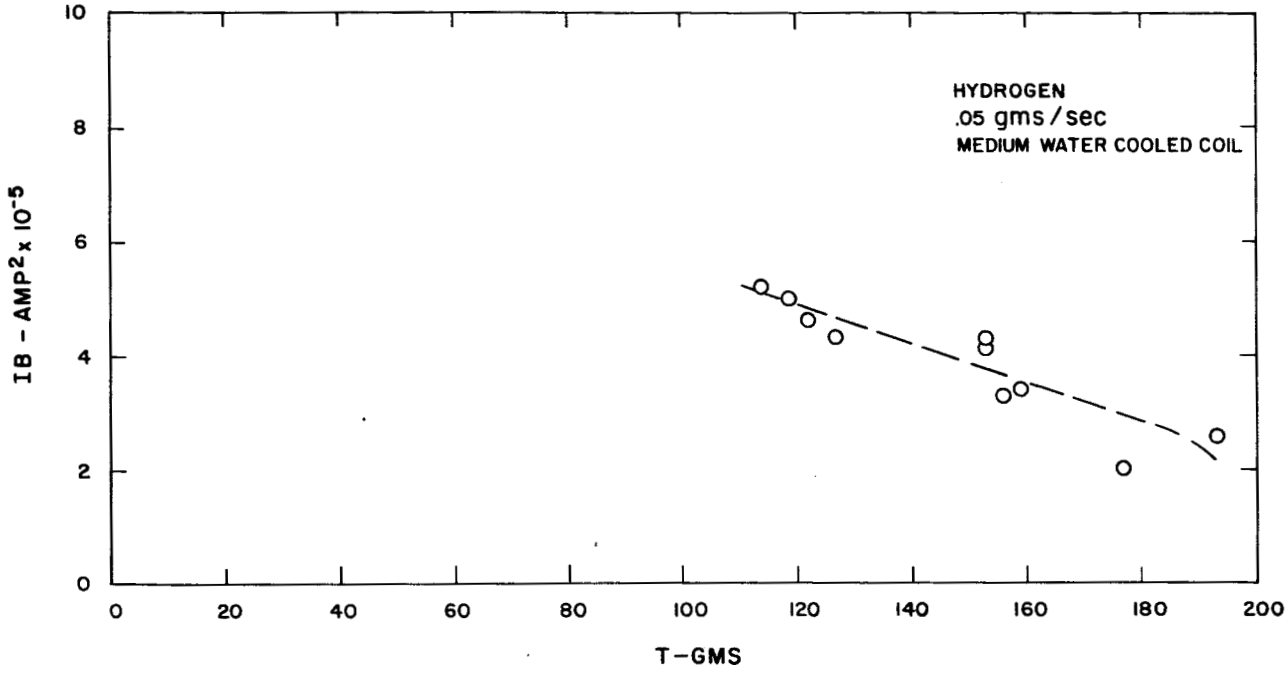

Fig. 29 IB vs thrust characteristics of the MAARC in hydrogen operating with a medium water cooled coil at constant mass flow and essentially constant power level.

A3273

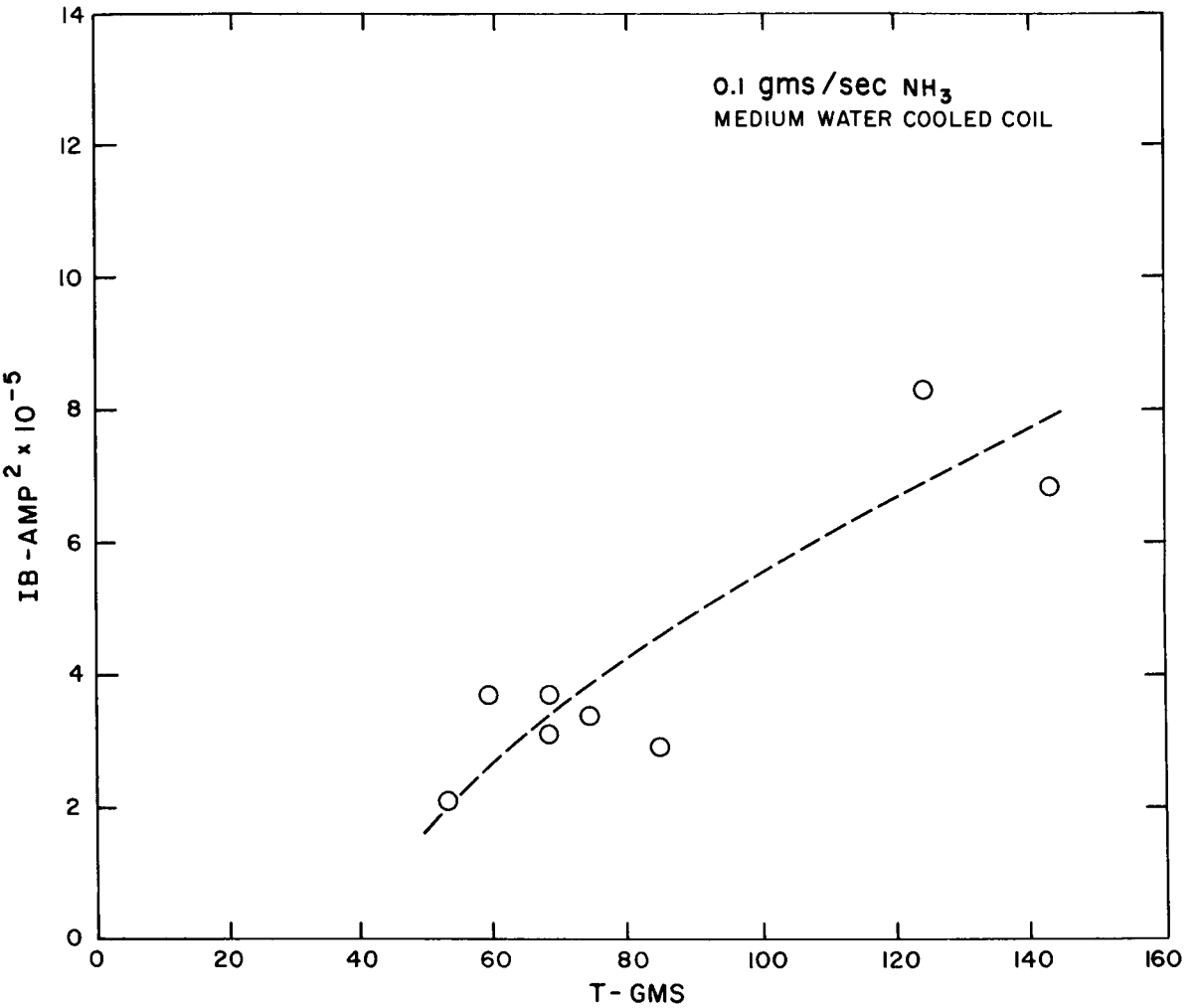

Fig. 30 IB vs thrust characteristics of the MAARC in ammonia operating with a medium water cooled coil at constant mass flow and essentially constant power levels.

A3274

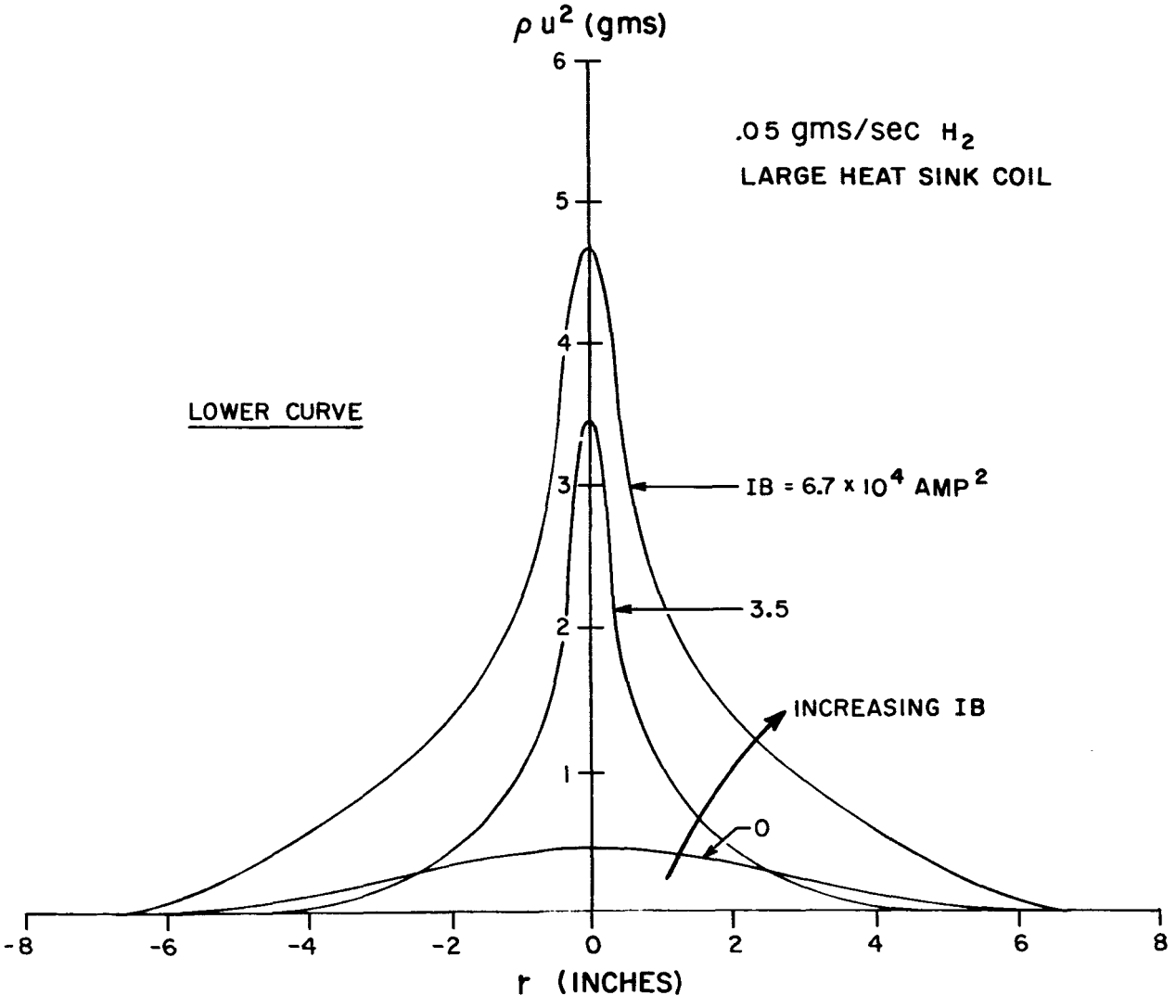

Fig. 31 ρu^2 profiles in hydrogen representing points on the lower curve of Fig. 26.

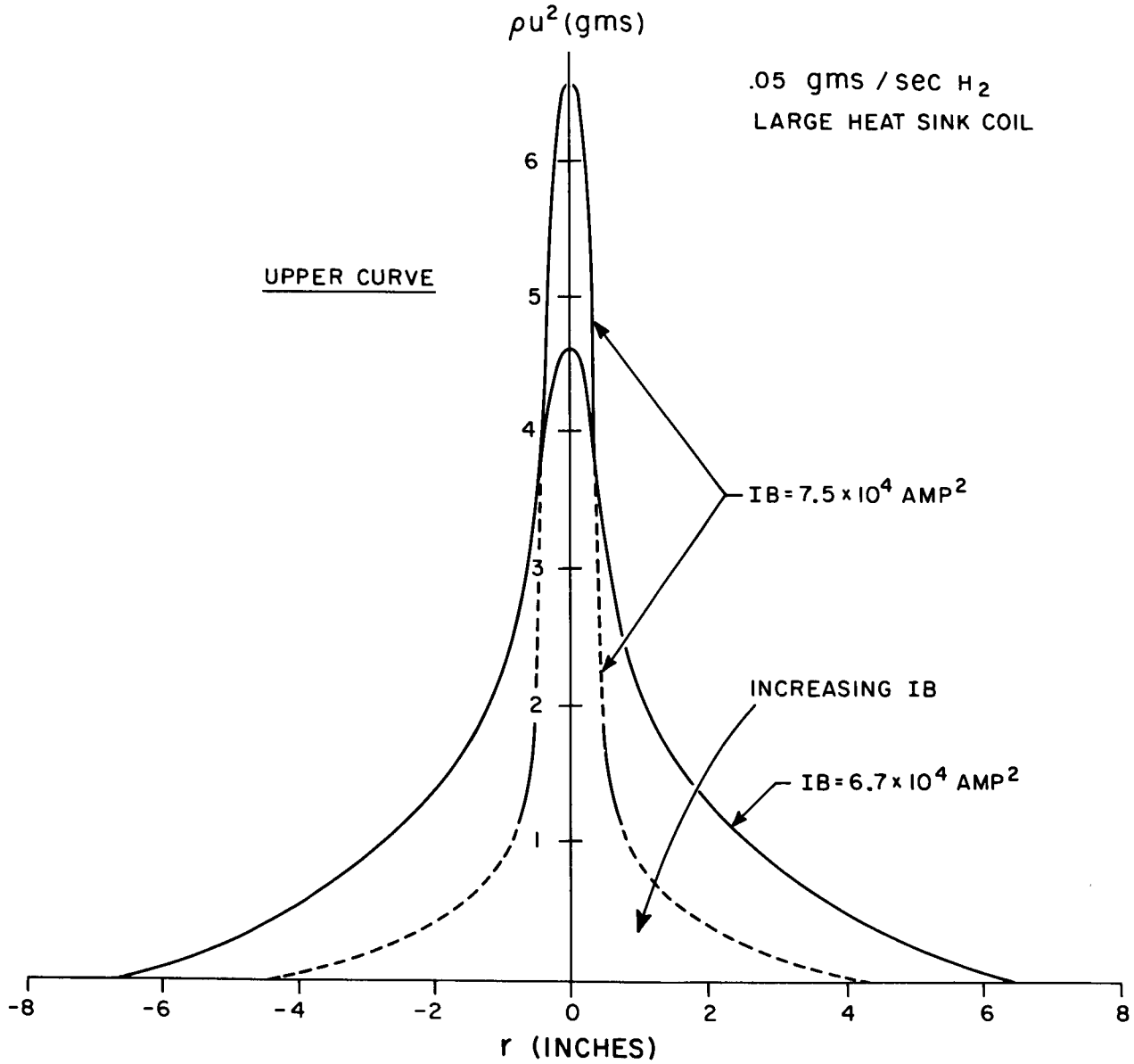

Fig. 32 ρu^2 profiles in hydrogen representing points on the upper curve of Fig. 26.

A3276

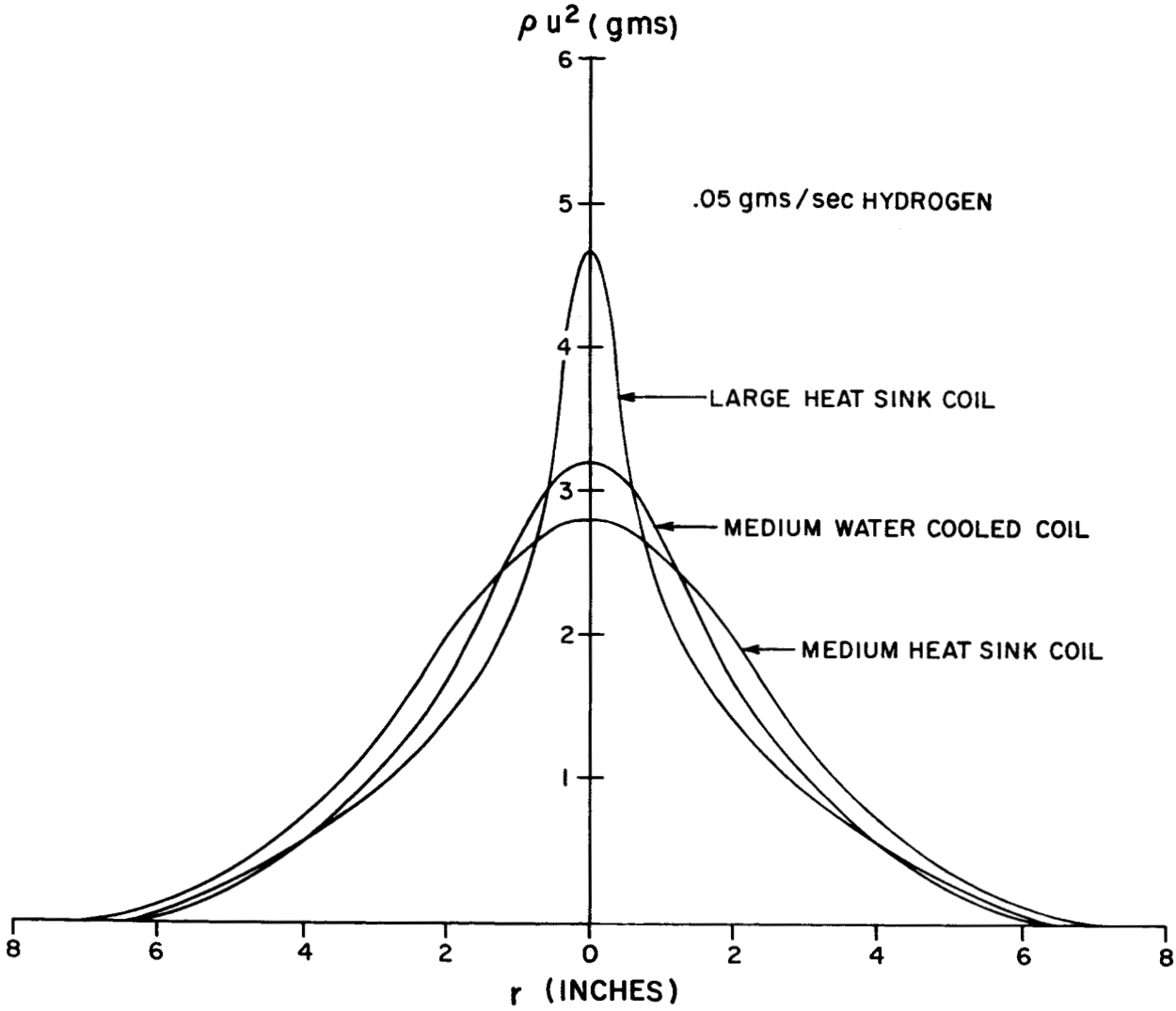

Fig. 33 ρu^2 profiles in hydrogen obtained with several different coils.

A3277

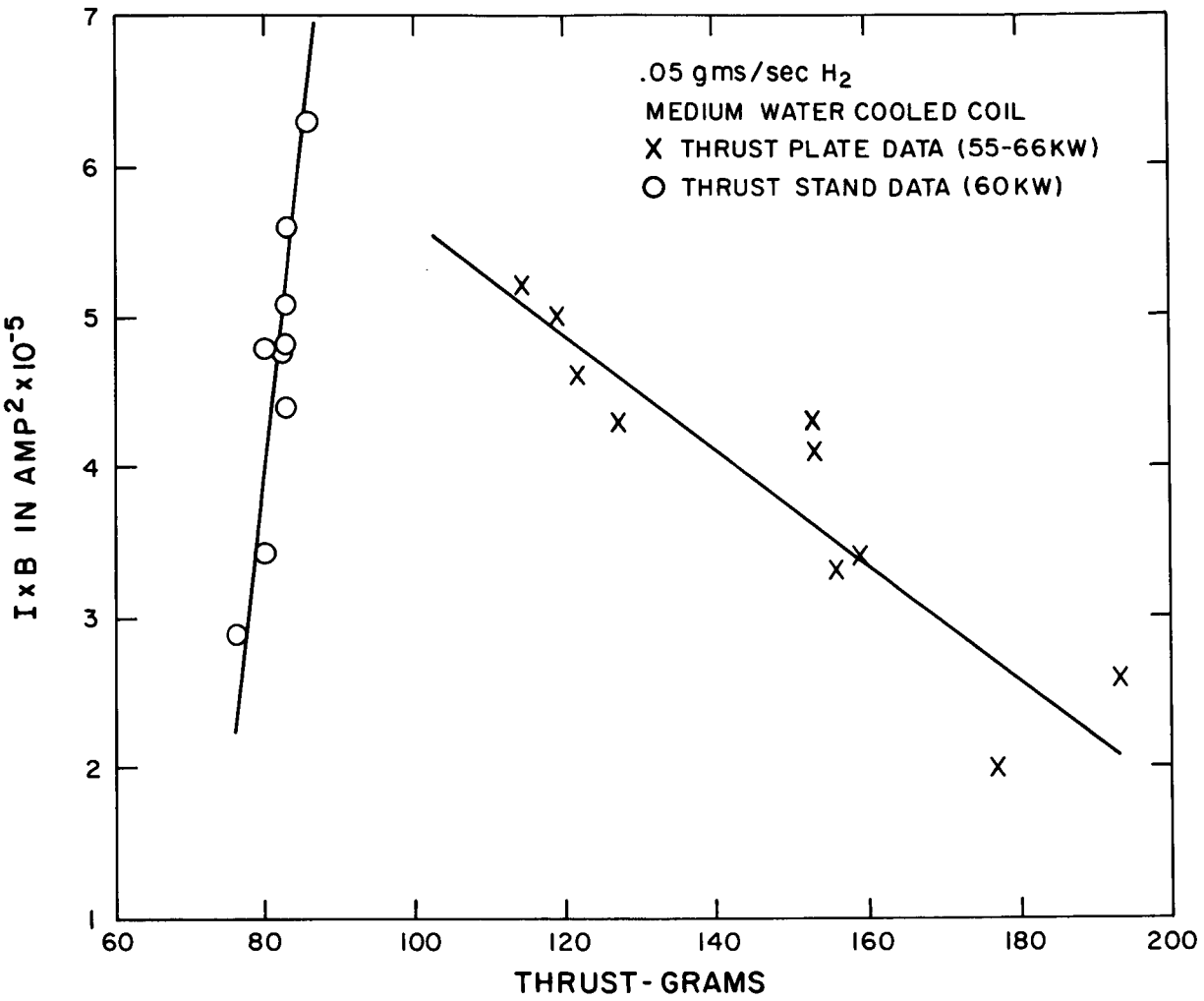

Fig. 34 Comparison of thrusts obtained from thrust stand measurements and thrust density profiles.

A3664

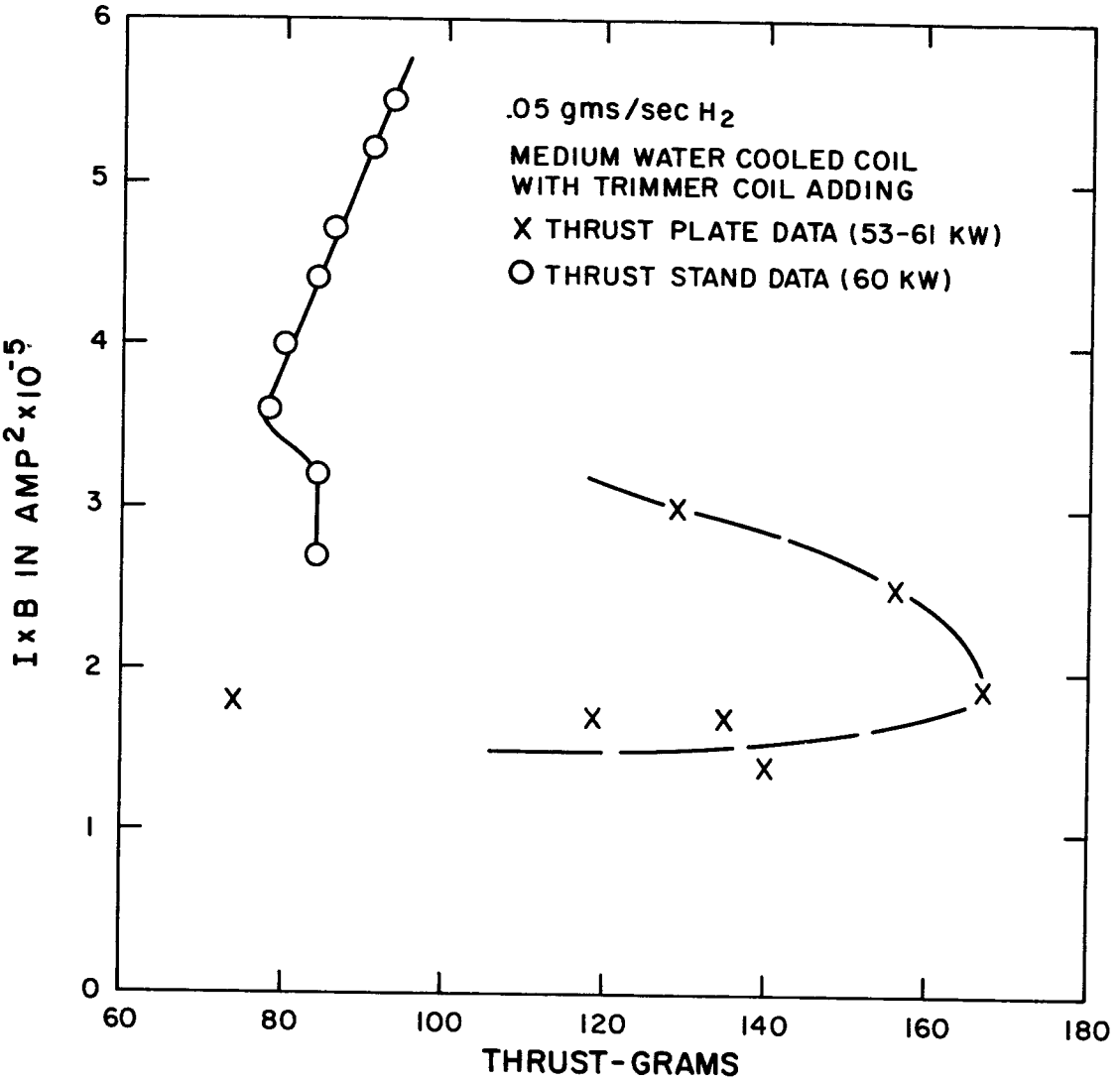

Fig. 35 Comparison of thrusts obtained from thrust stand measurements and thrust density profiles.

A3665

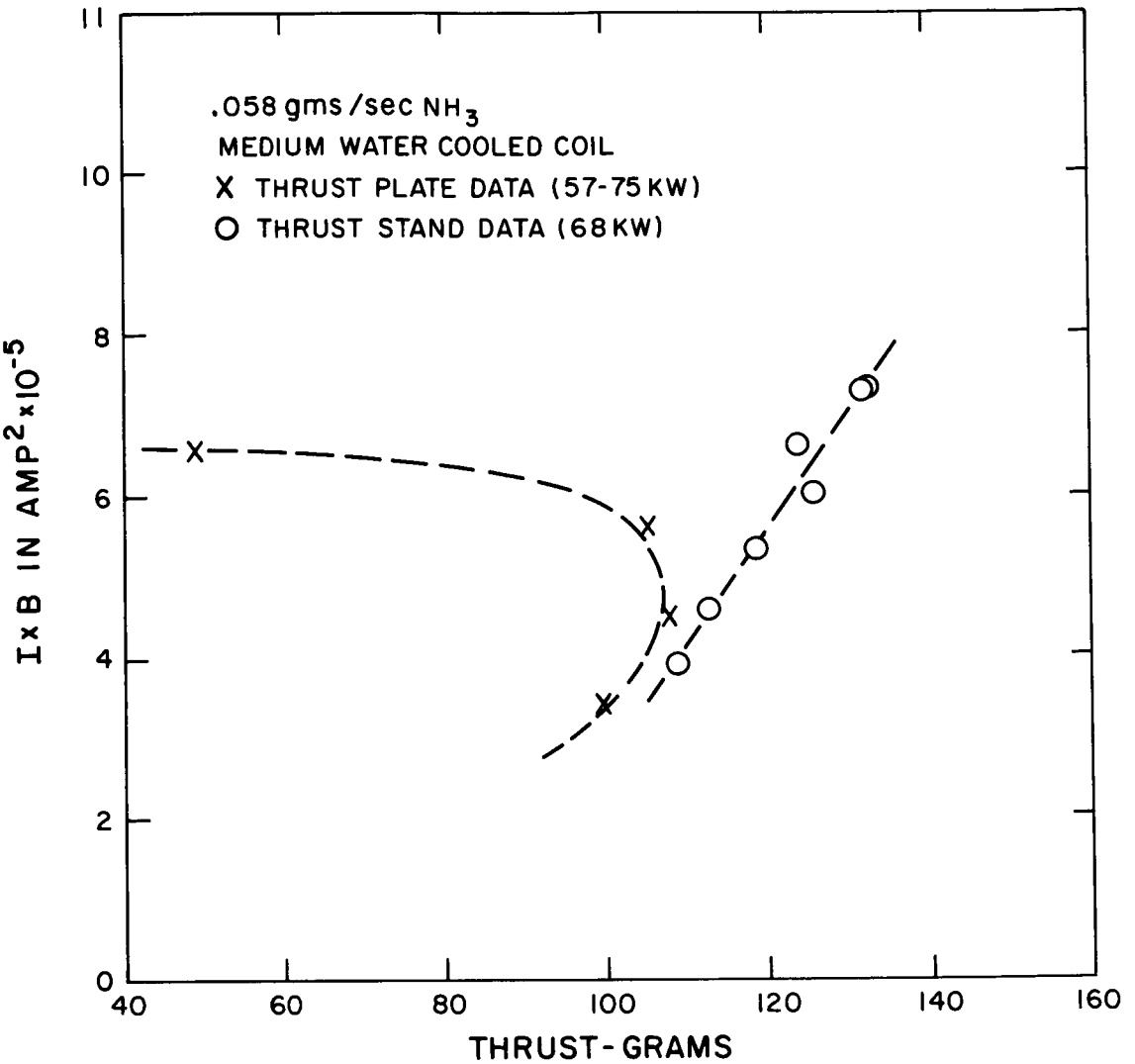

Fig. 36 Comparison of thrusts obtained from thrust stand measurements and thrust density profiles.

A3666

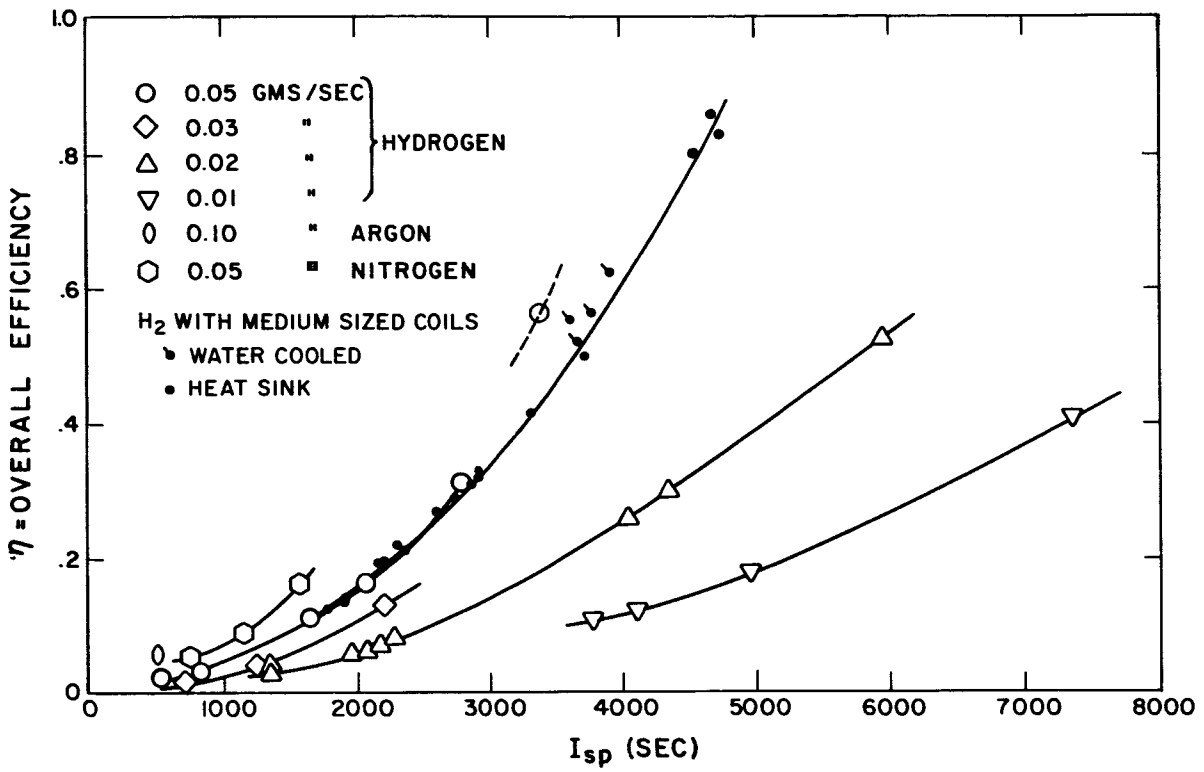

Fig. 37 The thrust efficiency, η vs I_{sp} for various propellants and mass flows. Open symbols represent data obtained with the large heat sink coil; solid symbols represent data for .05 gms/sec hydrogen.

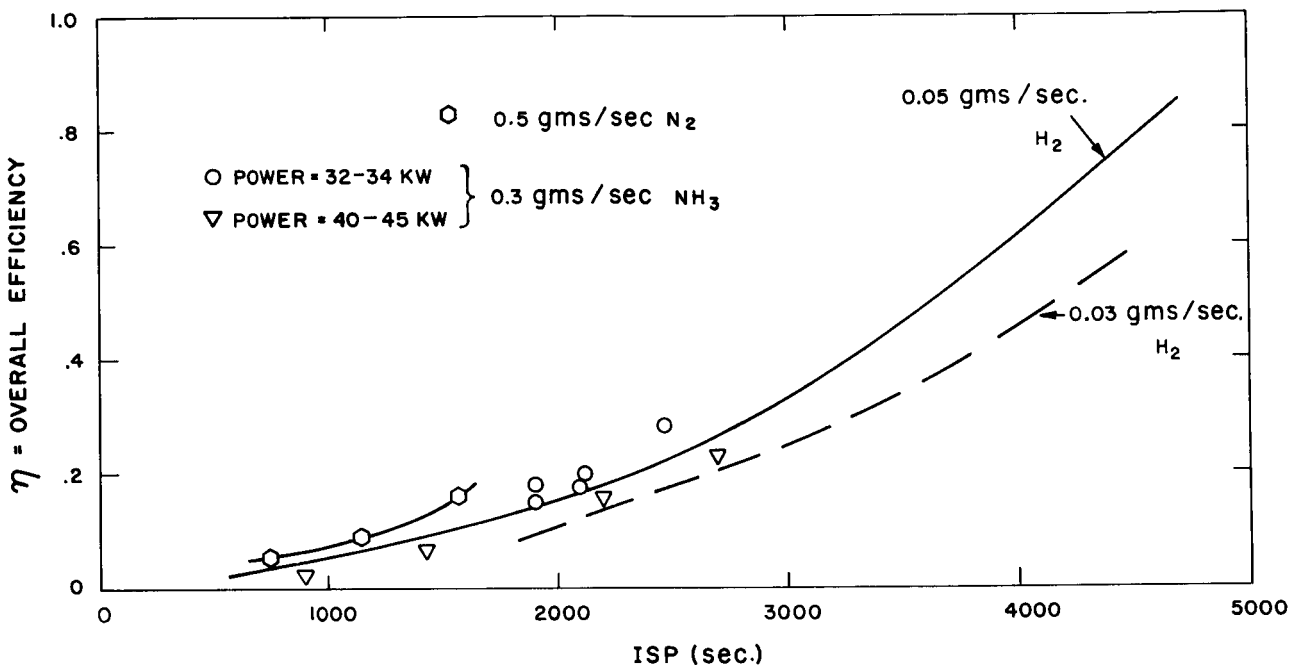

Fig. 38 Thrust efficiency, η vs I_{sp} in ammonia. The hydrogen data is taken from Fig. 37 The ammonia data was obtained with the medium water cooled coil.

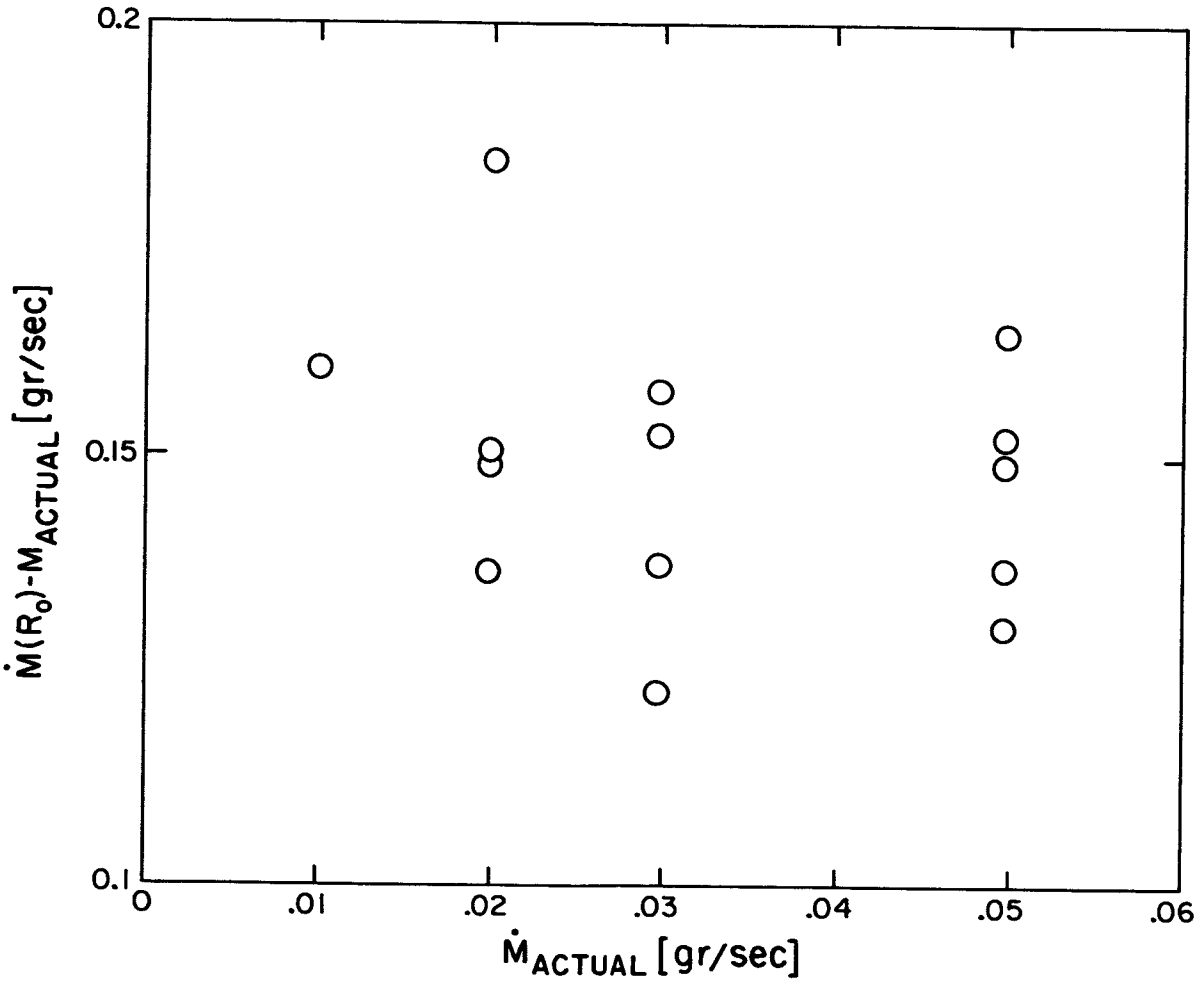

Fig. 39 Amount of entrained flow versus actual mass flow throughput in the MAARC.

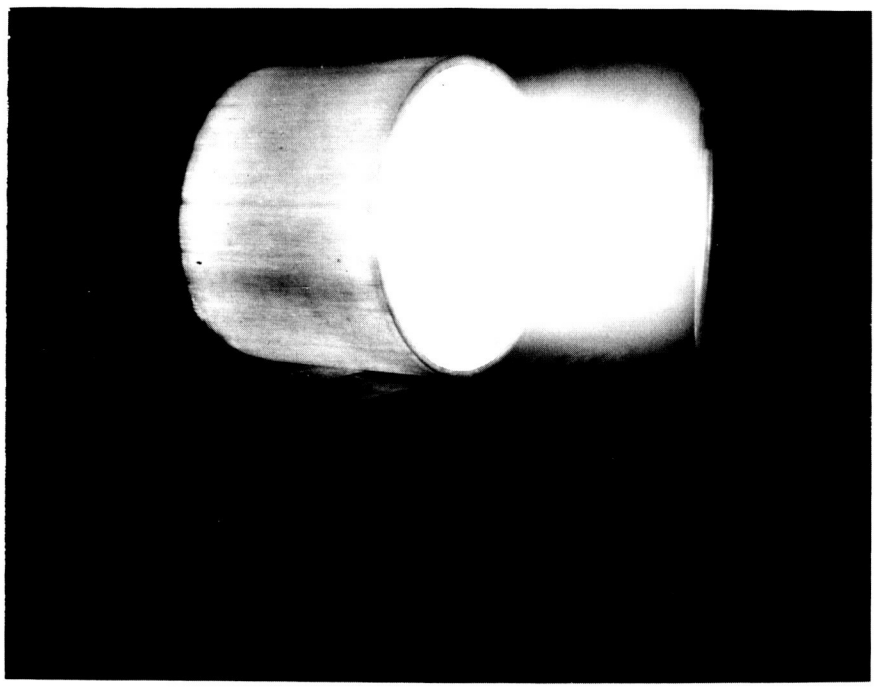

Fig. 40 Photograph of the MAARC operating with a qartz shroud.

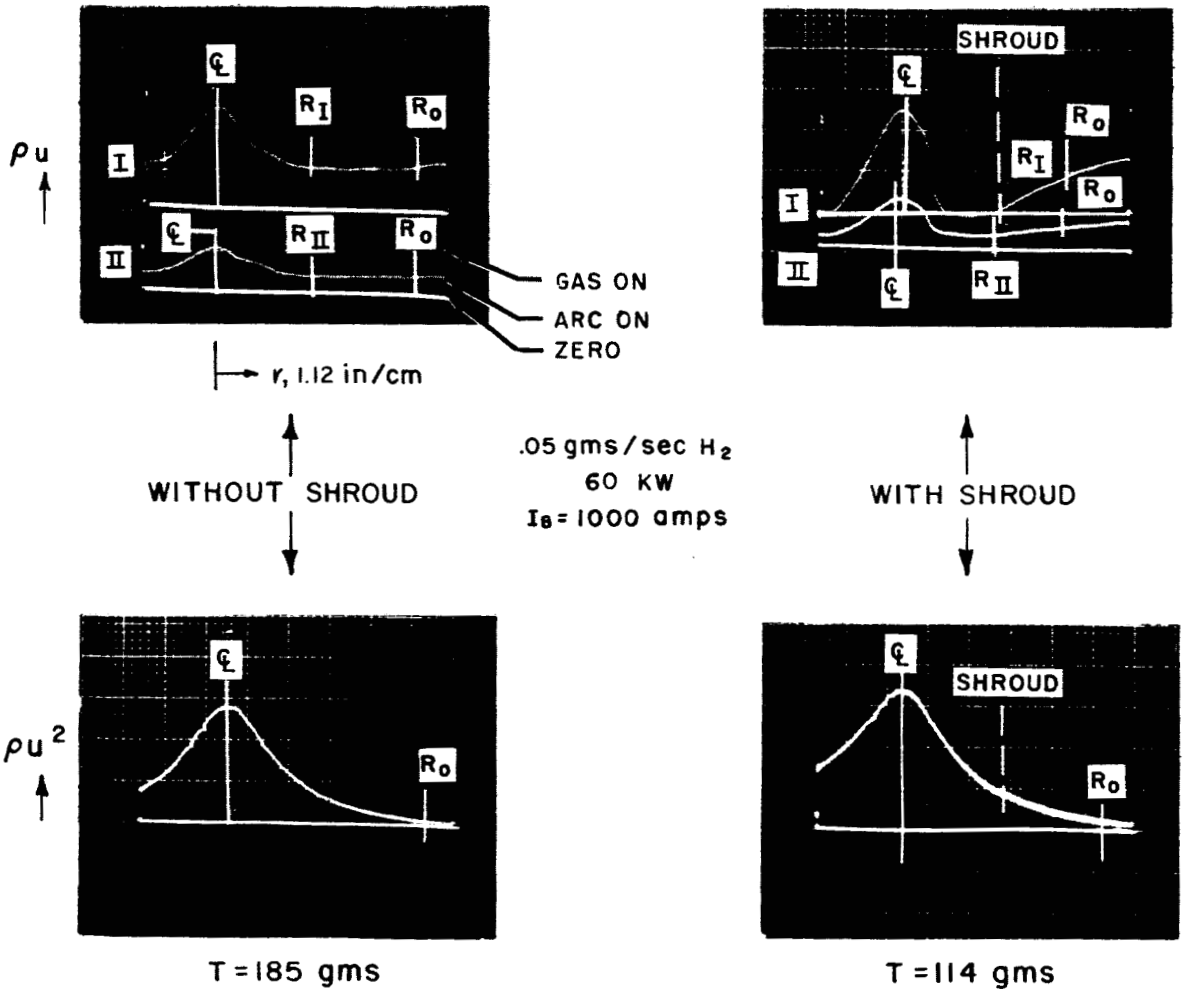

Fig. 41 ρu and ρu^2 oscillograms obtained with and without the quartz shroud.

A4261

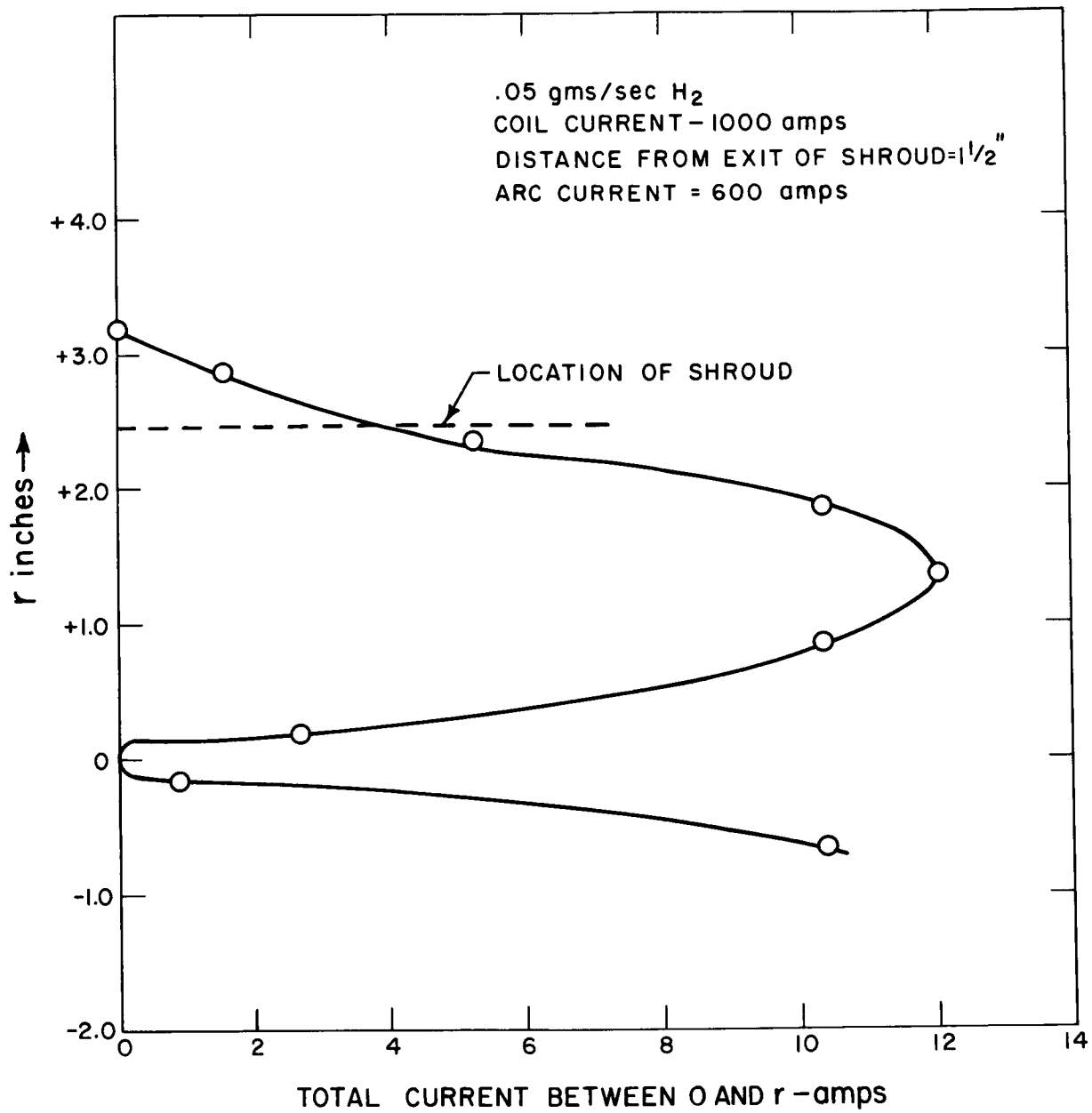

Fig. 42 Axial current distribution in the MAARC.

A4265

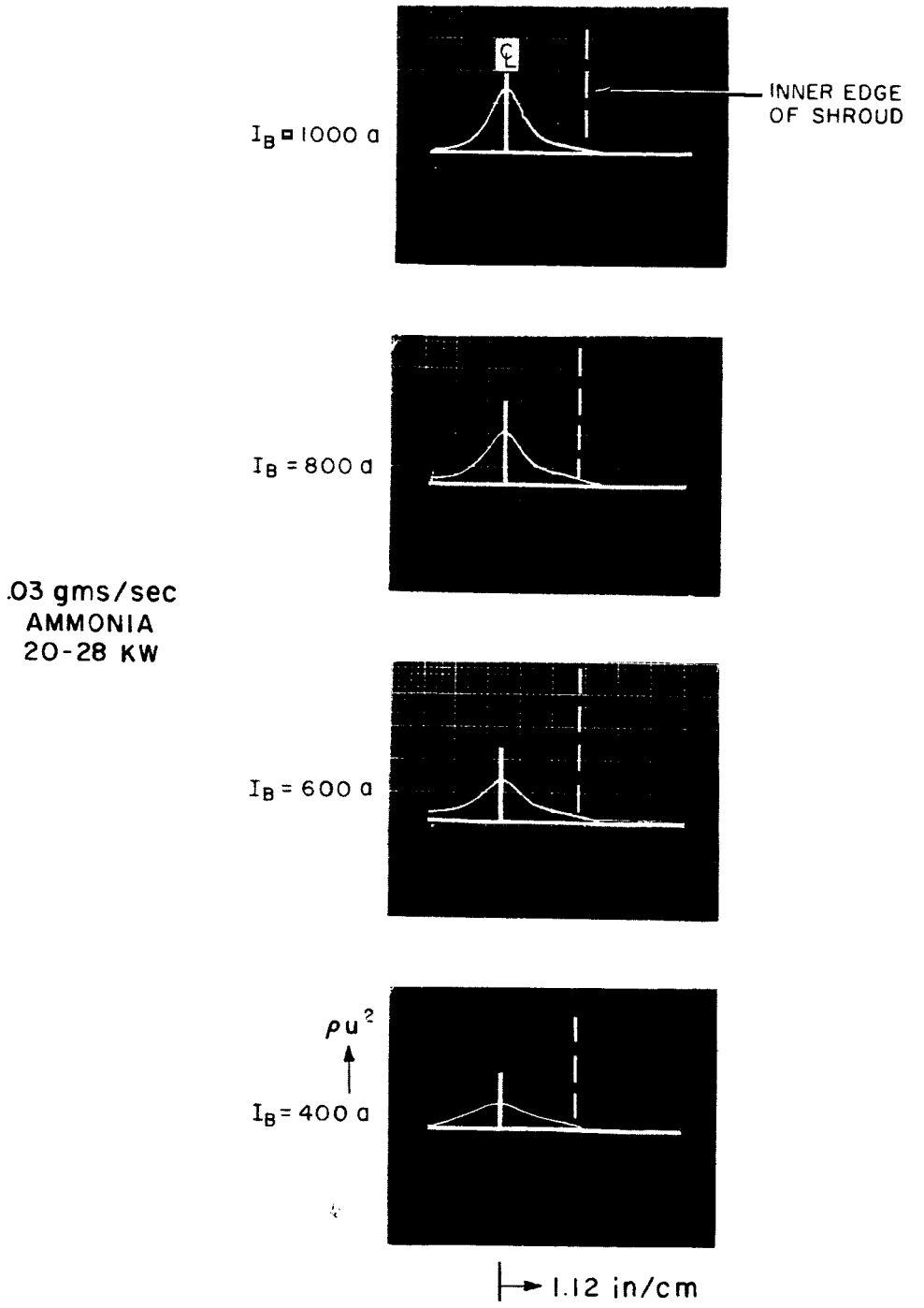

Fig. 43 ρu^2 measurements in ammonia with quartz shroud.

A4266

ADDENDUM*

During the period from September 15, 1965 through January 14, 1966 two further aspects of the Magnetic Annular Arc were studied.

The data on thermal efficiencies in ammonia which was discussed in the body of this report was correlated with an expression of the form

$$\eta_{thermal} = 1 - \frac{\alpha}{1 + \frac{U_c B \ell}{V_o}}$$

The quantity α, which is the ratio of the anode voltage drop to V_o was found to remain relatively constant over the experimental range. This data was observed to scale as predicted by the above relation for changes in B and V_o. A tabulation of data obtained at AERL, Avco RAD, and EOS for different propellants in general followed the trend predicted above for changes in $\eta_{thermal}$ with U_c/V_o.

Mode changes in ammonia were observed and identified as the result of changes in V_o with the parameter ℓ remaining constant. It was found that these mode changes could be controlled by changes in the axial cathode location. It was also observed that those modes possessing low V_o's yielded higher thermal efficiencies as was expected from the above relation for thermal efficiency.

A second study involved measurements of the axial and Hall current distributions in the MAARC exhaust. Rogowski and $\dot{B}_\theta$ coils were used for this study and it was observed that less than 15% of the MAARC current extended outside the anode. The active region of the anode was identified by painting it with insulating paint. This region was found to be quite small and well inside the nozzle. Based on these measurements, a model of the current distribution was proposed in which the bulk of the arc current flows well inside the anode, while the remaining current flows out along magnetic field lines in two distinct regions, possibly as a result of the probes, supports or tank walls providing a short circuit path across magnetic field lines.

---

* Numerical figure numbers, references and equation numbers refer to the body of this report, alphabetical notation refers to this addendum.

Optimization of Thermal Efficiency [g]

For space propulsion applications, where the pressure ratio across the MAARC will be effectively infinite, the thrust efficiency is limited by the degree of ionization and/or dissociation present since both azimuthal swirl energy and thermal energy are recoverable in the expansion process. Therefore, high thrust efficiency can be obtained in MAARC type devices by $\vec{j} \times \vec{B}$ acceleration or supersonic heating, since both these forms of energy addition keep the static temperature (and hence the degree of ionization and/or dissociation) low. It may also be possible to use propellants with high frozen flow efficiencies (e.g., lithium) and achieve desirable thrust efficiencies at high degrees of ionization if multiple ionization can be suppressed. It is felt presently by several investigators of MPD arcs that high thrust efficiencies have been achieved with the above mechanisms occurring singly or in combination.

The achievement of overall propulsive efficiencies in excess of 50% requires thermal efficiencies also in excess of 50%. This section deals primarily with a parametric study of the thermal efficiency of the MAARC. It will be shown that over the operating range studied, the thermal efficiency increases with increases in the quantity $U_c B\ell / V_o$ defined below.

Previously[1] it has been shown that over an extremely large range of operating conditions, the operating voltage of the MAARC is given by the relation

$$V = V_o + U_c B\ell \qquad (a)$$

where U_c is the so-called "critical speed" and is the velocity a particle has when its kinetic energy equals the energy required to ionize and dissociate it, B is the magnetic field strength, and ℓ is a characteristic length of the order of the anode-cathode spacing. The quantity V_o is an integration constant related to the anode and cathode voltage drops. Fig. 17 is a plot of arc voltage versus magnetic field obtained with various propellants in the MAARC. The lines drawn through the data were obtained from Eq. (a), where V_o and ℓ were adjusted to best fit the data. The values of ℓ ranged from .8 to 1.0 cm, compared to an anode-cathode radial separation of 1 cm at the cathode tip.

The critical speeds used in Fig. 17 along with the values of V_o are summarized in the table on page 22.

It has been observed[8] that under some operating conditions the anode heat transfer can be characterized by an anode voltage drop, V_o', so that

$$\dot{Q}_{anode} \cong IV_o' \qquad (b)$$

It is also true that the cathode heat transfer is less than 10% of the anode heat transfer and so for the purposes of this discussion, it has been neglected.

If it is further assumed that the anode voltage drop is related to the quantity V_o by a constant α, so that

$$V_o' = \alpha V_o \qquad (c)$$

Combining Eqs. (a), (b) and (c) with the definition of thermal efficiency results in the relation

$$\eta_{thermal} = -\alpha \frac{V_o}{V} = 1 - \frac{\alpha}{1 + \frac{U_c B\ell}{V_o}} \qquad (d)$$

It can therefore be concluded that under the assumption above, $\eta_{thermal}$ increases for approximately constant α as the quantity V_o/V decreases, or $U_c B\ell/V_o$ increases.

It then remains to investigate the assumptions of Eqs. (b) and (c) experimentally, and to discuss certain aspects of the quantity V_o in greater detail.

Anode Voltage Drop

To verify the assumption of Eq. (b), the anode heat transfer is plotted as a function of arc current in Fig. 22. The heat transfer to the anode is determined from the steady state temperature rise of a known flow rate of water which is used to cool the anode.

The power supply for the MAARC is so constructed that in this operating range, large changes in arc voltage produce much smaller changes in arc current; for example, a change in arc voltage from 50 to 100 volts

produces only a 20% decrease in arc current. During any given run, the arc voltage was changed by changing the magnetic field, while the arc current changed very slightly. It was observed that under these conditions of constant current and V_o during a run, the anode heat transfer was also quite constant, hence, each point on Fig. 22 represents one complete run. Comparison of the data in Fig. 22 shows good agreement with similar data reported by R. John et al.[8] The line plotted in Fig. 22 was obtained by linear extrapolation of this data to lower arc currents, since their experiments were at arc currents in excess of 600 amps. In this figure, the open symbols correspond to the low voltage mode whereas the solid symbols were obtained in the high voltage mode described in the last section. The data of Fig. 22 therefore represents an anode voltage drop of between 20 and 50 volts determined from the slope of lines drawn from the origin and bracketing the data points. Note that the data from Ref. 8, which is at much higher currents, has similar scatter, but represents a more constant anode voltage drop of 26 volts. As can be seen from the distribution of open and solid symbols, the variation in anode heat transfer at fixed arc current is due mostly to changes in the quantity V_o. It can therefore be concluded that the assumption of constant V_o' is rather crude over the range of experiments described here, but becomes more nearly true at the higher currents of Ref. 8.

Relation of V_o and V_o'

In Fig. a, a plot is presented of V_o' as a function of V_o for the data discussed in this paper. The slope of this curve is the quantity α, and it can be seen that α ranges between 0.5 and 0.8 for the bulk of the data. Hence, although wide variations in the anode voltage drop V_o' were demonstrated in the last section, corresponding changes in the quantity V_o result in a reasonably constant value of α. Hence, it is to be expected that Eq. (d) should be qualitatively, if not quantitatively, useful in determining the thermal efficiency of the MAARC.

Thermal Efficiency of the MAARC as a Function of Arc Power and $\frac{U_c B\ell}{V_o}$

A summary of the thermal efficiencies obtained in ammonia as a function of electrical input power to the MAARC is presented in Fig. 23.

The lines drawn on this figure connect typical sets of data points obtained during a single run in which only the magnetic field strength was varied and the quantity V_o was observed to remain constant. This data was obtained at approximately constant current and should not be construed as indicating that the thermal efficiency is a function of arc power. It is plotted in this way merely to indicate the range of operation which has been covered in ammonia. On each curve the higher values of efficiency correspond to higher magnetic field strengths, and at a given arc power, movement to higher efficiency curves correspond to decreasing values of V_o. Again, in this figure the open symbols correspond to the low voltage mode and the solid symbols to the high voltage mode of Fig. 10.

In Fig. b all data of Fig. a having a V_o of 40 volts is shown. This plot further demonstrates the effect of changes in V_o on the thermal efficiency of the MAARC.

The measured thermal efficiency is plotted as a function of the parameter $\frac{U_c B\ell}{V_o}$ in Fig. c. The values of $U_c B\ell$ were deduced from the measured V-B characteristics. Also plotted in this figure is Eq. (d) for α's of .5 and .8. As can be seen, the bulk of the data is bounded by these theoretical curves. It should be noted that if α was constant for a given set of data, this data must lie along the appropriate theoretical line by definition. As for example, the 7 points lying on the $\alpha = .5$ curve, where obtained during a single run, where V_o and V_o' (and hence α) were observed to remain constant. These particular points, therefore, represent the variation in thermal efficiency with varying magnetic field strength.

Conclusion Regarding Thermal Efficiency

Eq. (d) has been proposed as a useful relation for estimating the thermal efficiency of an MPD arc under the assumption of constant α. The MAARC has been operated in ammonia over the range 10 to 25 kw with mass flows of .02 to .05 gms/sec, and it has been demonstrated experimentally that ℓ is constant (0.5 cm) and α is approximately constant (0.5 to 0.8) for these experiments. The externally applied magnetic field has been varied and changes in V_o accomplished by changes in cathode location. It has been shown that the thermal efficiency of the MAARC does indeed vary

in accordance with Eq. (d) for changes in both V_o and B. Thermal efficiencies up to 75% have been achieved in ammonia and this level is apparently limited only by the magnetic field strength available in the MAARC facility.

It is useful to speculate on the effect of the use of other propellants on the thermal efficiency of an MPD arc based on the above results.

The following table is constructed from data given in Refs. 1, 13 and a, and from the additional sources cited.

Propellant	$U_c \times 10^{-4}$ m/sec	V_o volts	$(U_c/V_o) \times 10^{-3}$ m/sec/volt	Approximate maximum observed η_{therm} near 4000 gauss
H_2	5.5	45	1.22	90%
NH_3	2.6	36	.72	75%
A	.87	15	.58	70%
Li[c, d]	1.2	22[c, d]	.55	(35%[c] 86%[d])*
N_2	1.6	30	.53	55%
Na[e]	.65	13[e]	.50	(40%[e])*
K[f]	.46	10[f]	.46	(30%[f])*
Ce[b]	.23	16[b]	.15	38%[b]

* This data is for radiation cooled engines where $\eta_{thermal}$ is not known. The values given are maximum $\eta_{overall}$ and hence represent the minimum possible $\eta_{thermal}$ for these cases (i.e., η_{thrust} assumed unity).

From this table it is qualitatively apparent that the termal efficiency increases with increasing values of U_c/V_o over the wide range of propellant choice and operating conditions included in this table. If this trend is indeed quantitatively correct, it leads one to the conclusion that higher values of the product $B\ell$ are required when the use of propellants with lower critical speeds is found necessary from other considerations. At the present time, for a given geometry an increase in the product $B\ell$ in fact means an increase in the magnetic field itself, since the parameters which control ℓ are as yet unknown.

Axial Current Distribution in the Exhaust[j]

Current distributions have been obtained in MPD arcs operated in argon by Cann[h] and in hydrogen, ammonia, nitrogen and argon by Powers[i] by the measurement of magnetic field gradients with small Hall effect sensors. This section deals with similar measurements obtained in hydrogen and ammonia by monitoring with various search coils the decay of these currents as the arc is extinguished. A description of this relatively simple technique for current measurements will be presented along with some conclusions about the current distribution in the MAARC.

Diagnostic Technique

Fig. d is a schematic representation of what is known as a Rogowski loop or coil. With the use of Maxwell's equations in integral form, it can be shown that the voltage V is proportional to the change in the current I linked by this loop. First observe that

$$\oint_S \vec{B} \cdot d\vec{S} = \mu_o \int \vec{j} \cdot d\vec{A} = \mu_o I \qquad (e)$$

where $\vec{B}$ is the magnetic induction, $\vec{S}$ is the arc length along the loop, $\vec{A}$ the area of the loop, $\vec{j}$ the current density and I is the total current passing thru the loop.

In addition,

$$\int \vec{E} \cdot d\vec{s} = - \int \frac{\partial \vec{B}}{\partial t} \cdot d\vec{a} \qquad (f)$$

where $\vec{E}$ is the electric field, $\vec{s}$ is the arc length along the coil and $\vec{a}$ is the cross sectional area enclosed by the winding.

Then, for unit arc length of $\vec{S}$, Eq. (f) can be integrated so that

$$\epsilon = na \frac{dB_S}{dt} \qquad (g)$$

where ϵ is the E. M. F. induced in the coil per unit length along $\vec{S}$, n is the number of terms per unit length along $\vec{S}$ and B_S is the component of $\vec{B}$ along $\vec{S}$. Then, from (g) it follows that

$$B_S = \frac{1}{na} \int \epsilon \, dt \qquad (h)$$

so that

$$\mu_o I = \int \vec{B} \cdot d\vec{S} = \int B_S dS = \frac{1}{na} \int \nu dt \qquad (i)$$

were $\nu = \int \epsilon dS$ is the total voltage induced across the Rogowski loop.

If an integrating circuit such as that shown in Fig. d is used, then it is well known that the output of this circuit, V, is given by

$$V = \frac{1}{RC} \int \nu dt \text{ for } RC \gg \tau$$

where τ is the time over which ν is to be integrated. Hence, finally

$$I = \frac{1}{\mu_o} \frac{RC}{na} V \qquad (j)$$

Note that this result is independent of the shape of the Rogowski loop and depends only on the choice of RC and na. Since n is the number of terms per unit length, this result is independent of the size (length) of the Rogowski loop. Also, since it is independent of the current distribution thru the loop, it can be easily and accurately calibrated by simply placing a conductor anywhere thru the loop and passing a known current thru it. Care must be exercised when Rogowski coils are used to prevent sensitivity of the coil to changes in the magnetic field passing through the plane of the coil. This can be done by connecting one end of the coil to a conductor passing through the center or along the outside of the coil (as in Fig. d), or by winding the coil in an even number of layers (as was done for the experiments reported here) so that both ends of the winding terminate at the same end of the loop.

By using Rogowski coils with different major diameters at a given axial position (Fig. i) the total axial current can be inferred. As the loop diameter is increased, (c' to b') the total current through the loop increases until the region of return currents is entered. At this point (b'), the current will start decreasing until at the edge of the current region it reaches zero. The total axial current flow will then correspond to the maximum observed current through the loop, as the loop diameter is increased from c' to a'.

A special case arises when azimuthal symmetry exists. For this case, it is only necessary to use a short segment of a Rogowski coil and

measure $\frac{dB_\Theta}{dt}$, where B_Θ is the azumuthal component of $\vec{B}$. Then we find that

$$I = \frac{1}{\mu_o} \frac{RC}{Na} V\, 2\pi r \qquad (k)$$

Where N is the total number of turns of a small coil aligned with its axis in the Θ direction and r is the distance of the coil from the axis of symmetry. This is equivalent the previous result since $n = \frac{N}{2\pi r}$. A schematic of such a $\dot{B}_\Theta$ coil can be seen in Fig. 13.

Since the MAARC is a D.C. device, this technique is only applicable during the start-up or shut-down periods when changes of I with time occur. Then the requirement that equations (j) or (k) hold is that $RC \gg \tau$, the time required for the current to build up or extinguish itself. In addition, it is clear that for greater sensitivity, the RC should be held small to yield large V's at a given I. Hence these two requirements must be balanced in a given coil. It is also evident that τ should be made as small as possible to increase the coil sensitivity.

Description of Coils

A primary difficulty in the use of these techniques is the problem of electrostatic pick up. Three methods have been used to minimize this effect:

1. All coils used in this study have been double wound-center grounded (Fig. 13) and the outputs have been observed with a differential preamplifier.
2. The coils have been covered with an electromagnetically thin (.001"-.010") grounded Faraday shield.
3. The coils have been terminated with an impedence of approximately 20 times their own resistance.

These methods have eliminated any measurable electrostatic pick up in the data presented below.

$\dot{B}_\Theta$ Coil

Fig. 13 is a schematic representation of the $\dot{B}_\Theta$ coil used in these experiments. Shown in this figure is the double wound-center grounded technique employed to eliminate electrostatic effects. With the assumption of azimuthal symmetry, this coil can be used to estimate axial currents as

low as 1 amp. Thermal insulation was accomplished in a manner similar to that used with the Rogowski coils and resistance measurements were also made to determine coil integrity. The coil was calibrated by comparing its output to measurements of its output when the field produced by the MAARC field coil was turned off.

It was observed that initiation of the arc occurs in a relatively irregular fashion, taking of the order of 10^{-1} sec to reach steady state, whereas the termination of the arc occurred in a more regular way in approximately 5×10^{-3} sec; both these results probably resulting from the nature of the MAARC power supply. For this reason, all data reported in this paper was obtained during the shut-down of the MAARC.

The $\dot{B}_\theta$ coil had an RC time of 4×10^{-2} sec compared to the termination time of 5×10^{-3} sec, thus introducing an error on the order of 15% into these measurements. The zero level for the $\dot{B}_\theta$ signal was determined from the level of the trace after at least five RC times had elapsed.

Rogowski Coils

Three different Rogowski coils were used to study the current distribution in the exhaust of the MAARC. The geometric shapes of these coils are presented in Fig. e, along with their sensitivity. The coils were wound with number 38 or 42 magnet wire. These coils had an n of from 500 to 1000 turns per inch in four layers and were wound with a 1/8" I. D.

The coils were encased in quartz tubing and the region between the coils and the quartz was filled with a high temperature ceramic material (Sauereisen), or quartz fiber for thermal insulation and structural strength. With run durations of 1 to 2 seconds and manual cooling of the coils between runs, the quartz and ceramic shielding were all that was needed to maintain the integrity of the coils, except several coils burned out when placed far upstream in the nozzle. The variation in resistance of the coils from run to run was accurately measured to determine any possible internal shorting.

To increase the Rogowski coil sensitivity, the termination time τ for the arc was decreased by crowbarring it with a conventional mechanical switch. In this way the termination time was reduced to less than 10^{-4} sec. A RC time for the Rogowski coil integrator of 10^{-2} sec was used which easily satisfies the requirement that $RC \gg \tau$. A set of contacts on the

crowbarring switch pretriggered the oscilloscope 1 to 5 x 10^{-3} sec before the arc termination and a sweep speed of 5 x 10^{-3} sec/cm provided a trace of 5 integration time constants. This technique permits evaluation of the zero level before and after termination of the MAARC. In all cases these two levels corresponded, which leads to the conclusion that extraneous D.C. signals were absent from the Rogowski coil measurements.

The observation of a very large luminous exhaust,[j] when a MPD arc is operated at a very low back pressure, indicates that Rogowski coils up to 10 ft. in diameter may be useful in determining the extent of the arc currents. The hand winding of coils of such size is a very long and difficult undertaking; however, commercially available delay line is a satisfactory substitute. For example, Columbia Technical Corporation HH1600 delay cable consists of #38 magentic wire wound at approximately 200 turns per inch on a 1/8" diameter ferrite core. With such delay line it is only necessary to connect one end of the coil to the cables shielding and take the signal from the other end of the winding and the adjacent shielding. A second grounded shielding placed around the cable along with appropriate termination should eliminate any electrostatic effects. The coil diameter can be changed for a given loop by doubling up the loop. This technique should easily lead to sensitivities of better than 10 amps. The loop can again be calibrated by terminating the current through a conductor passing thru the loop in a time comparable to the shut-down time of the MPD arc. The effect of the ferrite core is automatically corrected for by this experimental calibration. Caution should be exercised in assuring that the ferrite core is not saturated, as this will affect the calibration linearity.

Experimental Results

Current distributions have been obtained in the MAARC exhaust using the various search coils. The hydrogen data was obtained with the $\dot{B}_\theta$ coil; the ammonia data was obtained with Rogowski coils.

Hydrogen Data

The $\dot{B}_\theta$ coil was used to make measurements of the axial current distribution at a fixed axial position in hydrogen at .05 gms/sec, 45 kw, 4200 gauss and a total MAARC current of 600 amps. The tank pressure for

these conditions was approximately 300μ. This data is shown in Fig. 42, where the total current contained within a radius r is plotted as a function of r. The currents were computed using Eq. (k). The measurements were obtained 1-1/2" downstream of a 6" x 6" quartz shroud, but are typical of the data obtained in the absence of the shroud at the same position. As can be seen from this figure, the axial current in hydrogen under these operating conditions 7-1/2" downstream from the exit plane of the anode indicated that less than 5% of the MAARC current flows in this external region and the data suggests that this small portion of the arc current flows out along magnetic field lines, crosses the field lines at some distance greater than 7-1/2" from the anode exit plane and returns to the anode again along magnetic field lines.

Ammonia Data

Measurements of the current distribution in the exhaust of the MAARC were made in ammonia at .02 gms/sec, 25 kw, 3200 gauss and a total MAARC current of 250 amps with the various Ragowski coils. The ambient tank pressure was of the order of 50 μ for these conditions. Some $\dot{B}_\theta$ coil data was obtained and found to be in agreement with the Rogowski coil data.

Figs. f and g are plots of the current passing through the 1-1/2" and 1" diameter Rogowski coils as a function of axial distance from the exit plane of the anode. Fig. h shows an ensemble of photographs of these coils in the MAARC flow.

Current Distribution Model for Ammonia Data

A model for the current distribution in the MAARC exhaust in ammonia under the above operating conditions is presented in Fig. i. It is postulated that the bulk of the MAARC current (that is: over 85%) is confined to a region far upstream in the anode while the remaining current (less than 15%) flows downstream in two distinct regions which are closely bounded by magnetic field lines. This downstream current flow may be related to the presence of the probes and their supports which could serve as short circuit paths across magnetic field lines. This model suggests that a Rogowski loop would measure an increasing current as it is moved from position (a) of Fig. i to position (b), since it would link less and less of the opposite signed

current of the anode region. From position (b) to position (c) the observed current should decrease as a decreasing fraction of the cathode region current is measured. Measurements with Rogowski loops of two different diameters would yield the total current in the cathode region (at position b) and could be used to determine the amount of radial current leakage between the anode and cathode regions.

The data of Figs. f thru h are compatible with this model. The 1-1/2" Rogowski coil yields a maximum signal ($\approx$ 35 amps or 14%) at approximately the same axial position where the cathode region just fills it. The 1" Rogowski coil does not show this effect as clearly, but it seems to flatten out at about the same current level and then starts rising again. This effect may result from the fact that the small coil represents a far larger (percentage-wise) obstacle to the flow as it is moved upstream, as is suggested by the photographs of Fig. h. It may, therefore, have an effect on the current pattern when it is moved far upstream.

The rectangular Rogowski coil was placed in the MAARC exhaust and aligned in the meridian plane so that it would be sensitive to azimuthal currents. Throughout the downstream flow region no signals were obtained, leading to the conclusion that the average Hall currents are less than 0.1 amps/cm^2. This result is compatible with the above model since if the meridian plane currents are everywhere parallel to the magnetic field, no Hall currents exist, even if $\omega\tau$ is large.

Current measurements well inside the nozzle are impractical at this time, so no details are known about the upstream currents. In order to determine the electrically active region of the anode, it was sprayed with an insulating paint (Glyptal). The MAARC was then operated in the normal fashion. The results of this are shown in Fig. j. As can be seen from this photo, only the furthest upstream portion of the anode is electrically active. No deviation from the normal operating conditions (current, voltage and visual appearance) were observed, but to further study the effect of the paint on the MAARC operation, a congruent case was tested. The regions where the paint was burned off the nozzle in Fig. j were painted and the rest of the nozzle was left bare. The result is shown in Fig. k and it is clear that an identical pattern to the previous one is obtained.

SUMMARY AND CONCLUSION

In this report, Rogowski coils have been proposed as a technique for gross measurement of currents in the exhaust of a MPD arc. These Rogowski coils have the advantages that they are relatively simple to construct, can be calibrated directly in that they have an output directly proportional to the current being measured and present a symmetric obstacle to the flow. No assumption of symmetry in the current distribution is required. They have the disadvantages that they provide gross current measurements rather than local current densities, do not provide continuous profiles since the arc must be terminated for each measurement and represent a large obstacle when made in small sizes or used for upstream in the exhaust. When constructed from delay cable, they are very attractive for measurements at low back pressures in large testing facilities.

A model has been proposed for the current flow in the MAARC when operated in ammonia at 0.02 gms/sec, 25 kw, 3200 gauss and a total MAARC current of 250 amps, at an ambient tank pressure of the order of 50μ. In this model, it is proposed that the majority of the MAARC current (85%) crosses the annulus well upstream in the nozzle, whereas the remaining current (15%) flows downstream in two distinct regions, roughly bounded by magnetic field lines. Experimental justification for this model can be summarized as follows:

1. Rogowski coil measurements indicate that less than 15% of the total MAARC current flows downstream of the exit plane of the anode.
2. Rogowski coil measurements corrolate with photographs of the MAARC exhaust to suggest that there is little axial change in the magnitude of this downstream current.
3. Photographs of the MAARC exhaust show the existence of two distinct regions whose boundaries correspond quite closely to magnetic field lines.
4. Rogowski coil measurements indicate that negligible Hall currents flow in the downstream region although estimates of $\omega\tau$ in this region indicate that it is greater than unity.

This suggests that the meridian plane currents are parallel to the applied magnetic field in this region.

5. Tests with an insulated anode show that only the furthest upstream portion of the nozzle (in the direct vicinity of the cathode) is electrically active.

Based on these observations, it is likely that most of the energy and momentum addition occurs far upstream in the anode under these operating conditions. Because of the very limited amount of ambient tank gas which is capable of diffusing into this region, it is unlikely that this type of entrainment is important under these conditions. The impedence for currents flowing downstream must be very high and it is possible that the vacuum tank walls or the Rogowski coils and their supports which cross magnetic field lines may be in some way responsible for the small currents which are observed outside the anode. Measurements of the extents of the arc currents at very low back pressures should shed a great deal of light on possible thrust measurement errors.

Based on the above results, the current patterns shown in Figs. 1 and i are the most likely distributions of MAARC currents under the given operating conditions.

REFERENCES

(a) R. M. Patrick and A. M. Schneiderman, "Performance characteristics of a magnetic annular arc", Sixth Symposium on Engineering Aspects of Magnetohydrodynamics, 1965, p. 70.

(b) S. Bennett, G. Enos, R. R. John and A. Tuchman, "MPD arc jet engine performance", presented at the AIAA Second Annual Meeting, San Francisco, Calif., July 26-29, 1965, AIAA Bull. 2, 297 (1965). AIAA Paper No. 65-296

(c) S. Bennett, Avco Corporation, Research and Advanced Development Division, private communication.

(d) R. A. Moore, et al., Electro-Optical Systems, Inc., Annual Report, Contract AF 33(615)-1579, June 1965.

(e) R. A. Moore, et al., Electro-Optical Systems, Inc., Semi-annual Report, Contract AF 33(615)-1579, September 1965.

(f) Electro-Optical Systems, Inc., Fourth Quarterly Progress Report, Contract NAS3-5909, June 20, 1965.

(g) A. M. Schneiderman and R. M. Patrick, "Optimization of the Thermal Efficiency of the Magnetic Annular Arc", presented at the Third Aerospace Sciences Meeting, AIAA, N. Y., N. Y., January 24-26, 1966. AIAA Bull. 2, 714 (1966). AIAA Paper No. 66-115.

(h) G. L. Cann, P. D. Lenn, and R. L. Harder, Hall Current Accelerator, Third Quarterly Progress Report NAS3-5909, 20 March, 1965.

(i) W. E. Powers, "Measurements of the Current Density Distribution in the Exhaust of an MPD Arc Jet" presented at the Third Aerospace Sciences Meeting, AIAA, N. Y., N. Y., January 24-26, 1966. AIAA Bull. 2, 714 (1966). AIAA Paper No. 66-116.

(j) R. M. Patrick and A. M. Schneiderman, "Axial Current Distribution in the Exhaust of the Magnetic Annular Arc", presented at the Fifth Electric Propulsion Conference, San Diego, California, March 7-9, 1966. AIAA Paper No. 66-198.

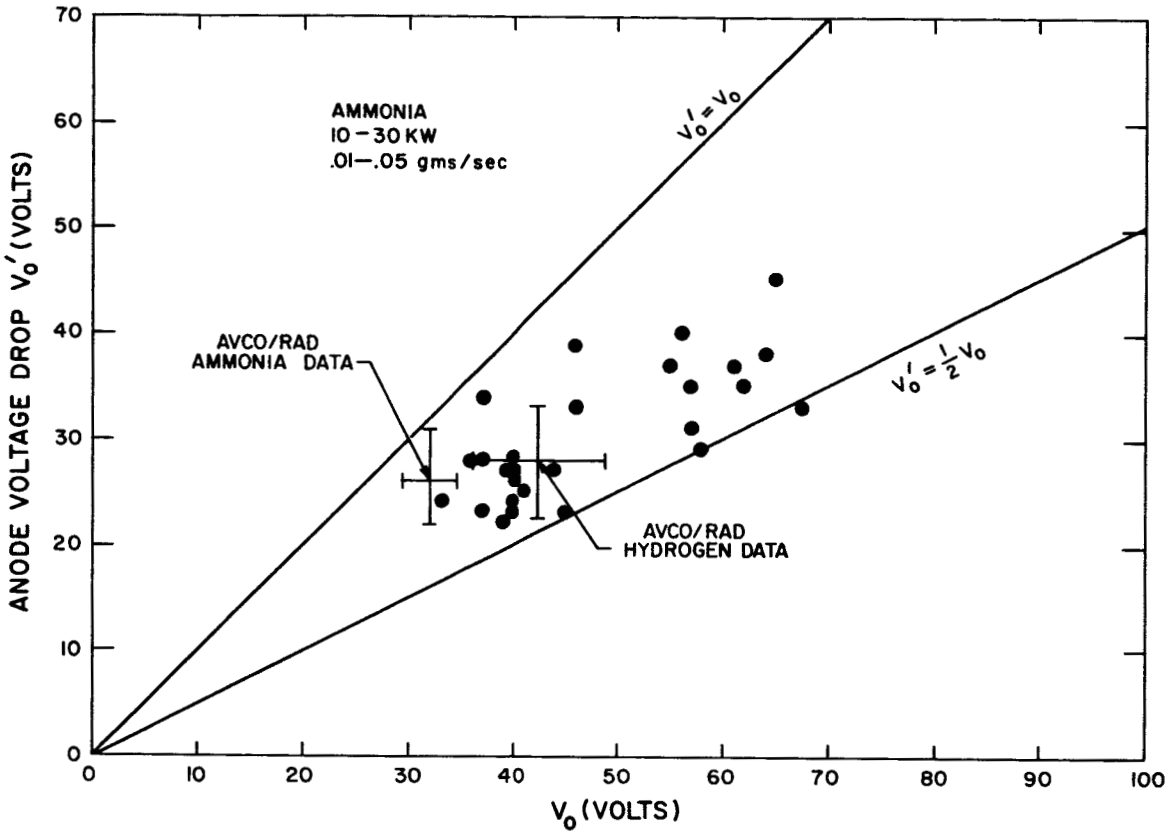

Fig. a Anode Voltage Drop vs the Constant V_o for Ammonia

A4684

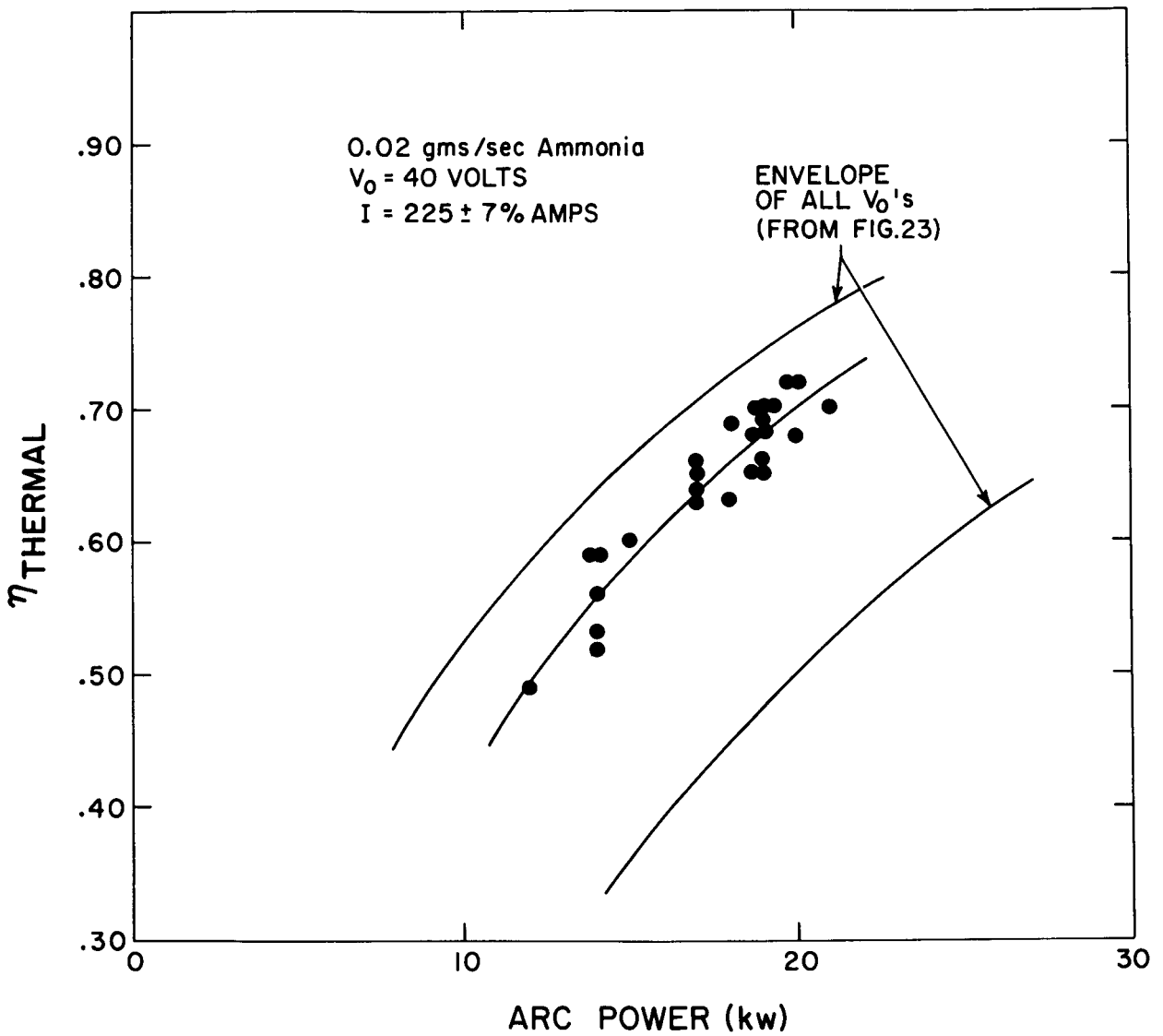

Fig. b Thermal efficiency vs input power at V_o = 40 volts. All data of Fig. 23 corresponding to V_o = 40 volts is shown.

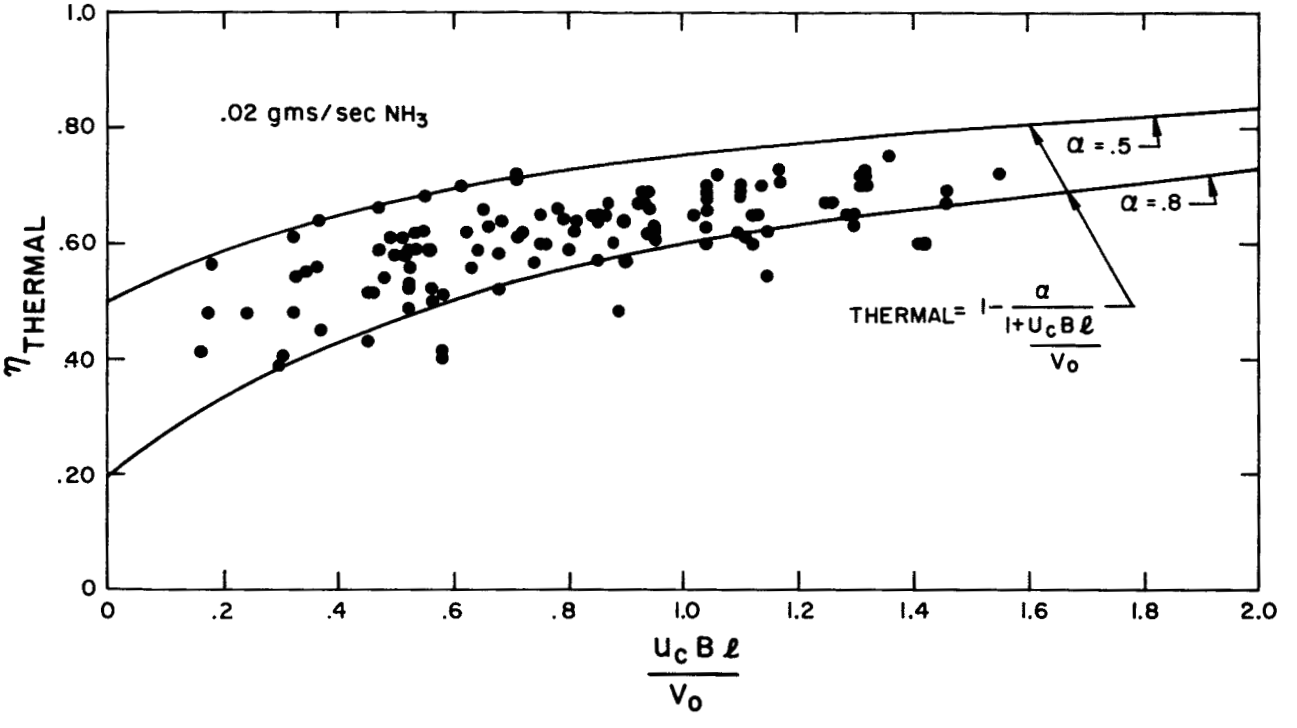

Fig. c The data of Fig. 23 plotted in terms of the parameter $\frac{U_c B \ell}{V_o}$.

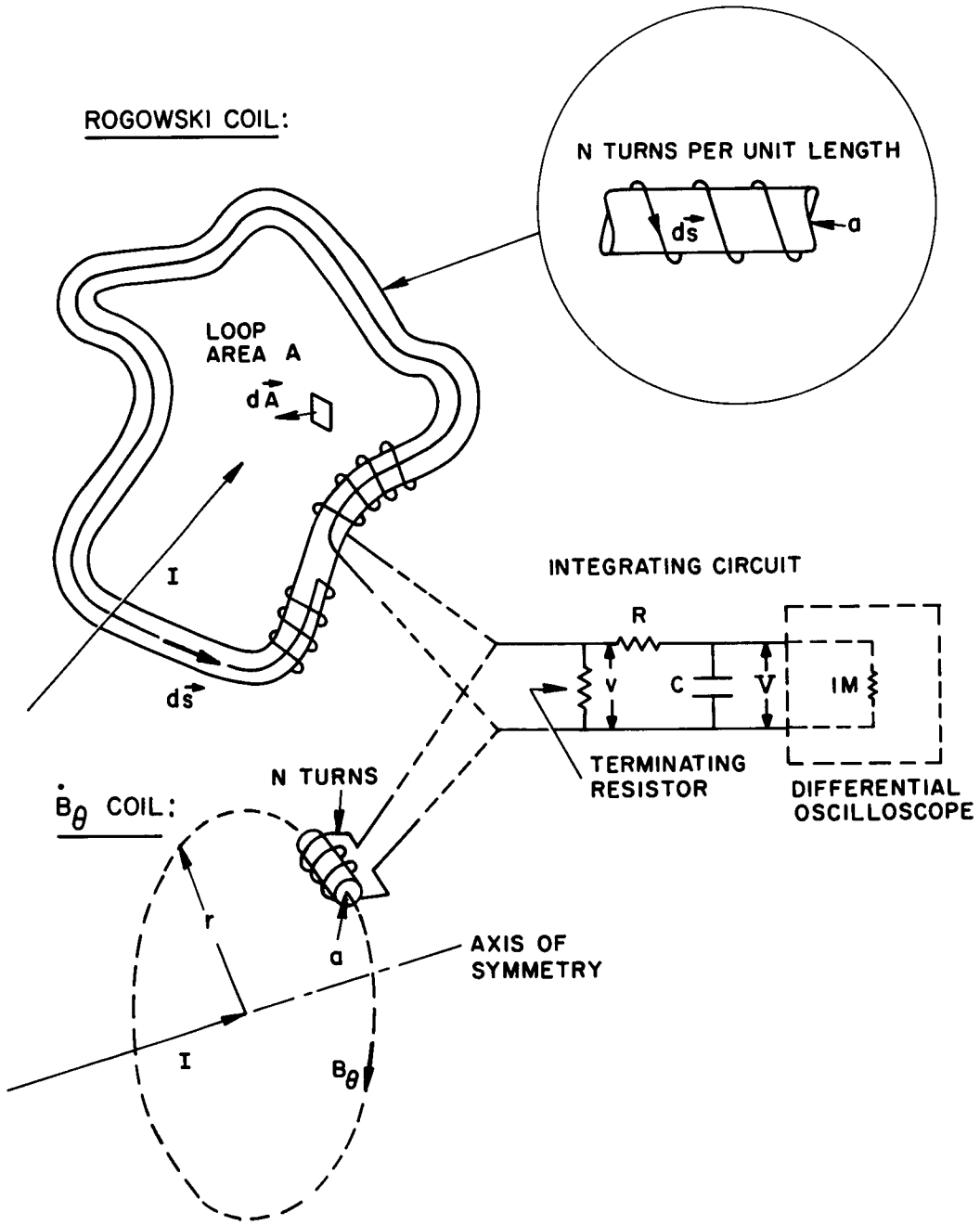

Fig. d Schematic representation of the Rogowski coil and $\dot{B}_\Theta$ coil showing defined terms used in the text.

A5051

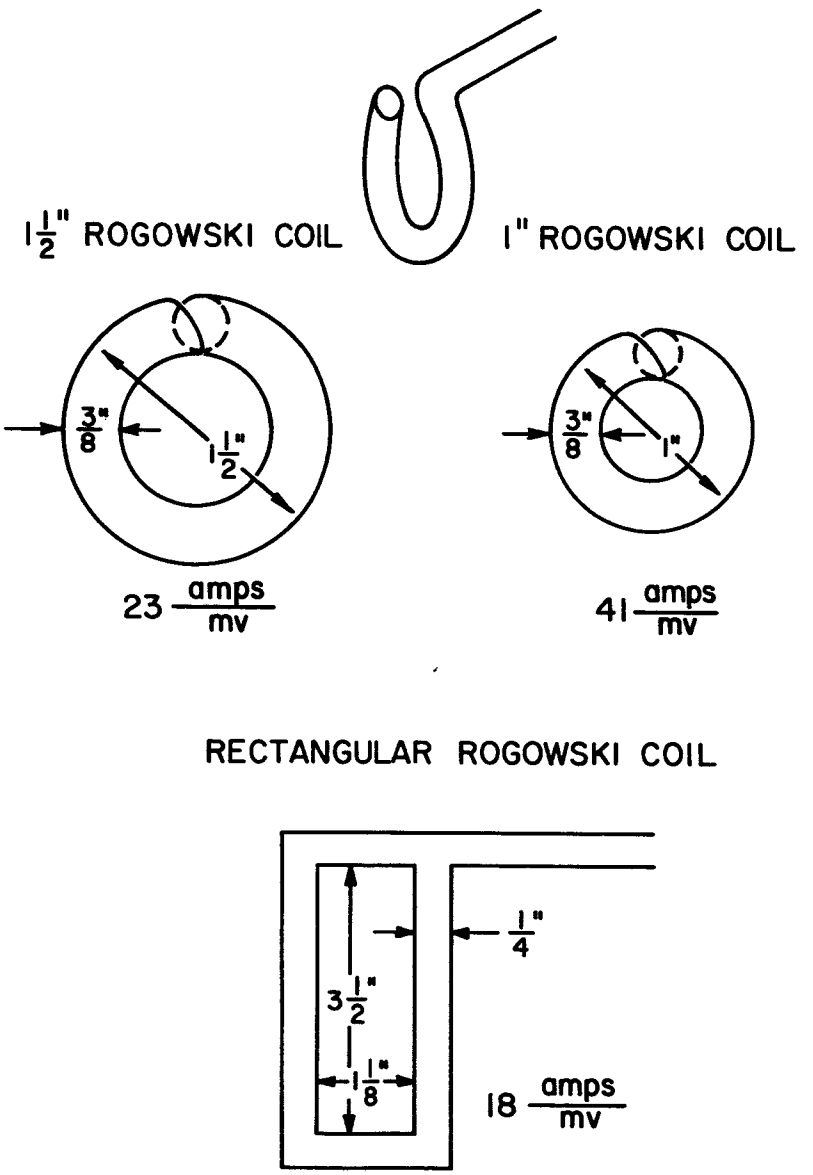

Fig. e Geometric characteristics of the Rogowski coils.

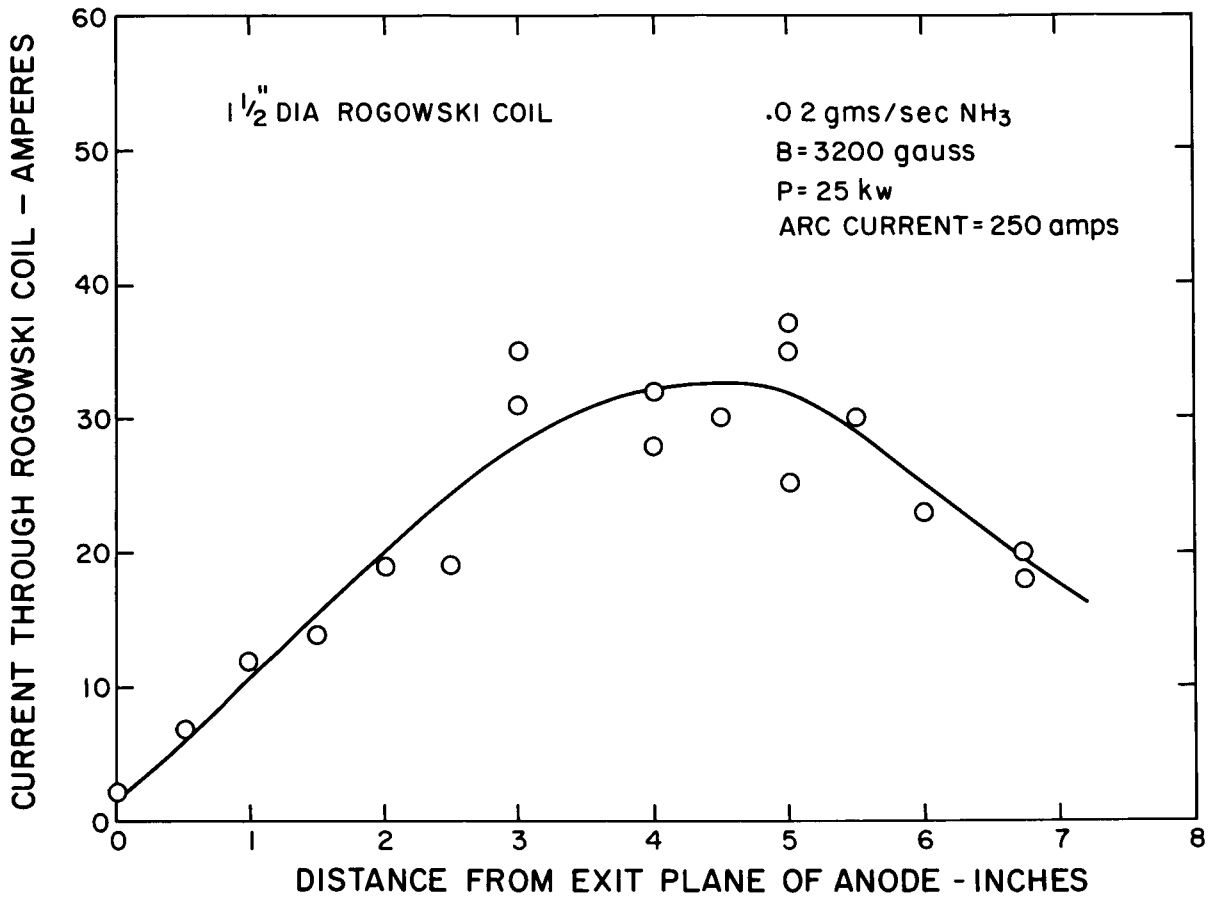

Fig. f Current thru the 1-1/2" Rogowski coil in ammonia as a function of axial position.

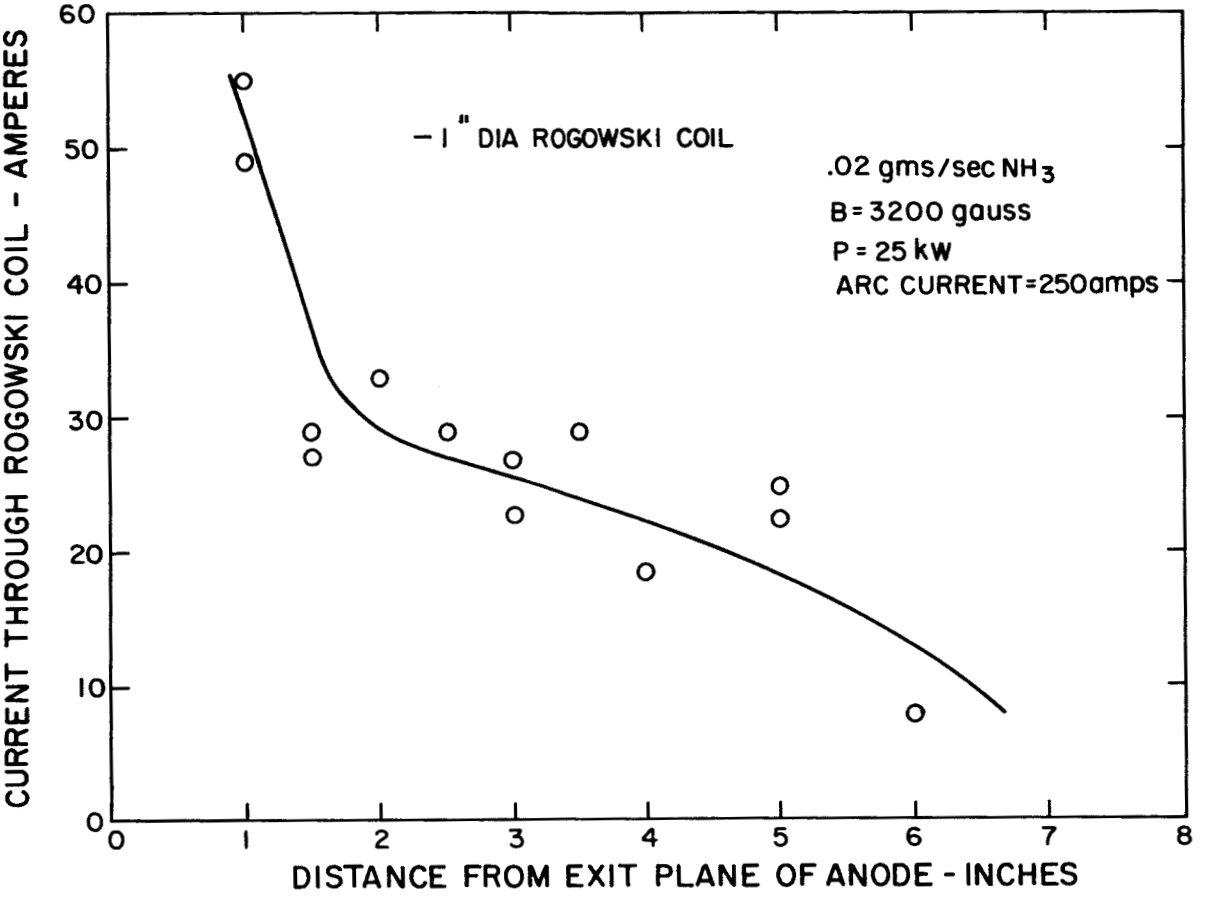

Fig. g Current thru the 1" Rogowski coil in ammonia as a function of axial position.

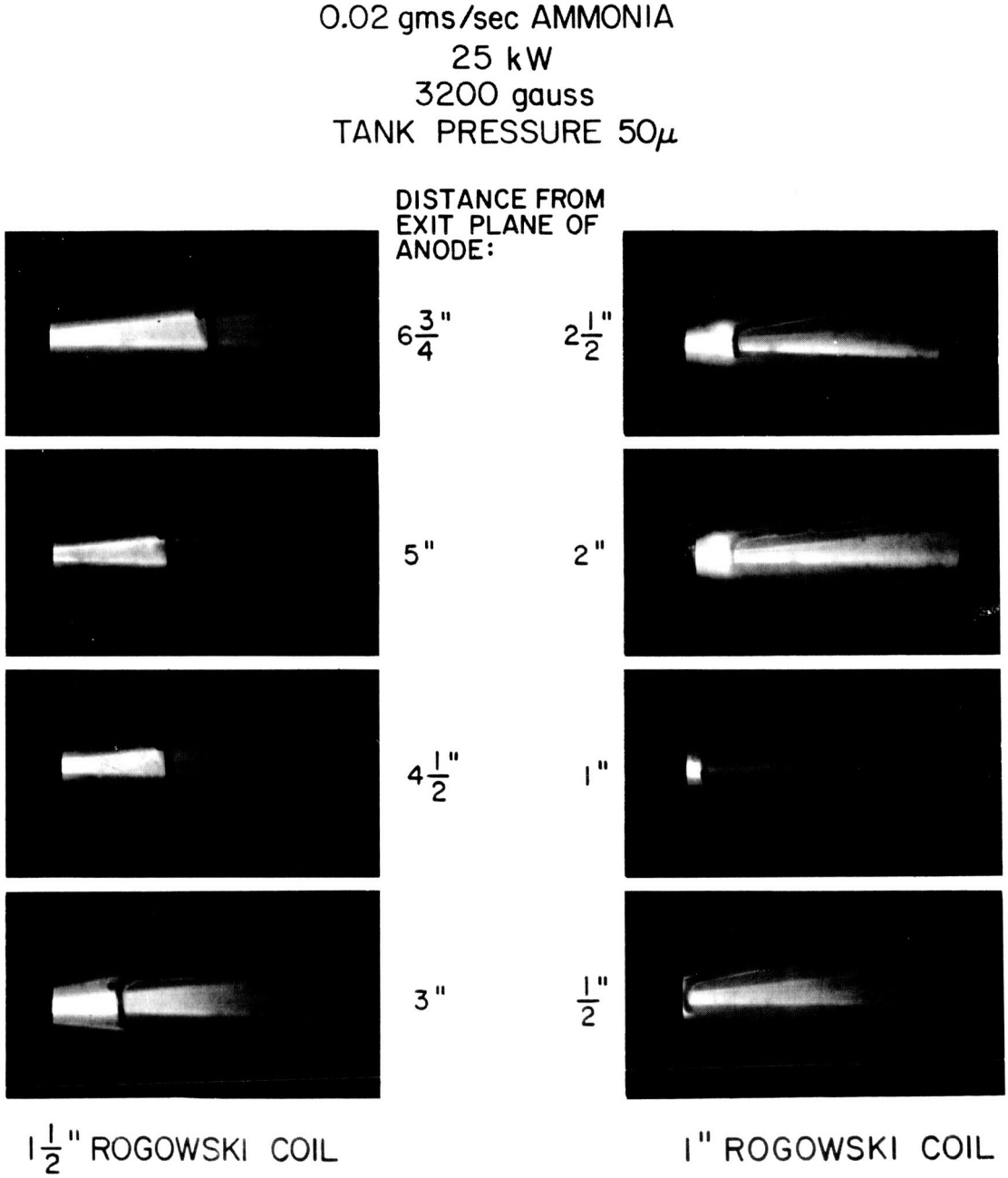

Fig. h Photographs of the 1-1/2" and 1" Rogowski coils in the MAARC exhaust in ammonia.

A5055

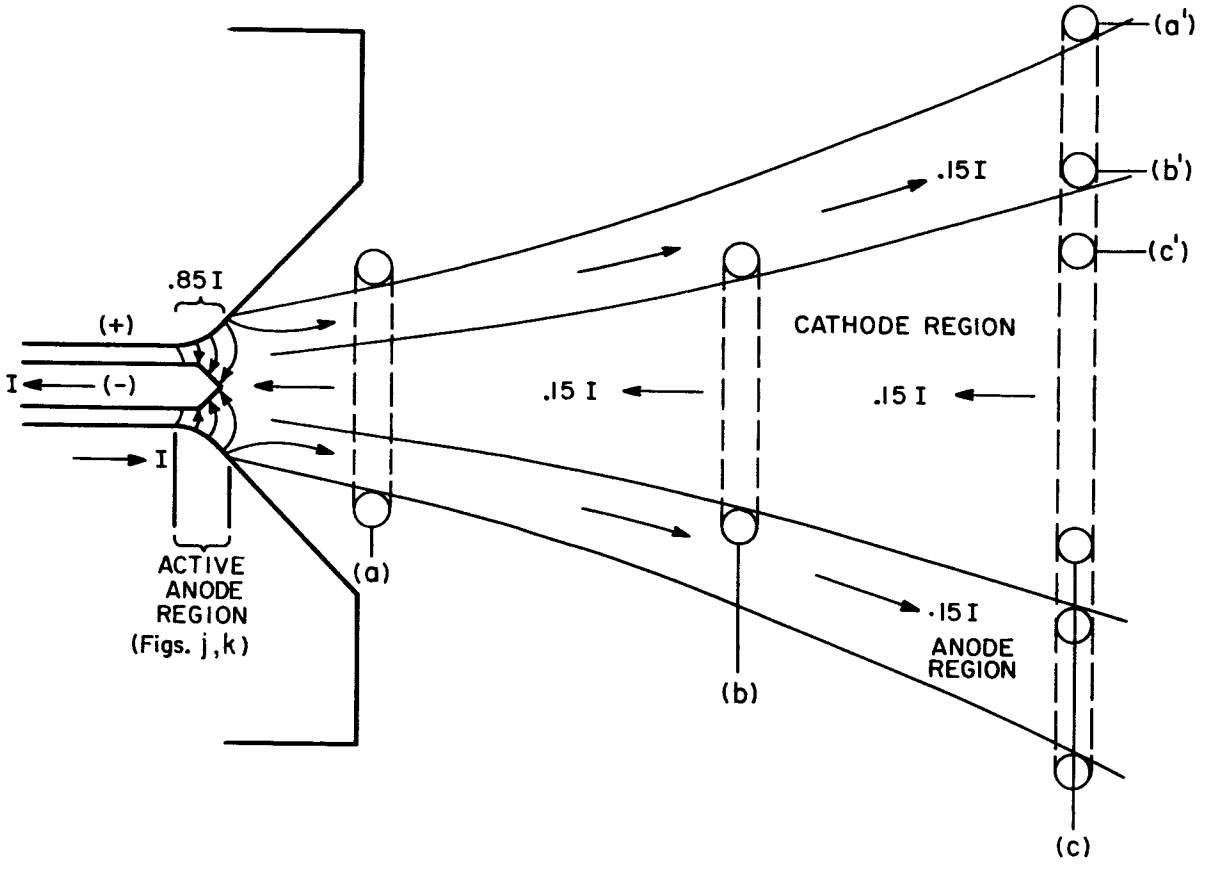

Fig. i Model for the current flow in the MAARC under the operating conditions studied.

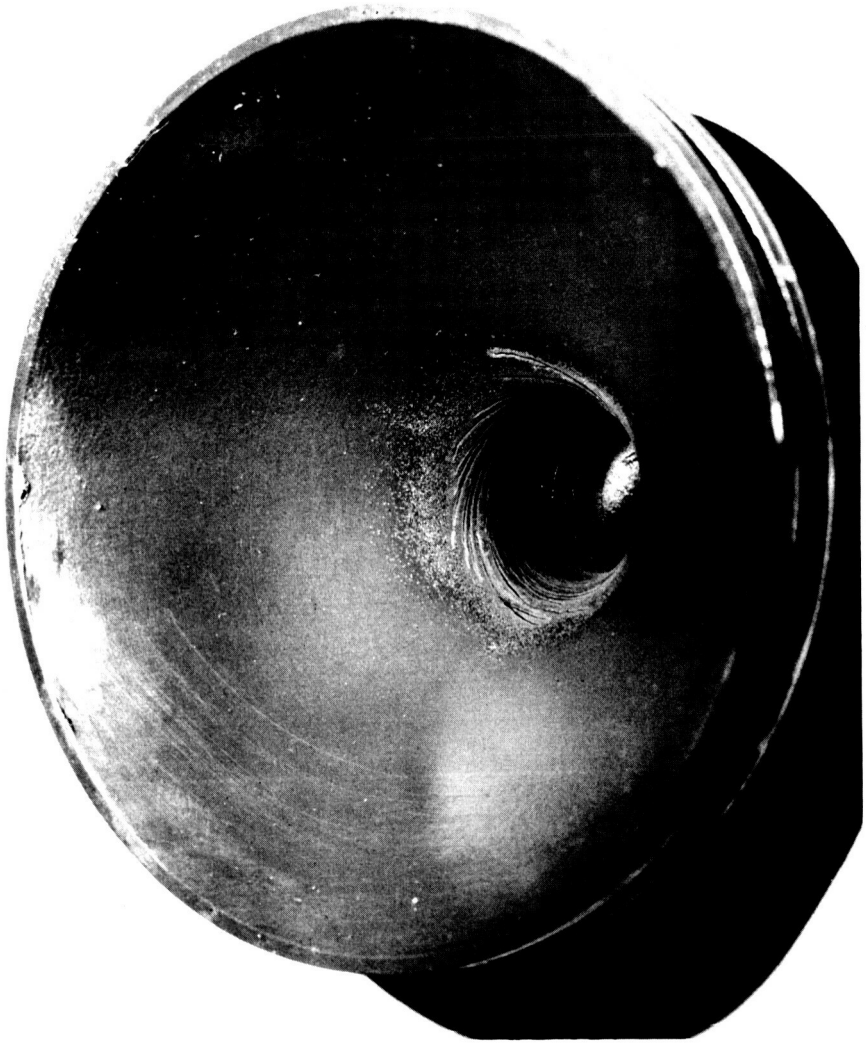

Fig. j Photograph of the MAARC anode showing painted region and electrically active area.

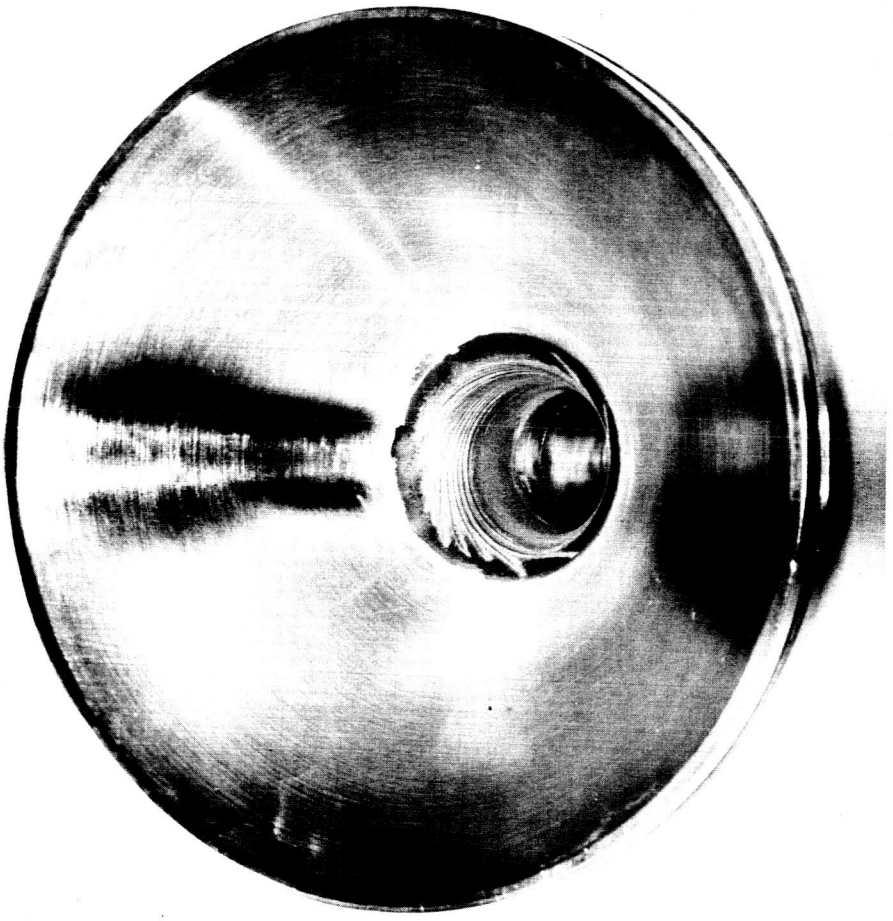

Fig. k Photograph of the MAARC anode which had been painted in a congruent configuration to that shown in Fig. j.